

# Uitnodiging

De promototieplechtigheid vindt plaats op 13 november 2002 in zaal 2 van het gebouw van Bestuur en Beheer op de campus van de Universiteit Twente te Enschede.

Om 14.45 uur zal ik een korte toelichting geven op mijn proefschrift, gevolgd door de verdediging om 15.00 uur.

Aansluitend bent u van harte welkom voor een lopend buffet in bar/discotheek 'Nul74' te Hengelo.

Paranimfen:

Richard Severijns  
Richard.Severijns@brain2.com

en

Hans-Elias de Bree  
06-55343585

ISBN 90-36518288

Distributed thermal micro sensors for fluid flow

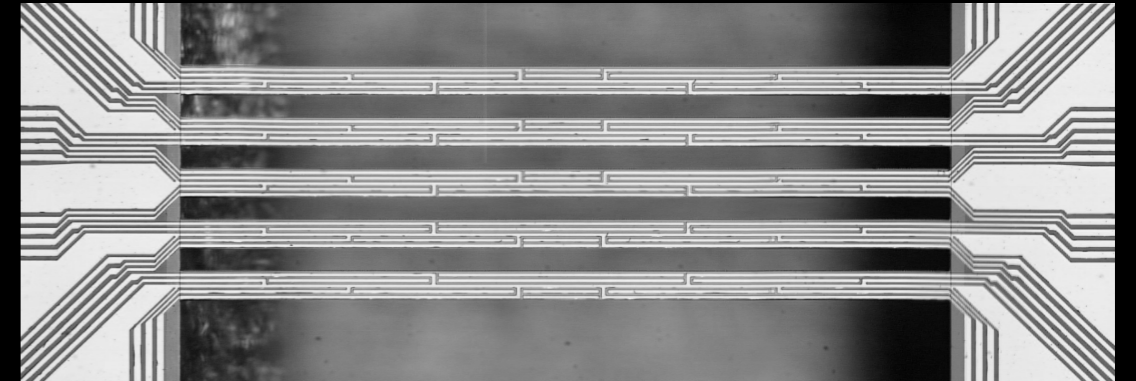


John van Baar

2002



# D-i-s-t-r-i-b-u-t-e-d thermal micro sensors for fluid flow



John van Baar

## STELLINGEN

behorende bij het proefschrift

“Distributed thermal micro sensors for fluid flow”

1. Het wetenschappelijk vormen van een beeld, het modelleren, lijkt meer op boetsen dan op beeldhouwen.
2. Over het algemeen zijn de gratis te verkrijgen open bron-code programma's in het begin duurder in het gebruik dan commerciële producten.
3. Het is een tegenstrijdigheid als een veganist zijn huisdier vlees geeft.
4. Een fietsframe van chitine is sterker dan een van carbon en is natuurlijk biologisch afbreekbaar.
5. In treinen is te verwachten dat jongeren vooruit en bejaarden achteruit reizen, gezien de kijk op het leven en de grotere veiligheid van het achteruit reizen.
6. Onthaasting begint bij het gebruik van het openbaar vervoer en de fiets.
7. Eerder dan hondenbezitters behoren ruiters een spade bij zich te hebben om faecaliën van de openbare weg af te pluggen.
8. Een toegevoegde waarde van meerdere weerstandjes ten opzichte van één is het mogelijk maken van het elimineren van de temperatuurcoëfficiënt van de elektrische weerstanden. *(dit proefschrift)*

John van Baar, 2002

# Distributed thermal micro sensors for fluid flow

John van Baar

The research in this thesis was carried out at the group Transducers Science and Technology of the MESA<sup>+</sup> Research Institute at the University of Twente, Enschede, The Netherlands. This work was supported by the Technology Foundation STW.

De promotiecommissie:

*Voorzitter en secretaris:*

Prof. Dr. C. Hoede	Universiteit Twente
--------------------	---------------------

*Promotoren:*

Prof. Dr. M. Elwenspoek	Universiteit Twente
-------------------------	---------------------

Prof. Dr. P.P.L. Regtien	Universiteit Twente
--------------------------	---------------------

*Leden:*

Prof. Dr. Th.H. van der Meer	Universiteit Twente
------------------------------	---------------------

Prof. Dr. J. Mellema	Universiteit Twente
----------------------	---------------------

Prof. Dr. J.H. Huijsing	Technische Universiteit Delft
-------------------------	-------------------------------

Prof. Dr. M.J. Vellekoop	Vienna University of Technology
--------------------------	---------------------------------

Baar van, John

Distributed thermal micro sensors for fluid flow

Ph.D. thesis, University of Twente, The Netherlands

ISBN 90-36518288

Subject headings: thermal, Pirani, pressure sensor, distributed sensing, fluid parameters, flow, anemometry, micromachined

A digital version of this thesis in pdf-format can be downloaded from the catalogue of the library of the University of Twente or from the URL

<http://utep.e1.utwente.nl/tt/research/finished.htm>

Typesetting: pdfL<sup>A</sup>T<sub>E</sub>X

Printed: Drukkerij Twente Hengelo

On the cover: flow sensor

DISTRIBUTED THERMAL MICRO SENSORS FOR FLUID FLOW

PROEFSCHRIFT

ter verkrijging van  
de graad van doctor aan de Universiteit Twente,  
op gezag van de rector magnificus,  
prof. dr. F.A. van Vught,  
volgens besluit van het College voor Promoties  
in het openbaar te verdedigen  
op woensdag 13 november 2002 te 15.00 uur

door

John Joannes Jacobus van Baar  
geboren op 7 mei 1971  
te Hoorn

Dit proefschrift is goedgekeurd door de promotoren:

Prof. Dr. M. Elwenspoek

Prof. Dr. P. Regtien

*ter nagedachtenis van mijn moeder*





# Contents

<b>1</b>	<b>Introduction</b>	<b>1</b>
1.1	Introduction . . . . .	1
1.2	Arrangements of multiple similar sensor elements . . . . .	2
1.3	The basic sensor element . . . . .	3
1.3.1	The application field of flow sensing . . . . .	3
1.3.2	Ease of fabrication . . . . .	3
1.3.3	Thermal sensors are sensitive to a large number of physical parameters . . . . .	4
1.3.4	Simple interfacing . . . . .	4
1.4	Existing sensor structures based on thermal measurement principles . . . . .	4
1.4.1	Flow velocity and mass flow sensors . . . . .	4
1.4.2	Thermal conductivity sensors . . . . .	5
1.4.3	Thermal pressure sensors . . . . .	5
1.5	Outline of this thesis . . . . .	5
<b>2</b>	<b>Design considerations</b>	<b>7</b>
2.1	Introduction . . . . .	7
2.2	TCR-sensor . . . . .	8
2.3	Short description of the structures . . . . .	11
2.3.1	Thermal conductivity sensor . . . . .	12
2.3.2	Thermal flow sensor and diffusivity sensor . . . . .	12
2.3.3	Pirani pressure sensor . . . . .	14
2.3.4	Kinematic viscosity sensor . . . . .	15
2.4	Fabrication . . . . .	16
2.5	Conclusions . . . . .	18
<b>3</b>	<b>Flow sensors with distributed temperature sensing</b>	<b>19</b>
3.1	Introduction . . . . .	19
3.2	Design . . . . .	21
3.2.1	Flow profile . . . . .	22
3.2.2	Sensor beams . . . . .	23
3.2.3	Heat transport . . . . .	23
3.3	Realization . . . . .	27
3.4	Experiments . . . . .	32
3.4.1	Measurement method . . . . .	32
3.4.2	Beams in micromachined channel . . . . .	33

3.4.3	Probe structure . . . . .	40
3.5	Conclusions . . . . .	40
<b>4</b>	<b>V-grooved Pirani pressure sensor</b>	<b>41</b>
4.1	Introduction . . . . .	41
4.2	Theory . . . . .	43
4.3	Model . . . . .	44
4.3.1	Obtaining an estimate for the thermal line conductance . . . . .	46
4.4	Realization . . . . .	48
4.5	Measurement results . . . . .	49
4.6	Conclusions . . . . .	56
<b>5</b>	<b>Combined -Pirani/bending membrane- pressure sensor</b>	<b>59</b>
5.1	Introduction . . . . .	59
5.2	Operation principle . . . . .	60
5.3	Fabrication process . . . . .	63
5.4	Measurement results . . . . .	65
5.4.1	Single heater/sensor device . . . . .	65
5.4.2	Distributed temperature measurement . . . . .	68
5.4.3	Operation as absolute pressure sensor . . . . .	69
5.5	Conclusions . . . . .	71
<b>6</b>	<b>TCR and kinematic viscosity sensors</b>	<b>73</b>
6.1	Introduction . . . . .	73
6.2	TCR-sensor . . . . .	73
6.2.1	Heater along beam . . . . .	75
6.2.2	Heater at center . . . . .	76
6.2.3	TCR obtained from other distributed sensors . . . . .	76
6.3	Kinematic viscosity sensor . . . . .	77
6.4	Conclusions . . . . .	80
<b>7</b>	<b>Conclusions and outlook</b>	<b>81</b>
7.1	Conclusions . . . . .	81
7.2	Outlook . . . . .	82
	<b>References</b>	<b>85</b>
<b>A</b>	<b>Process scheme</b>	<b>89</b>
A.1	General . . . . .	89
A.2	Masks . . . . .	91
A.3	Connection to the macro world . . . . .	93
A.4	Fabrication . . . . .	93
A.5	Wafer . . . . .	93
A.6	Process outline . . . . .	93

<b>B Theory</b>	<b>109</b>
B.1 Physical domains . . . . .	109
B.1.1 Hydraulical . . . . .	109
B.1.2 Thermal . . . . .	112
B.1.3 Electrical . . . . .	114
B.1.4 Mechanical . . . . .	115
B.2 1D temperature distributions . . . . .	115
B.2.1 Cartesian coordinates . . . . .	116
B.2.2 Polar coordinates . . . . .	118
B.3 2D temperature distributions . . . . .	119
B.4 Pirani sensor and thermal conductivity . . . . .	120
B.4.1 Calculation of the thermal conductivity for a dilute gas . . . . .	120
<b>C Lock-in amplifier and <math>\omega - 3\omega</math>-method</b>	<b>123</b>
C.1 Lock-in amplifier . . . . .	123
C.2 $\omega - 3\omega$ -method . . . . .	123
<b>Summary</b>	<b>127</b>
<b>Samenvatting</b>	<b>129</b>
<b>Dankwoord</b>	<b>131</b>



# Chapter 1

## Introduction

In this thesis thermal sensor-actuator structures are proposed for measuring the parameters pressure  $p$ , dynamic viscosity  $\mu$ , thermal conductivity  $\kappa$ , specific heat  $c$ , density  $\rho$  and the fluid velocity  $v$ . In this chapter examples will be given of the added value of many identical simple elements and the added value of several structures with an optimized geometry for the determination of a parameter. Placing the structures in different environments can fulfill different tasks. A short description of thermal flow sensors, pressure sensors and thermal conductivity sensors will be given.

### 1.1 Introduction

Many examples can be given to illustrate the basic idea that using a large number of simple sensor elements can have an added value, which may far exceed the sum of the individual elements. For example, in the field of flow sensing, the basic sensor element could be a hot wire, which is cooled down by a flow [1]. The temperature of the wire is a measure for the amount of flow, but the direction of the flow cannot be determined. Furthermore, the measurement will depend on other parameters like the temperature of the fluid and the type of the fluid. A second hot wire can be used to perform a bi-directional flow measurement or to compensate for temperature fluctuations of the fluid. Thus, combining the two wires in a single sensor system clearly adds functionality that cannot be obtained by two individual hot wires. Adding more wires will result in even more information. Examples are three-dimensional flow [2] and acoustic [3] sensors. Figure 1.1 shows a photograph of the latter, where three acoustic sensors are placed in orthogonal directions on a single chip.

Another example of a simple element is the photodiode in a CCD camera. A single photodiode can be used for proximity detection or simple distance measurements by using the light intensity variation as a function of the distance between source and detector. To compensate for intensity variations of the source a second diode can be used. With triangulation, a much more accurate distance measurement is possible: the position of the spot of the reflected light beam can be accurately determined by an array of photodiodes. The resolution of such a system increases with the number of diodes in the array. Moreover, such a structure in combination with a scanning mechanism allows for the measurement of more complex properties, such

as profiles, shapes and simple other 3D characteristics of objects. Finally, when arranged in a 2D matrix, the well known CCD camera results, with the capability to determine all kind of 3D geometric and radiometric properties. The success of the CCD camera is mainly due to the fact that technology allows for the construction of many photodiodes, densely packed on a small piece of silicon, containing selection and read-out electronics as well.

The work presented in this thesis focuses on the measurement of fluid and flow parameters, which is a challenging field because of the complexity of flow sensing in general and the large number of physical parameters involved. The ultimate aim of the work is to design a sensor system that can simultaneously sense flow parameters, like pressure and flow velocity, and fluid parameters, like density, viscosity and thermal conductivity.

## 1.2 Arrangements of multiple similar sensor elements

When using arrangements of similar sensor elements, we can distinguish between the following three situations:

- Completely identical sensor elements  
In this case the only difference between the sensor elements is the physical position in the array. The CCD camera discussed above is an example of such an array.
- Slightly different sensor elements in order to realize different sensitivities for measured parameters  
Making slight, but substantial, changes in a sensor's geometry usually results in a change in its sensing properties. This effect can be exploited by combining the output signals from different sensor elements. For example, this technique can be used to compensate for offset, [4], or to extend the operation range of a sensor [5]. Another example is related to the Pirani type pressure sensors, which will be discussed in Chapters 4 and 5. In these sensors, a measure for the absolute pressure is obtained by measuring the thermal conductance of a gas between a heater and heat sink that are located at a very short distance from each other. A problem with these sensors is that the measurement is not only dependent on the pressure, but also on the gas composition. By using two sensors with different spacing between heater and heat sink it is possible to compensate for the gas composition [6].
- Identical sensor elements exposed to different phenomena  
A good example is the hot wire discussed earlier. A combination of two hot wires can perform a variety of sensing tasks, depending on the environment. For example, they can be applied as spirit level sensor [7] by making use of free convection, as accelerometer without proof mass [8], based on the inertia of the mass of the fluid, or with proof mass [9], as a balanced flow sensor [10] and as acoustic sensor [11].

Of course, combinations of these three situations are also possible. Furthermore, the classification into these three situations can be quite ambiguous. A lot depends

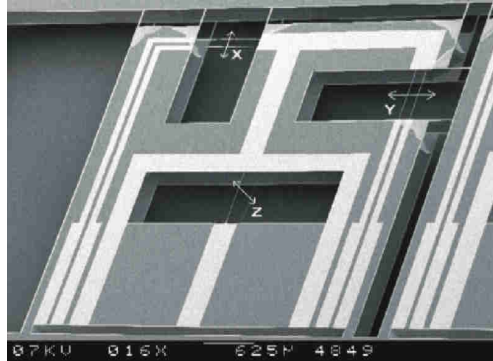


**Figure 1.1:** Photograph of a 3D MicroFlown [3], a 3D acoustic particle velocity sensor that is used in combination with a normal pressure microphone for sound-intensity measurements.

on the definition of a different environment. Even the CCD camera could be classified in the last category because each pixel receives a different portion of the image. All sensors presented in this thesis consist of multiple sensor elements and especially the two techniques of using slightly different elements or exposing the elements to different environments will be used.

## 1.3 The basic sensor element

For the work described in this thesis we have chosen to use simple resistors as the basic sensor element. There are several reasons for this choice, as will be explained below.

### 1.3.1 The application field of flow sensing

Micro flow sensors described so far are either based on thermal principles or on the measurement of pressure distributions and shear stress. The majority of the designs are based on a thermal principle. These sensors add some heat locally to the streaming fluid and measure the resulting temperature distribution close to and far away from the heater, and/or the heat loss of the heater [12]. A simple resistor provides an easy way to generate heat, namely by dissipating electrical power. The amount of heat generated can be monitored accurately by measuring the electrical current and voltage. Furthermore, resistors are generally temperature dependent, so that they can be used as temperature sensor.

### 1.3.2 Ease of fabrication

The resistors used in this thesis were made by sputtering a thin film of platinum on a silicon nitride support layer. A thin chromium adhesion layer was used. The resulting Temperature Coefficient of Resistance (TCR) was rather low and may drift in time, but on the other hand the fabrication process is extremely simple. Compensation of drift is possible by using a TCR sensor as proposed in chapter 6. As an

alternative for using the simple platinum resistors one could think of thermocouples or thermistors. Thermocouples have the important advantage that they measure a temperature difference instead of absolute temperature. As a result they do not suffer from offset problems. Thermistors have a temperature dependent resistance. In fact, the word thermistor is a contraction of the words thermal resistor. Thermistors are usually made from ceramic semiconductors and have either large positive TCR (PTC devices) or large negative TCR (NTC devices). However, the large TCR is usually obtained at the expense of a large nonlinearity.

### **1.3.3 Thermal sensors are sensitive to a large number of physical parameters**

An important advantage of using thermal sensing techniques is that they are also sensitive to a large number of fluid parameters. Usually this is regarded as a disadvantage, but for the work presented in this thesis we need sensor elements that are sensitive to more than one parameter. Measurement techniques based on mechanical deformations due to pressure differences or shear stress are much less sensitive to fluid parameters.

### **1.3.4 Simple interfacing**

Another advantage of using simple resistive elements is the low complexity of the required interface electronics. In principle one only needs to apply a current and measure the resulting voltage drop across the resistor. In contrast, measuring for example small capacitance changes requires much more complex electronic circuitry, see e.g. [12].

## **1.4 Existing sensor structures based on thermal measurement principles**

A large number of thermal sensors can be found in literature. For the work presented in this thesis the sensor structures designed for sensing flow velocity, mass flow, thermal conductivity and pressure are the most relevant. The main characteristics of these sensors are described below, however no attempt is made to present a complete overview.

### **1.4.1 Flow velocity and mass flow sensors**

Many micromachined flow sensor designs can be found in literature. As mentioned above, these sensors add some heat locally to the streaming fluid and measure the resulting temperature distribution close and far away from the heater, and/or the heat loss of the heater. An overview can be found in [12]. The sensors are based on calorimetry or on the boundary layer principle or on a combination [1]. In case of the calorimetric principle the amount of heat is equal to the increase of the heat content of the fluid. Increasing the velocity a part of the fluid will be heated up only in the



thin thermal boundary layer: the boundary layer principle. The first has a linear behavior and the latter shows a square root behavior [13].

Different numbers of wires in a sensor can be found: only one hot wire, which is depending on the change of the fluid temperature and therefore needs an extra temperature sensor in the fluid, two heated wires from which the common and differential signal can be taken, or three wires (usually in sensor-heater-sensor configuration). Even sensors consisting of a much larger number of wires have been reported.

An important advantage of using micromachining techniques over traditional techniques is that it is possible to realize very small hot wires and hot wire-arrays. For example, hot wires with dimensions of 80 by 1 by  $0.5 \mu\text{m}^3$  and a hot wire array have been published by Jiang [14].

### 1.4.2 Thermal conductivity sensors

The thermal conductivity detector (TCD) is an essential part of gas chromatography. It is not as sensitive as solute property detectors such as the flame ionization detector, but it is more simple and robust [15]. TCDs are concentration sensitive devices and ionization detectors are mass sensitive. As the detector size is reduced, the detector volume decreases, but the gas concentration is not greatly affected. Thus TCDs are at large advantage in a miniature system compared to other types of detectors. Miniature TCDs generally involve a thin film of heating element deposited on the floor or suspended in the middle of a micromachined channel etched on a silicon wafer. The former is called a planar and the latter a non-planar miniature TCD. Huang and Bau investigated the forced convection effect on TCDs performances [16].

### 1.4.3 Thermal pressure sensors

Two types of thermal pressure sensors can be found in literature: Pirani sensors and sensors measuring a deflection of a membrane thermally. Both sensors are based on measuring the heat transfer between the heater and the heat sink. In 1906, M. von Pirani found that, in the molecular range, the thermal conductivity of a gas is proportional to the pressure [17]. The advantage of this type of sensors is their wide range and their robustness due to the lack of moving parts. Their range can cover even more than five decades. Several sensor topologies have been used and can be found in the literature. A short overview is given in Chapter 4. Pressure sensors based on thermal measurement of a membrane deflection have been presented recently [18]-[20]. Figure 1.2 illustrates the basic operating principle [20]. The pressure range is now completely defined by the mechanical properties of the membrane. A combined Pirani/bending membrane sensor is presented in chapter 5 [19].

## 1.5 Outline of this thesis

The research that led to this thesis is presented in seven chapters. After the introduction, some general design considerations are discussed in Chapter 2. In this chapter a method will be presented that based on thermal measurement principles in principle allows the measurement of pressure and flow, together with the fluid parameters thermal conductivity, viscosity, specific heat and density. Based on this method a

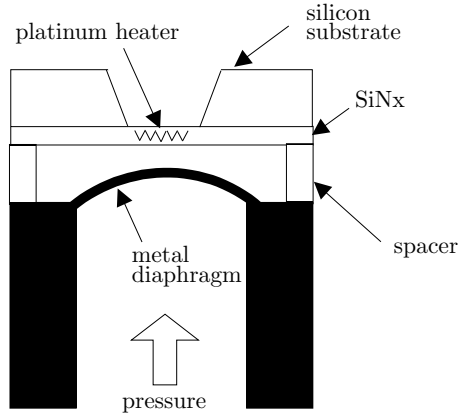


**Figure 1.2:** Pressure sensor with thermal read-out [20]

number of sensor arrangements is designed, each consisting of a number of basic resistive sensor elements. These sensor arrangements are discussed separately in the following chapters.

In chapter 3 flow sensor designs are discussed, which are based on distributed temperature sensing. It is shown that the temperature distribution along a microbridge is dependent on both the magnitude of an applied flow and on the shape of the flow profile (e.g. the parabolic flow profile in a duct).

In chapter 4 a thermal conductivity sensor is presented. Again, a microbridge is used, but now the temperature distribution is made dependent on the thermal conductivity. This is accomplished by placing the microbridge over a V-groove in the substrate, which acts as a heat sink. Although it was not originally designed for this purpose, the same structure can be used as vacuum sensor, because at low pressures the structure operates like a Pirani pressure sensor.

In chapter 5 a combined Pirani/bending membrane pressure sensor is presented. In this case, a membrane is used instead of a microbridge so that a pressure difference causes a deflection of the membrane. This deflection is detected by measuring the change in the temperature distribution over the membrane. At the same time the structure acts as Pirani pressure sensor even at atmospheric pressure levels, because of the narrow gap between the membrane and the silicon substrate beneath it. This allows measurement of the absolute pressure under the membrane.

In chapter 6 two more structures are discussed that have been designed and fabricated, but have not yet been measured. The first structure is a Thermal Coefficient of Resistance (TCR) sensor to detect the TCR of the resistive sensor elements. This sensor is important for auto-calibration purposes. The second structure is sensitive to the kinematic viscosity of a fluid. This structure is an essential part of the measurement scheme developed in chapter 2. The structure is needed to distinguish between specific heat and density.

Finally, in chapter 7 some conclusions are presented.

A number of appendixes is included that contain some theoretical derivations and the process scheme that was used for realization of the designs in the MESA<sup>+</sup> clean room.

# Chapter 2

## Design considerations

In this chapter<sup>1</sup> a framework for the determination of thermal and hydrodynamic parameters is presented. Sensor-actuator structures are proposed that could be used to measure thermal conductivity, flow velocity, heat capacity, kinematic viscosity, thermal diffusivity and pressure. The structures are based on thermal measurements: resistive structures are used for both heating and temperature measurement. A structure for determination of the Temperature Coefficient of Resistance will also be proposed. All structures are designed in such a way that they can be realized in the same fabrication process and therefore they can be easily combined in a single device.

### 2.1 Introduction

As mentioned in chapter 1 electrical resistive elements will be used as basic sensor element for all structures. A resistive element can be used as heater and as sensor simultaneously. Making use of the temperature dependency of the resistivity the temperature can be obtained from the resistance by

$$R = R_0 (1 + \alpha \Delta T) \quad (2.1)$$

with  $\alpha [K^{-1}]$  the temperature coefficient of resistance and  $R_0$  the resistance at  $\Delta T = 0$ . Using an array of such elements makes it possible to measure the temperature distribution.

Thermal techniques can be used to measure various fluid and flow parameters: thermal conductivity [22], flow velocity and diffusivity [23] [24], heat capacity, kinematic viscosity and pressure [25].

In our work the metal heater is positioned on a thin SiN layer. Additional leads were added dividing the heater in several segments enabling measurement of the resistances individually. In this manner the temperature distribution can be measured. This temperature distribution will be influenced by the fluid and flow parameters, like velocity profile and pressure.

In this chapter structures are proposed for measuring the thermal conductivity, the (distribution of) flow velocity, the diffusion coefficient and indirectly the pressure

---

<sup>1</sup>This chapter is based on a paper published in [21].

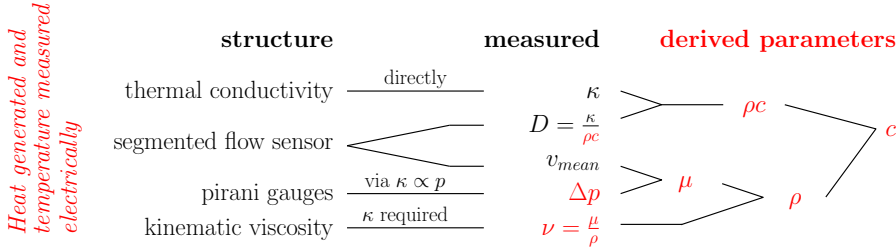


**Figure 2.1:** Overview of the parameters to obtain and how to derive from the measured parameters.

and the kinematic viscosity. From these measured parameters the parameters density, specific heat and the dynamic viscosity can be derived, as indicated in figure 2.1. A more detailed scheme of figure 2.1 can be found in figure 2.2, which will be explained in section 2.3.

The Temperature Coefficient of Resistance drifts in time. Therefore a structure is proposed to measure the TCR.

All structures can be realized in a common fabrication process. Thus, the structures can be easily combined in a single device for simultaneous measurement of several parameters.

## 2.2 TCR-sensor

The bulk value for the Temperature Coefficient of Resistance is  $3.85 \cdot 10^{-3} K^{-1}$ . In MEMS lower values are found of  $2.5 \cdot 10^{-3} K^{-1}$  [26] and even lower. The deviation of thin film material properties from the bulk value can not be explained by the decrease of the effective length of the mean free path of the molecules [27], because the layer is not thin enough: the thickness should be comparable with the magnitude with the mean free path.

Platinum adheres poorly to silicon,  $SiO_2$  and  $Si_xN_y$ . Therefore one needs an adhesion layer. This function is traditionally realized by a thin chromium layer. Platinum and chromium form an intermetallic compound, which has a much lower TCR than platinum. Large temperature variations causes a drift in temperature sensing and poor performance.

Omitting a metal adhesion layer by a ceramic one could solve the problem. A high TCR is found by [28] using an oxidized Si substrate with a  $Si_xN_y$  layer and an  $Al_2O_3$  buffer layer, which has a TCR value of  $3.7 \cdot 10^{-3} K^{-1}$  after annealing at 1100 °C in air.

Two possibilities to compensate for the drift is having a special structure to autocalibrate the TCR or elimination of the TCR by looking at the change of the temperature distribution are presented in this thesis.

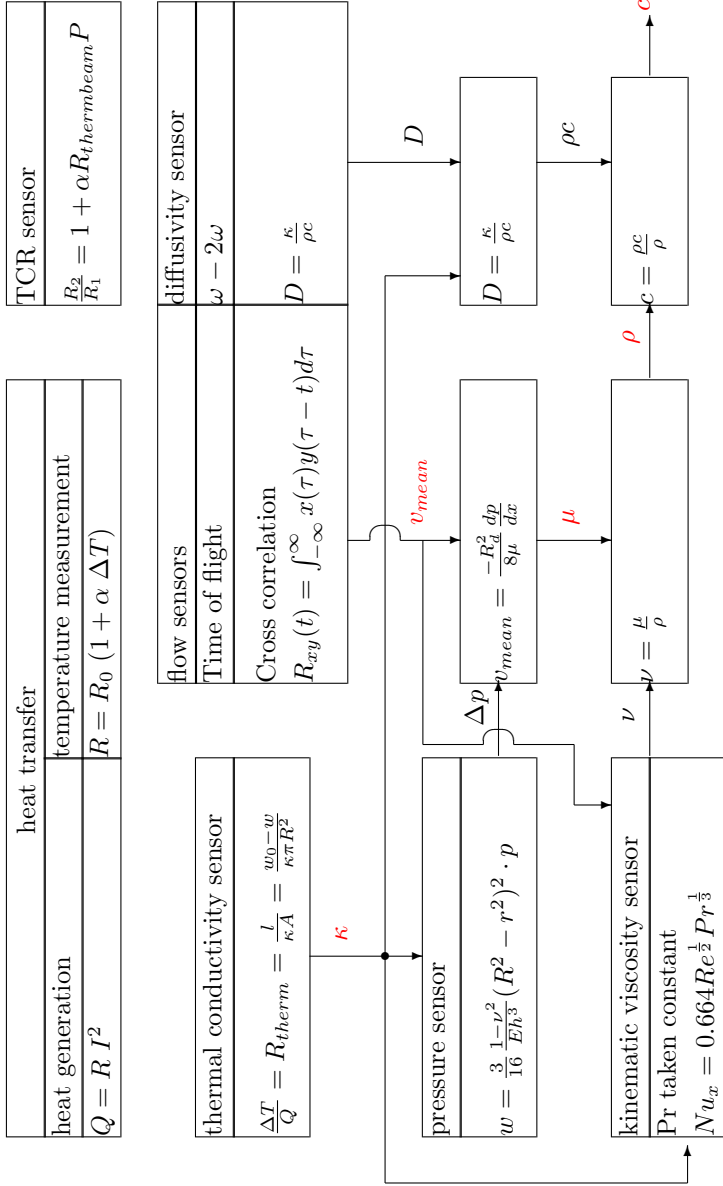
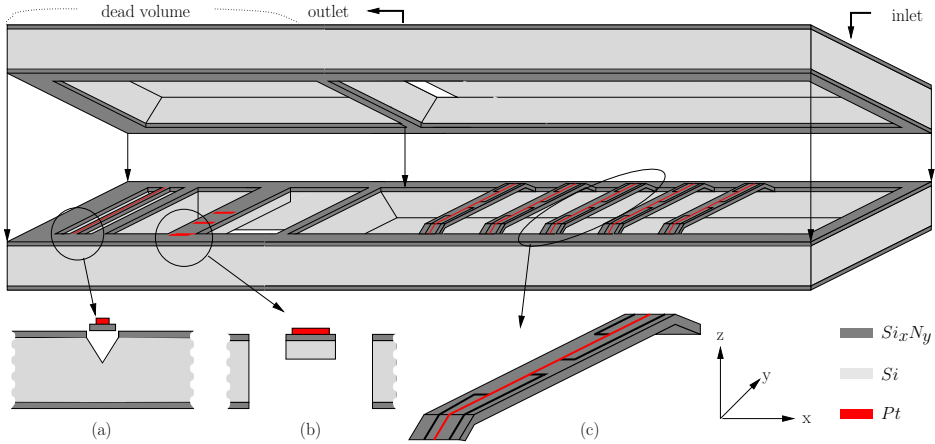


Figure 2.2: Overview of the relations between the parameters

Table 2.1: Overview of the structures and formula

function	structure	formula	parameter
thermal conductivity sensor		$\frac{\Delta T}{Q} = R_{therm} = \frac{l}{\kappa A}$	$\kappa \left[ \frac{W}{(Km)} \right]$
diffusivity or flow sensor		$\Theta(r, t) = \frac{e^{-i\omega t}}{2\pi D} K_0 \left( r \sqrt{\frac{i\omega}{D}} \right)$	$D \left[ \frac{m^2}{s} \right]$
pressure sensor		$R_{xy}(t) = \int_{-\infty}^{\infty} x(\tau)y(\tau-t)d\tau$	$v \left[ \frac{m}{s} \right]$
pressure sensor		$\kappa = \frac{K}{1+p_o/p}$ $w(r) = \frac{3}{16} \frac{1-\nu^2}{Eh^3} (R^2 - r^2)^2 \cdot p$	$p \text{ [Pa]}$
kinematic viscosity sensor		$\frac{P'}{\kappa \Delta T} = Nu_L = 0.664 Re^{\frac{1}{2}} Pr^{\frac{1}{3}}$	$\nu \text{ [Pa s]}$
TCR sensor		$\frac{R_2}{R_1} = 1 + \alpha R_{thermbeam} P$	$\alpha \text{ [K}^{-1}\text{]}$



**Figure 2.3:** Schematic drawing of realized structure (a) thermal conductivity, (b) TCR and (c) segmented flow sensors (not to scale)

A special structure was designed for auto-calibration of the TCR. The TCR-sensor consists of a thick silicon beam with a heater on top of it, see the last structure of table 2.1. The heat transfer through the thick beam to the bulk will be dominant over the heat transfer through the fluid. The temperature distribution will depend only on the applied power and the thermal resistance of the beam. Knowing the change in resistance and the temperature rise the TCR can be calculated, which will be explained in more detail in chapter 6.

## 2.3 Short description of the structures

Figure 2.2 shows a scheme with the proposed sensing principles, the parameters that dominate the output signal of the structures and the parameters that can be derived from these measured parameters. An overview of the proposed structures with formula is given in table 2.1. The functionality of the structures and the relations between them will be discussed below.

Figure 2.3 shows a schematic drawing of the fabricated structures for measuring thermal conductivity, TCR, flow velocity and heat capacity. A channel is formed by etching grooves in two silicon wafers, which are subsequently glued together. The top wafer contains inlet and outlet holes to allow a flow through the right part of the channel, which contains the flow sensor. The TCR and thermal conductivity sensors are placed in a dead volume at the left to reduce the influence of forced convection. The characteristic temperature distributions of the structures, based on their respective geometries and heat transfer properties, are given in figure 2.4. Figure 2.6 shows a schematic drawing of the fabricated pressure sensor and designed kinematic viscosity sensor. The channel can be made in the same way as the first structure.

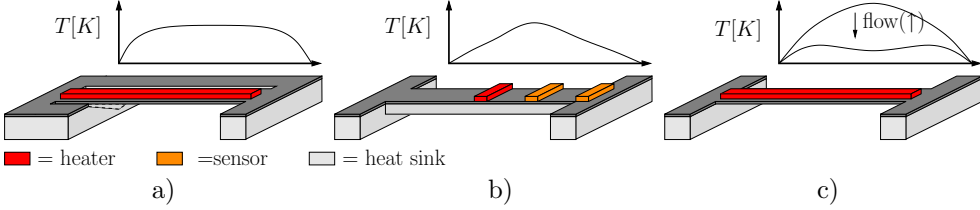


**Figure 2.4:** Characteristic temperature distributions of (a) thermal conductivity, (b) TCR and (c) flow sensors

### 2.3.1 Thermal conductivity sensor

The thermal conductivity sensor is based on the heat transfer from a heater to a heat sink by conduction through a fluid. For a parallel plate approximation the thermal conductivity  $\kappa$  [ $W/(Km)$ ] can be obtained from the applied heating power  $P$  [ $W$ ], the temperature rise of the heated element  $\Delta T$  [ $K$ ] and the geometry using

$$\frac{\Delta T}{P} = R_{therm} = \frac{l}{\kappa A} \quad (2.2)$$

with  $l$  [ $m$ ] the characteristic length between the heater and heat sink and  $A$  [ $m^2$ ] the area of the segments.

Besides the heat transfer to the fluid heat will also be conducted to the support. Therefore the thermal conductivity sensor is a relatively long heater, which is close to a heat sink, but the operating range is still in the viscous region, see table 2.1 for a schematic drawing of the structure.

The following differential equation can be derived for the temperature distribution along the beam [1]:

$$-\frac{1}{R'_b l^2} \frac{\partial^2 T(y_n)}{\partial y_n^2} + G'_f T(y_n) = P' \quad (2.3)$$

where  $y_n$  is the normalized position along the beam,  $G'_f$  is the thermal line conductance of the fluid in [ $W/(Km)$ ],  $R'_b$  is the thermal line resistance of the beam in [ $K/(Wm)$ ] and  $P'$  is the line power in [ $W/m$ ] generated in the heater, see figure 2.5(a).

Using the boundary conditions  $T(y_n = -0.5) = T(y_n = 0.5) = 0$  figure 2.5(b) shows a plot of the solution of equation 2.3 for several values of the shape parameter  $l^2 G'_f R'_b$ , ranging from 0 to 20. The temperature has been normalized to the temperature of the center segment. In the uniform part of the temperature distribution the heat transfer through the fluid to the bottom of the groove is dominant over the heat transfer via the beam to the bulk.

At low pressures the mean free path of the gas molecules becomes larger than the depth of the V-groove. In this range the thermal conductivity depends on the pressure and makes it feasible to use it as a Pirani pressure sensor. A short description is given in section 2.3.3 and is worked out in chapter 4.

### 2.3.2 Thermal flow sensor and diffusivity sensor

We use a structure in which beams cross a channel through its center, see figure 2.3. One of the beams can be heated and the temperature can be measured on all beams.



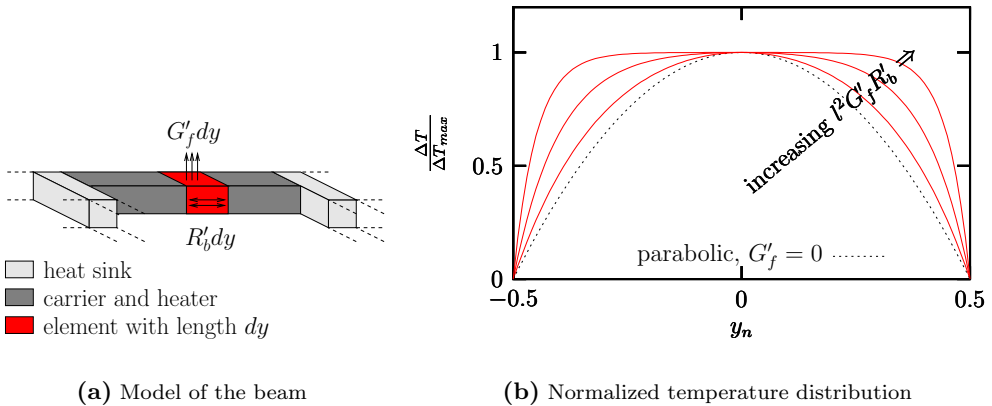


**Figure 2.5:** Model of the beam with line conductance to the fluid  $G'_f$  and the normalized temperature distribution versus the normalized position on the beam as function of the shape parameter  $R'_b G'_f l^2$ .

This yields the temperature distribution along the channel. Additionally, we may measure not only the mean temperature along a beam using one resistor, but also its distribution along the beam using several resistor segments.

Two measurement methods will be explained. The first one gives only the velocity of the streaming fluid, the other one is related to the heat diffusion coefficient. The combination of these types of measurement will yield both, the flow velocity and the heat diffusion coefficient.

The flow velocity  $v$  [m/s] can be obtained in two ways: by time of flight measurement [23] [29], this is measuring the time needed for a heat pulse to travel from one beam to the next, or by an ac measurement [30], where the phase shift of a temperature signal between two sensors is a measure for the flow velocity.

Applying a current with angular frequency  $\omega$  results in a  $2\omega$  component in the power signal. The difference in temperature between the heater and sensor can be measured, which gives the diffusion coefficient  $D$  [m<sup>2</sup>/s]. Under the assumption of a line source and zero velocity the following equation can be used [31]:

$$\Theta(r, t) = \frac{e^{i\omega t}}{2\pi D} K_0 \left( r \sqrt{\frac{i\omega}{D}} \right) \quad (2.4)$$

with  $\omega$  [rad/s] the angular frequency,  $t$  [s] the time and  $r$  [m] the radius. In this equation  $K_0$  is the modified Bessel function of order zero and  $\Theta$  is the complex temperature. Only the real part of this complex temperature is physically relevant.

The diffusion coefficient is defined by:

$$D = \frac{\kappa}{\rho c} \quad (2.5)$$

Combining the thermal conductivity with the diffusion coefficient gives the product of density  $\rho$  [kg/m<sup>3</sup>] and specific heat  $c$  [J/(kgK)].

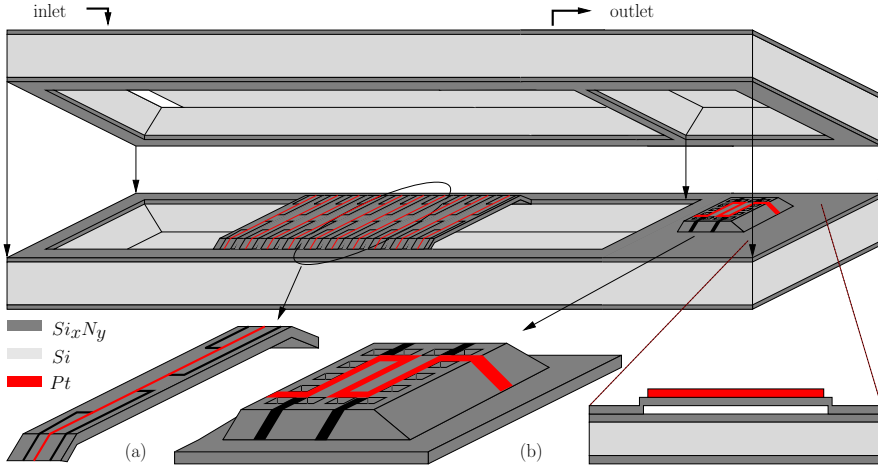


**Figure 2.6:** Kinematic viscosity sensor (a) and pressure sensor (b)

From the mean velocity and the pressure drop  $dp$  [Pa] in the channel, the dynamic viscosity  $\mu$  [Pa s] can be calculated, according to the pressure-drop law of Hagen-Poiseuille for a horizontal circular duct [32]:

$$v_{mean} = \frac{-R^2}{8\mu} \frac{dp}{dx} \quad (2.6)$$

with radius  $R$  [m].

Using several beams makes it possible to measure the change of the temperature distributions downstream by the influences of the precursor heated beams. Decreasing the spacing results in the kinematic viscosity sensor.

### 2.3.3 Pirani pressure sensor

In the molecular range the thermal conductivity of a gas is proportional to the pressure as found by M. von Pirani in 1906 [17]. Absolute pressures can be measured indirectly by measuring the thermal conductivity in the case that the distance between heat source and heat sink is smaller than the free mean path of the gas molecules [25]. For atmospheric pressure this distance should be in the order of 100 nm. The thermal conductivity sensor of section 2.3.1 works in the viscous range at atmospheric pressure: the thermal conductivity does not depend on pressure.

Smoluchowsky [33] has found a relation for the dependence of the thermal conductivity on pressure, which is in simplified form:

$$\kappa \propto \left( \frac{P_t}{1 + P_t/P} \right) \quad (2.7)$$

with the transition pressure  $P_t$  [Pa] depending on the characteristic length of the system, i.e. the distance between heater and heat sink. The transition pressure is proportional to the reciprocal of the characteristic length. Two Pirani sensors in a Wheatstone bridge can be used to obtain the pressure drop in a channel.

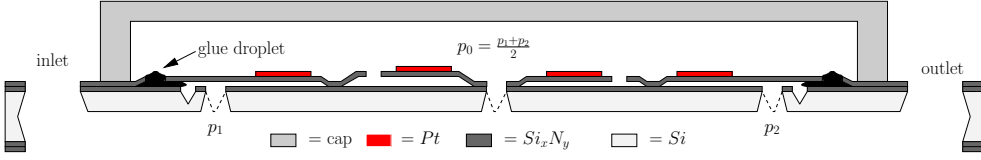


**Figure 2.7:** Cap with integrated absolute (at the center) and differential pressure sensors

The right side of figure 2.6 shows a cross section of the structure, where a thin sacrificial polysilicon layer is etched away between two silicon nitride membranes. To avoid buckling of the top nitride membrane it has to be supported to the substrate at regular distances and to prevent sticking dimples could be added. Thermal guarding can be used to minimize the heat loss to the support.

Another pressure sensor makes use of the bending of the membrane due to the applied pressure difference [18]. This makes use of the changes of the geometry: the distance of the heated membrane to the heat sink changes, which changes the temperature in case of constant heating power.

When a pressure difference  $p_1 - p_2$  [Pa] is applied over a membrane it will bend and the gap distance  $l$  changes. For a circular membrane with radius  $R$  [m] the deflection  $w$  [m] is given by [12]:

$$w(r) = \frac{3}{16} \frac{1 - \nu^2}{Eh^3} (R^2 - r^2)^2 \cdot \Delta p \quad (2.8)$$

with  $\nu$  the Poisson ratio,  $E$  [Pa] the Young's modulus,  $h$  [m] the thickness,  $\Delta p$  [Pa] the pressure drop and  $r$  [m] the radius from the center of the membrane.

Bending membrane and non-bending membrane sensors could be implemented in the cap as indicated in figure 2.7. Also v-groove pressure sensors, with different depths of the v-groove can be integrated. The pressure sensors need openings at the top side of the wafer for KOH etching. Later on this could be closed using a small droplet of glue.

### 2.3.4 Kinematic viscosity sensor

The kinematic viscosity sensor is a plate that is kept at constant temperature in a flow. The kinematic viscosity  $\nu$  [Pa s] can be obtained from the applied line power [W/m] and the thermal conductivity using a local Nusselt number for a plate at constant temperature difference  $\Delta T$  [K] to the ambient [34]:

$$Nu_x = \frac{P'}{\kappa \Delta T} = 0.664 Re_x^{\frac{1}{2}} Pr^{\frac{1}{3}} \quad (2.9)$$

where the local Reynolds number  $Re_x$  is given by  $Re_x = \frac{vx}{\nu}$  with  $x$  [m] the characteristic length. The Prandtl number for the gases of interest ( $H_2, O_2, He, N_2, Ar$ ) at room temperature deviates within five percent from 0.7 and therefore can be assumed constant. The plate is divided in several beams. The heat transfer from each beam can be measured.

Thus, for a known flow velocity and thermal conductivity of the fluid the kinematic viscosity  $\nu$  can be obtained. Combining the dynamic viscosity  $\mu$  and the kinematic

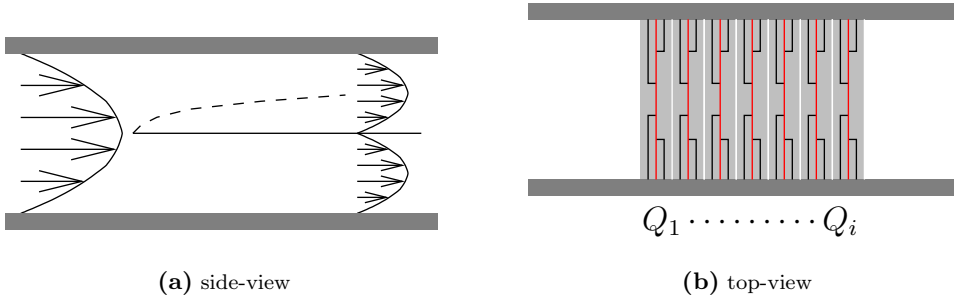


**Figure 2.8:** Velocity profile in a channel with sensors on a plate, which divides the channel in two parts.

viscosity  $\nu = \frac{\mu}{\rho}$  gives the density  $\rho$ . From the product of density and specific heat,  $\rho c$ , an estimate for the specific heat  $c$  can be derived.

Most of the fluid parameters are temperature dependent. To prevent the change of the fluid properties the applied temperature rise due to heating needed for the measurement has to be as small as possible. On the other hand, the signals have to be large enough to be able to gain a good signal to noise ratio.

The basic structure of a kinematic viscosity sensor is shown on the left side of figure 2.6. A silicon nitride plate is placed in the middle of the channel, thus splitting it into two parts. A hydrodynamic boundary layer will be formed as indicated in figure 2.8(a). Several heater-sensor structures - similar to the flow sensor beams discussed before - are placed on top of the plate, as shown in figure 2.8(b). The heat transfer to the fluid will be dependent on the position on the plates and on the kinematic viscosity of the fluid. After a certain distance from the left edge of the plate, the velocity profile is again developed and the heat transfer will become constant.

For fully developed hydrodynamical and thermal boundary layers, the structure can be used as a thermal conductivity sensor.

## 2.4 Fabrication

In figure 2.9 cross sections of all structures are plotted next to each other. The technology for all structures is very similar and they can be realized in a single fabrication process.

The first step of the process is the deposition of a  $1 \mu\text{m}$   $\text{Si}_x\text{N}_y$  layer on a silicon (100) wafer, with a thickness of approximately  $380 \mu\text{m}$ .

For a good alignment a special mask structure, in combination with KOH-etching, is used for precisely finding the crystallographic orientation [35].

This step is necessary because of the large aspect ratio of the channel length to the width. Misalignment results in a large underetch, which widens the flow channel and the v-groove.

The next steps are selectively stripping of the  $\text{Si}_x\text{N}_y$  and the deposition of the 100 nm sacrificial polysilicon layer. The polysilicon layer has two purposes: it defines

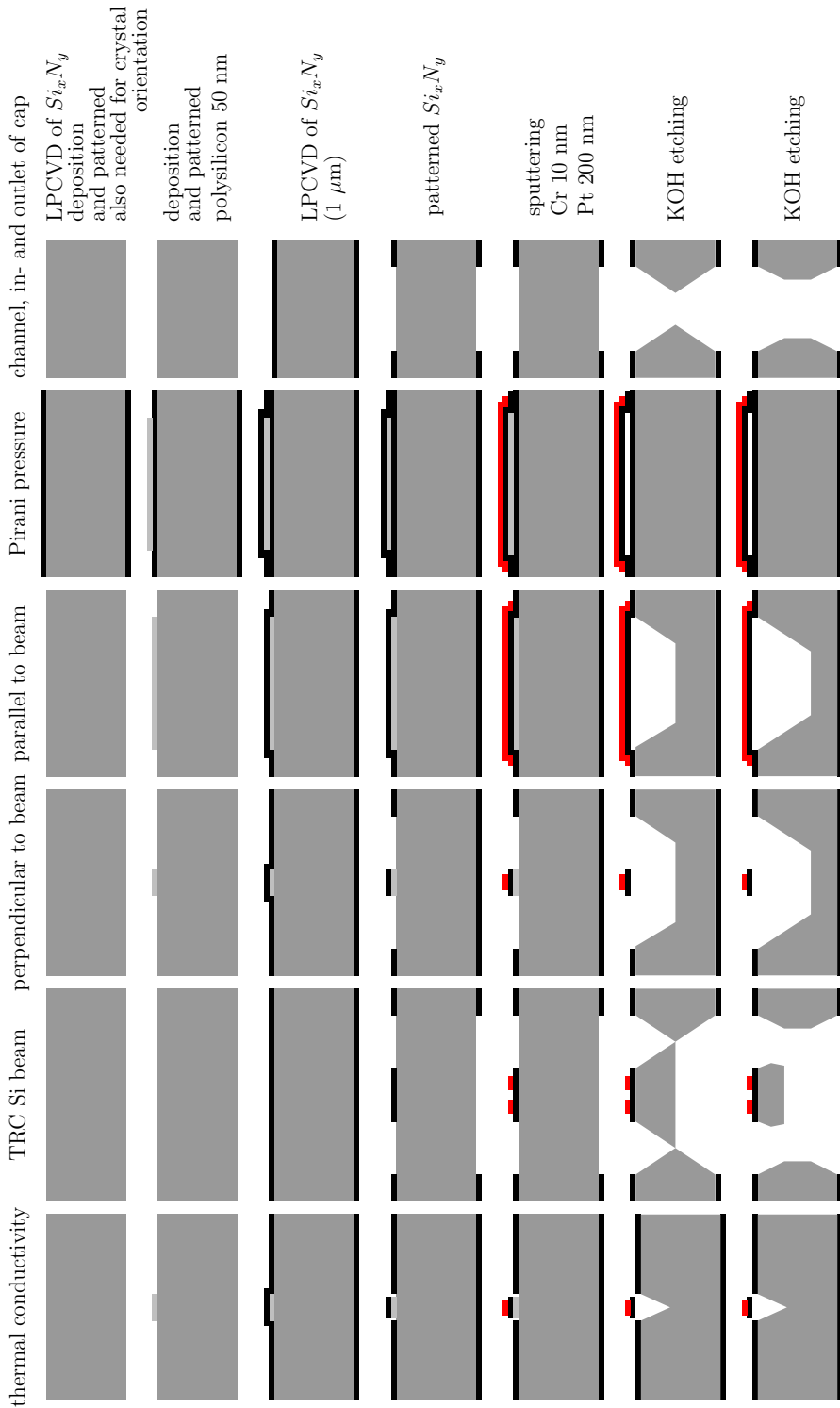
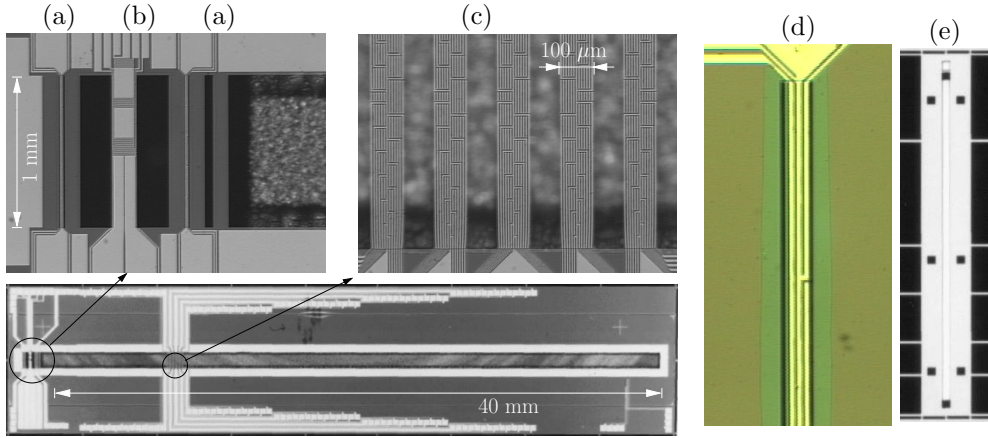


Figure 2.9: Overview process steps of top and bottom wafers



**Figure 2.10:** Photograph of device with magnification of (a) thermal conductivity sensor, (b) TCR sensor (c) segmented flow sensor beams and (d) a close-up of the thermal conductivity sensor. The cap (e) with in- and outlets and six holes for glue. The length of the hexagonal duct is 40 mm, the width is 1 mm and the height is 0.5 mm.

the gap distance in the pressure sensor and it is needed for underetching the beams and plate crossing the channel. After patterning the poly-Si layer a  $Si_xN_y$  layer is deposited and patterned. The 10 nm chromium primary layer and 200 nm platinum layer are sputtered and after lift-off, KOH etching is used for releasing the beams and forming the channel.

For the thermal conductivity sensor KOH etching stops at a maximum depth of 40 μm in stead of 21 μm due to underetch caused by the long etching time. The channel depth under the flow sensor is about 250 μm. The 100 μm beam of the TCR-sensor is etched from both sides, as indicated in figure 2.9. The thickness of the beam is mostly defined by the backetching. The width of the flow sensor beams with 25 resistor segments is 100 μm. The thermal conductivity sensor contains five resistor segments, which results in a width of 25 μm.

The cap is glued on the bottom wafer and the devices are broken out of the wafers. As mentioned before, a device has been fabricated containing a thermal conductivity sensor, a TCR sensor and a flow sensor, see figure 2.10.

## 2.5 Conclusions

A number of structures have been proposed for measuring various fluid and flow parameters. Each structure is optimized for a particular parameter and some have to make use of parameters gained from another sensor. All structures can be realized in the same fabrication process and, therefore, they can be easily combined in a single device. The advantages of beams or membranes with distributed temperature sensing are the elimination of the TCR and the possibility of taking in account the heat loss to the support.

## Chapter 3

# Flow sensors with distributed temperature sensing

A two dimensional resistor structure in a micro-machined hexagonal channel is presented. It contains five homogeneously individually heated heaters, each having sensors for distributed temperature measurements. Using the influence of the flow profile on the temperature distribution of the beam it is possible to measure the flow velocity independent of the temperature coefficient of resistance (TCR) of the sensors. Moreover, the heat transfer to the support can be taken in account. A lumped element model based on King's law has been fit to the measurements. Applying a constant current to all beams the decrease of the temperature downstream and the change of the temperature distribution have been measured. A probe with only one segmented beam has been realized to enable local measurements.

### 3.1 Introduction

A common method to measure flow velocity is Hot Wire Anemometry [1]. The earliest work on that is done by King [13]. An electrically heated wire cools down by the flow, which takes away heat. The resistive element, the Hot Wire, is used as heater and as sensor simultaneously. Sensing is obtained by the change in electrical resistance of the wire with changing temperature.

Besides the heat transfer to the fluid, there is heat transfer to the support that causes an error. This error can be reduced using large length-to-diameter ratios. Commercially mounted wires have a typical length over thickness ratio of 150. For research work a common diameter of the wires is 2.5 to 5  $\mu\text{m}$  [36].

The concept of thin film anemometers was introduced in 1955. On a carrier with low thermal conductivity, high strength and electrically isolating, the conducting film was deposited on the surface. An advantage is the small thermal mass, which gives a better frequency response.

Thermal flow sensors are based on calorimetry [37] or on the boundary layer principle [4]. Calorimetric flow sensors measure the amount of energy needed to raise the temperature of a certain mass of fluid. The most elementary configuration is the

sensor-heater-sensor configuration: two temperature sensors on both sides of a heater. The first sensor measures the temperature of the incoming fluid and the second sensor measures the outgoing heated flow. The heat content of the entire flow can only be measured correctly if the mass of the fluid passing the second sensor, has a uniform temperature.

Heat flux thermal sensors or boundary layer sensors measure a flow dependent change in heat transfer from a heater element to a fraction of the fluid, rather than the temperature change of a defined and mixed volume element. Calorimetric flow sensors have a linear power-velocity relation and for boundary layer sensor the power is proportional to the square root of the fluid velocity. Because the heating is restricted to the boundary layer of the fluid less power will be needed than for calorimetric measurements.

Different numbers of wires in a sensor can be found: only a single hot wire, which temperature is depending on the change of the fluid temperature and therefore needs an extra temperature sensor in the fluid, two heated wires from which the common and differential signal can be taken, or three wires (sensor-heater-sensor structure) [4].

The temperature sensors can contain thermistors, thermocouples, transistors or hot wire elements [4]. A combination of those is also possible: for example a hot wire with thermo couple sensors.

The wires can be placed on the bulk, on a membrane or on a beam. To reduce the heat loss to the substrate a cavity can be made, creating a membrane or beam. The sensor can be positioned in the center of a channel or at the wall. For the latter it is possible to do measurements through the wall, which is very useful when corroding fluids are used.

The first silicon thermal sensor was presented by van Putten in 1974 [38]. The advantage of hot wires made with micro-machining techniques over traditional techniques is to build very small hot wires and hot wire-arrays. A hot wire with dimensions of 80 by 1 by 0.5  $\mu\text{m}^3$  and a hot wire array have been published by Jiang [14].

Two operation methods are common: constant power and constant temperature. The latter method has the advantage of reducing the influence of the thermal capacitance of the structure [36], which results in a higher bandwidth.

Existing sensors measure the average temperature of the micro beam in stead of the temperature distribution. This temperature distribution along a beam depends on the applied flow profile and the type of gas. Using the temperature distribution the heat transfer to the support can be taken in account, which can be obtained by the temperature gradient at the edges of the beam. Normalizing the temperature distribution to the temperature at the center eliminates the dependency on the temperature coefficient of resistance: only the relative change of the resistance matters.

The micro-machined structure with distributed temperature sensing presented in this thesis consists of a thin silicon nitride beam. A chromium-platinum heater is placed at the center along the beam. This heater is divided into 25 segments by 26 additional leads. Via the leads the voltage drop across each of these segments can be measured individually. The average temperature of each segment is calculated from the change in electrical resistance of the segment. Four point measurements are carried out to eliminate the resistance of the leads. The electrical direct current has been applied in both directions to reduce thermal disturbances. In this way the resulting temperature distribution along the homogeneously heated beam has been



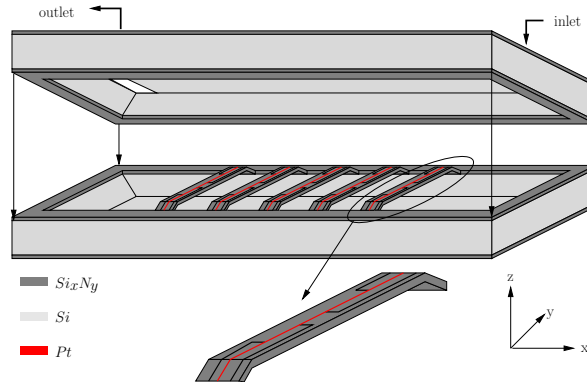


**Figure 3.1:** Segmented beams in channel (not to scale)

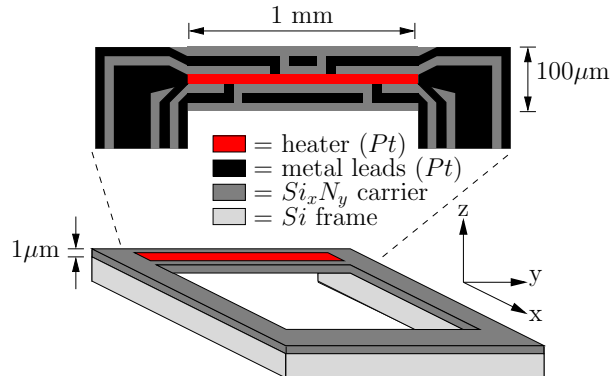


**Figure 3.2:** Probe and top view, drawn with five segments in stead of 25

measured.

The influence of the flow velocity profile on the temperature distribution along a heated segmented micro-machined beam has been studied. Two types of devices have been fabricated: a micromachined probe structure for use in a uniform flow and several beams crossing a micromachined channel with a parabolic flow profile, see figures 3.1 and 3.2. The first can also be used in a sensor-heater-sensor configuration. For simplicity five segments have been drawn in stead of 25. An important application of the flow sensor is the measurement of diffusion coefficient and fluid flow velocity as described in [21]. In combination with other sensors an integrated flow measurement system can be realized that fully characterizes the fluid.

## 3.2 Design

Schematic drawings of the two sensor designs are shown in figures 3.1 and 3.2. The basic element of both sensors is a silicon nitride beam carrying a segmented heater. It has a length of 1 mm, a width of 100  $\mu\text{m}$  and a thickness of 1  $\mu\text{m}$ . In the first

**Table 3.1:** Parameters for several gases

gas	$\rho$ [ $kg/m^3$ ]	$c$ [ $J/(kgK)$ ]	$\mu$ [ $Pa\ s$ ]	$\kappa$ [ $W/(Km)$ ]	Pr
CO2	1.8e+00	8.5e+02	1.5e-05	1.7e-02	7.7e-01
N2	1.1e+00	1.0e+03	1.8e-05	2.6e-02	7.2e-01
He	1.6e-01	5.2e+03	2.0e-05	1.5e-01	6.8e-01

**Table 3.2:** Dimensionless numbers and the mean velocity at equal heating power for several gases

gas	$v_{mean}$ [ $m/s$ ]	$Re_{max-beam}$	$Re_{max-duct}$	$\rho_{N2}c_{N2}/\rho_{gas}c_{gas}$
CO2	2.6e+00	6.1e+01	2.1e+02	7.8e-01
N2	3.3e+00	4.2e+01	1.5e+02	1.0e+00
He	4.6e+00	7.5e+00	2.6e+01	1.4e+00

device five of these beams are placed in a flow channel. The flow channel is formed between two bonded  $< 100$  silicon wafers. The bottom wafer contains the sensor structures. The top wafer contains the channel and inlet and outlet holes. The shape of the channel is pseudo hexagonal due to KOH anisotropic etching used to make the (semi) channels. The channel is 40 mm long, 1 mm wide and 0.5 mm high. The second device has one beam only, which is placed between the arms of a U-shaped support. The arms have a length of 5 mm to reduce the influence of back flow. In this way it is possible to do measurements in free air.

### 3.2.1 Flow profile

In the micromachined channel the flow has to develop from the inlet of the channel to the beams. The entrance length in a circular duct is taken as an approximation. In a circular duct the entrance length from a uniform to a parabolic flow profile can be expressed as [32]:

$$x = D * 0.05 * Re_D \quad \text{for} \quad Re_D < 2300 \quad (3.1)$$

where  $D$  [m] is the hydraulic diameter of the duct and  $x$  [m] the entrance length. The hydraulic diameter is defined as the area of the duct  $A$  [ $m^2$ ] over its circumference or perimeter  $P$  [m]:  $D = 4A/P$ . For the micromachined channel, see figure 3.3 a hydraulic diameter of 0.8 mm is a good approximation. Table 3.1 lists the values of some parameters belonging to the gases that were used for the experiments. The mean flow velocities, the Reynolds number for the duct and the local Reynolds number for the beam are given in table 3.2. For carbon dioxide the entrance length will be eleven times the hydraulic diameter. Because of the fact that the flow is not uniform at the entrance length due to the connection from the top side it may be a bit longer. Therefore, the beams were placed at three quarter of the channel length, 30 mm from the inlet, so that we can safely assume a fully developed parabolic flow profile at the position of the beams.

For the probe structure measurements were performed in a plastic tube with a diameter of 14 mm. In this case the beam dimensions are much smaller than the

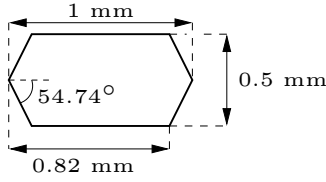


**Figure 3.3:** Cross section of the hexagonal channel with dimensions

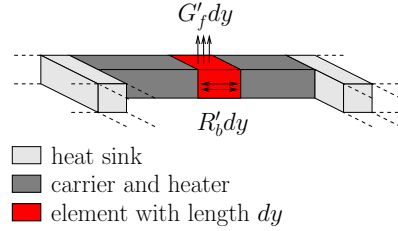


**Figure 3.4:** Model of a heated beam

tube diameter and therefore the flow velocity can be assumed uniform over the entire beam.

### 3.2.2 Sensor beams

Sensor beams with a length of 1 mm and thickness of 1  $\mu\text{m}$  were used. The width of the beams was dependent on the number of segments. The width of the heater and the leads were taken 5  $\mu\text{m}$  and the space between the wires was 2.5  $\mu\text{m}$ . A photograph is shown in figure 3.10(b). For measuring the voltage drop over 25 segments 26 voltage contact points were needed, which results on both sides in thirteen connections due to the symmetry. The width of the beam is the summation of one heater with a spacing on both sides and twelve leads with on one side a spacing:  $5 + 2 \cdot 2.5 + 12 \cdot 5 + 12 \cdot 2.5 = 100 \mu\text{m}$ . The first and last voltage contact leads and the current contact leads are positioned on the bulk, not on the beam. For gaining a uniform thermal resistance dummy strips are applied between the segments on places where no contact leads are deposited and no spacing is required.

To minimize the heat through the beam to the support the ratio of length to the cross sectional area should be as large as possible. On the other hand, measurement of the temperature distribution instead of the average beam temperature allows for compensation of this heat loss. A compromise should be made between the spatial resolution of the temperature distribution and the width of the beam. Using 25 segments results in a sufficiently high spatial temperature resolution. A version with nine segments, resulting in a beam of 40  $\mu\text{m}$  width, has also been realized.

### 3.2.3 Heat transport

The shape of the temperature distribution along the beam is defined by the heat transfer by conduction through the beam and the heat transfer to the fluid, see figure 3.4. The latter is caused by free- and forced convection, radiation and conduction through the fluid.

The stationary temperature distribution along the beam, i.e. in the  $y$ -direction in figures 3.1 and 3.2, can be described with the following one-dimensional differential equation [1]:

$$\frac{1}{R'_b l^2} \frac{\partial^2 T(y_n)}{\partial y_n^2} - G'_f(u) T(y_n) = -P' \quad \text{for} \quad -\frac{1}{2} \leq y_n \leq \frac{1}{2} \quad (3.2)$$

where  $y_n = y/l$  is the normalized position along the beam with position  $y$  [m] and length  $l$  [m],  $G'_f(u)$  is the flow dependent thermal line conductance of the fluid, perpendicular to the beam, in [W/(K m)],  $R'_b$  is the thermal line resistance of the beam in [K/(W m)] and  $P'$  is the line power in [W/m] generated in the beam. The solution for the differential equation for given  $G'_f$  independent of  $y_n$ , with the Dirichlet boundary condition  $\frac{dT}{dy_n}(y_n = 0) = 0$  and the Neumann boundary condition  $T(y_n = \frac{1}{2}) = 0$  for half a beam due to symmetry, is given by

$$\Delta T(y_n) = \frac{P'}{G'_f} \left( 1 - \frac{\cosh\left(y_n \cdot l \sqrt{R'_b G'_f}\right)}{\cosh\left(\frac{1}{2} l \sqrt{R'_b G'_f}\right)} \right) \quad (3.3)$$

where the product  $l \sqrt{R'_b G'_f}$  is a shape factor, with  $l$  [m] the length of the beam. The temperature profile, normalized at  $T(y_n = 0)$ , is shown in figure 3.5(a). The dashed line represents the case that the heat transfer to the fluid is zero. The other curves represent a uniform conductance to the fluid.

The heat from the beam is transferred by the physical processes radiation, free- and forced convection and conduction. The contribution of each term will be approximated and considered whether it is negligible or not with respect to the other terms.

The heat transfer by forced convection can be described by the empirical law [34]

$$Nu_L = C Re_L^m Pr^n \quad (3.4)$$

with  $L$  [m] the characteristic length of the geometry,  $Nu_L$  the Nusselt number averaged over the length  $L$ ,  $Pr$  the Prandtl number and  $C$ ,  $m$  and  $n$  values varying with the nature of the surface and the type of flow. The Prandtl number is defined as  $Pr = \frac{c \mu}{\kappa}$  and the Reynolds number as  $Re = \frac{\rho u L}{\mu}$  with the thermal conductivity  $\kappa$  [W/(K m)], the density  $\rho$  [kg/m<sup>3</sup>], the specific heat  $c$  [J/(kgK)] and the dynamic viscosity  $\mu$  [Pa s]. From theoretical considerations the average Nusselt number for laminar flow has  $C = 0.664$ ,  $m = 1/2$  and  $n = 1/3$ , which results in [34]

$$Nu_L = 0.664 Re_L^{\frac{1}{2}} Pr^{\frac{1}{3}} \quad \text{for } Pr > 0.6 \quad (3.5)$$

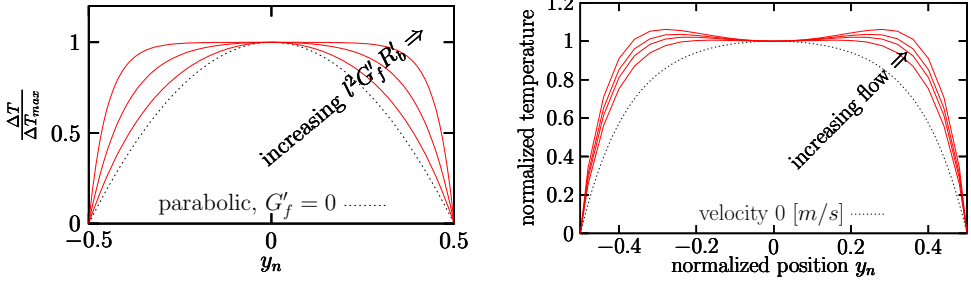
The variation in value between the  $Pr^{1/3}$  for the used gases is only five percent and therefore assumed constant. For the characteristic length the width of the beam has been taken and the applied velocities in table 3.2 to calculate the Reynolds number. For a flat plate the flow is laminar for Reynolds numbers smaller than  $1 \cdot 10^5$ , so in our case the flow is laminar.

The heat transfer for free convection for a long horizontal isothermal cylinder can given by

$$Nu = 0.675 Ra_D^{0.058} \quad \text{for } 10^{-10} < Ra < 10^{-2} \quad (3.6)$$

where the Rayleigh number  $Ra = Gr Pr$  with  $Gr$  the Grashof number. The Grashof number is defined as

$$Gr = \frac{g \beta (T_s - T_\infty) L^3}{\nu^2} \quad (3.7)$$



(a) Analytical model with homogeneous conduction to the fluid

(b) Lumped element model with parabolic flow profile in the x-direction

**Figure 3.5:** Normalized temperature distribution versus the normalized position for a homogeneously heated heater.

with  $g$  [ $m/s^2$ ] the local acceleration due to gravity,  $\beta$  [ $K^{-1}$ ] volumetric expansion coefficient,  $T_s - T_\infty$  the temperature difference between heater and fluid at infinite distance. The Reynolds number provides a measure of the ratio of the inertial to viscous forces acting on a fluid element. The Grashof number indicates the ratio of the buoyancy force to the viscous force acting on the fluid.

Approximating the beam by a cylinder with an effective diameter of  $60 \mu m$  and a maximum temperature rise of  $30 K$  results in  $Gr = 8.2 \cdot 10^{-4}$ . Substituting this into equation 3.6 gives  $Nu = 0.02$

In case that the Grashof number is much smaller than the Reynolds number,  $Gr_L \ll Re_L^2$ , the heat transfer by free convection can be neglected with respect to the forced convection component. For a beam with a width of  $100 \mu m$ , this is the characteristic length, a maximum temperature rise of  $30 K$  and flows larger than  $0.1 m/s$  this assumption is valid. Towards the edges of the beam the flow becomes smaller, but also the conduction through the beam to the support becomes dominant resulting in lower temperature rises. The free convection is assumed negligible. The values of  $Nu$  for the flow can be calculated from equation 3.5 and table 3.2

The heat transfer via conduction through the gas can be approximated by taking a parallel plate approximation for the thermal line conductance in [W/Km]:

$$G' = \frac{\kappa w}{d} = \kappa Nu \quad (3.8)$$

with the width  $w$  [ $m$ ] and  $d$  [ $m$ ] the channel depth. The width of the beam is  $100 \mu m$  and the depth of the channel is  $250 \mu m$ . Equating both sides gives  $Nu=0.8$  The expected Nusselt number will be higher due to parasitic conductances at the edges of the beam. Another approximation is taking a cylinder, see figure 3.6. The method of images is used.

$$G' = \frac{2\pi\kappa}{\ln\left(\frac{2a-r_i}{r_i}\right)} \quad (3.9)$$

with  $2a = 500 \mu m$  and  $r_i = 100 * 1/2\pi = 16 \mu m$  resulting in  $Nu = 1.8$ . The other

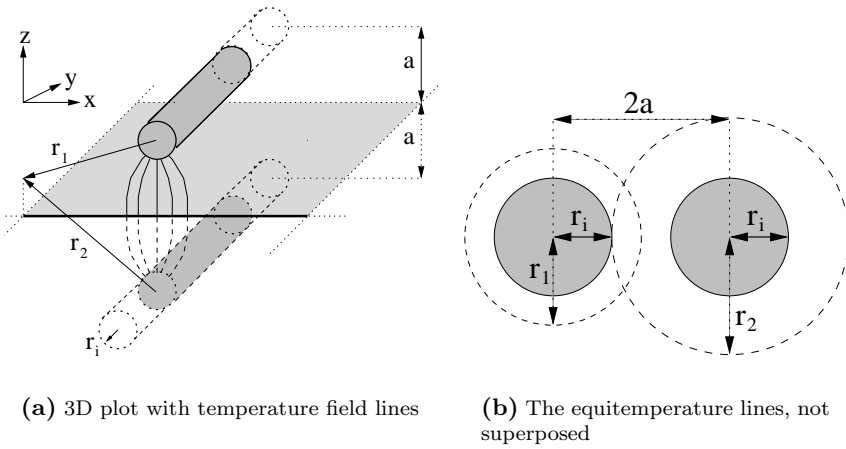


**Figure 3.6:** Method of images for  $\infty$  line source and plane conductor

wall of the channel should also be taken in account by using a grid of positive and negative line sources [Feynman].

Heat transfer via radiation can be approximated using the law of Stefan-Boltzmann

$$P'' = \epsilon \sigma (T^4 - T_0^4) \quad (3.10)$$

with  $\epsilon$  the emissivity of the surface and the Stefan-Boltzmann constant  $\sigma = 56.7 \cdot 10^{-9} [Wm^{-2}K^{-4}]$ . Filling in  $T = 325 K$  and  $T_0 = 295 K$  and taking for a black body  $\epsilon = 1$  results in a power per unit area of  $203 Wm^{-2}$ . The thermal line conductance  $G'_r = P'' * w / (T - T_0)$  becomes  $6.8 \cdot 10^{-4}$ , resulting in  $Nu = 2.6 \cdot 10^{-2}$  for nitrogen.

Radiation can be neglected despite of the fact that the beam is not a black body. Free convection can be omitted because the contributions due to the forced convection or conduction are dominant.

The hydrodynamic boundary layer thickness  $\delta [m]$  can be derived from the continuity, momentum equation and Blasius similarity solution and with  $u/u_\infty = 0.99$  it becomes

$$\delta = \frac{5.0}{\sqrt{u_\infty / (\nu x)}} = \frac{5x}{\sqrt{Re_x}} \quad (3.11)$$

A schematic plot is given in figure 3.7(a) for increasing flow. Using the parameters of table 3.1 and the velocity of table 3.2 the boundary thickness can be calculated. The boundary layer at the center of the beam for highest velocity is about  $80 \mu m$ . As mentioned earlier for low velocities the boundary principle, with its square root behavior, turns into the calorimetric principle, with its linear behavior, see figure 3.7(b).

In the pseudo hexagonal duct we assume an almost parabolic flow profile. The velocity  $u(y_n) [m/s]$  is in the x-direction and depends on the position along the beam, according to

$$u(y_n) = 2 u_{mean} (1 - (y_n/0.5)^2) \quad (3.12)$$

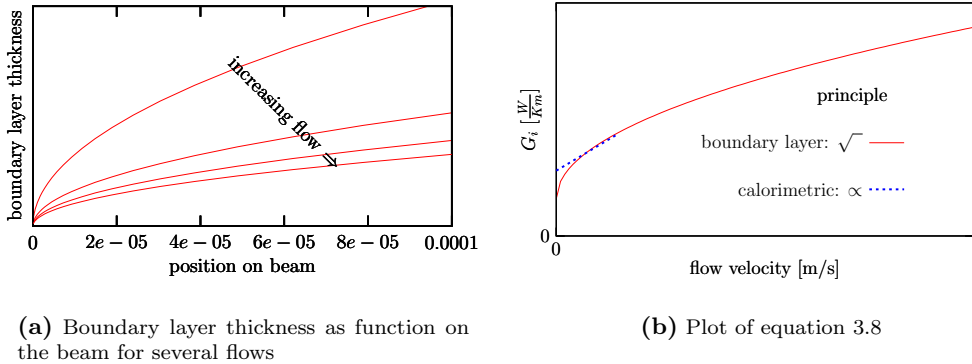


**Figure 3.7:** Boundary and calorimetric principle. The first is proportional to the velocity the second has a square root behavior

with  $u_{mean}$  the mean velocity of  $u$ .

The heat transfer in the x-(and z) direction at position  $y_n$  is modeled according to King's Law

$$G'_f(u(y_n)) = G'_{cond} + G'_{conv}(\sqrt{u(y_n)}) \quad (3.13)$$

with a flow independent thermal line conduction term  $G'_{cond}$  and a forced convection term  $G'_{conv}$ . Both are fluid dependent. Defining  $G'_{cond} = A_{conv} \kappa$  and  $G'_{conv} = B_{conv} \kappa \sqrt{u(y_n)}$  results in two constants, which are independent of  $\kappa$ . Using equation 3.5 and the constant  $C_{0.664}$  then  $B_{conv} = C_{0.664} 0.664 \sqrt{L/\nu} \sqrt[3]{Pr}$  with the kinematic viscosity  $\nu = \mu/\rho$  [ $m^2/s$ ]. For a nonuniform flow profile we take  $G'_f(y_n)$ , depending on the normalized position  $y_n$ . Equation 3.2 transforms into a non-linear differential equation, which is difficult to solve. For this reason we have developed a lumped element model, see figure 3.8. The heat transport through the beam itself is modeled by the conductances marked  $G_b$ . The heat transport through the fluid is due to a combination of conduction and forced convection and is modeled by the conductances  $G_i$ .

In figure 3.5(b) the calculated normalized temperature distribution along the beam for several flows has been plotted, taking  $N_2$ ,  $CO_2$  and  $He$  as model gases. A dip appears in the temperature distribution due to the parabolic velocity profile. In case of zero flow the curve corresponds with one of the solid lines of figure 3.5(a).

### 3.3 Realization

The flow channel is formed between two KOH etched(100) silicon wafers: the bottom wafer containing the sensor-heater structures and the top wafer containing the inlet and outlet holes.

Figure 3.9 shows the process sequence used for fabrication. The first step of the process is the deposition of a 150 nm thin  $Si_xN_y$  layer on a silicon (100) wafer,

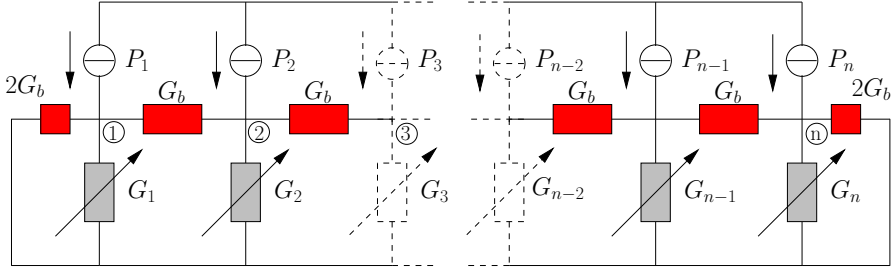


**Figure 3.8:** Lumped thermal model of a beam with  $G_b$  [K/W] the thermal conductance of the beam,  $G_i$  [K/W] the flow-dependent thermal conductance to the fluid and  $P$  the power [W].

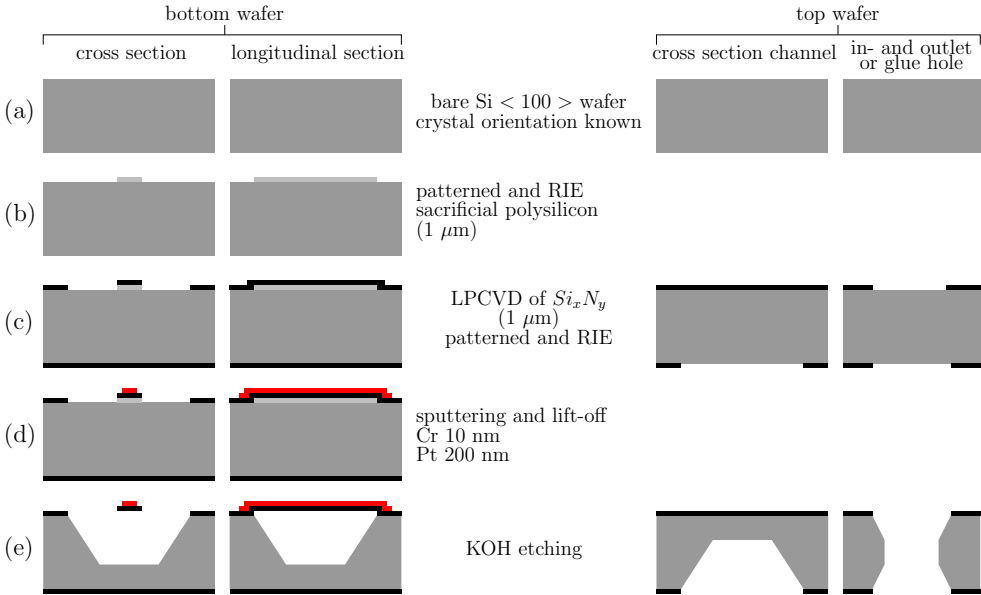
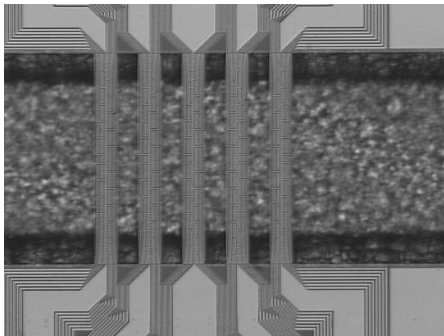
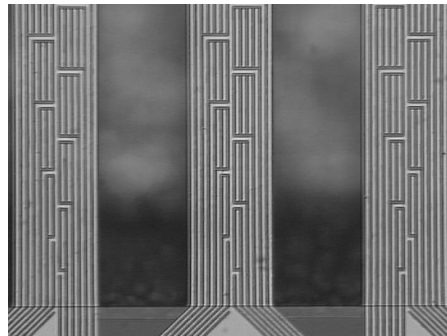


**Figure 3.9:** Sequence of process steps

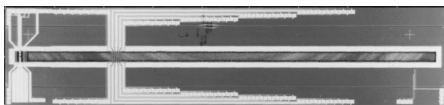




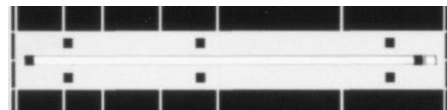
(a) Five beams with distributed temperature sensors



(b) Close-up of part of the beams with resistor segments



(c) Overview of the structure



(d) The cap

**Figure 3.10:** Photograph of the realized flow sensor with segmented beams. On the beams, the central platinum line, is the heater.

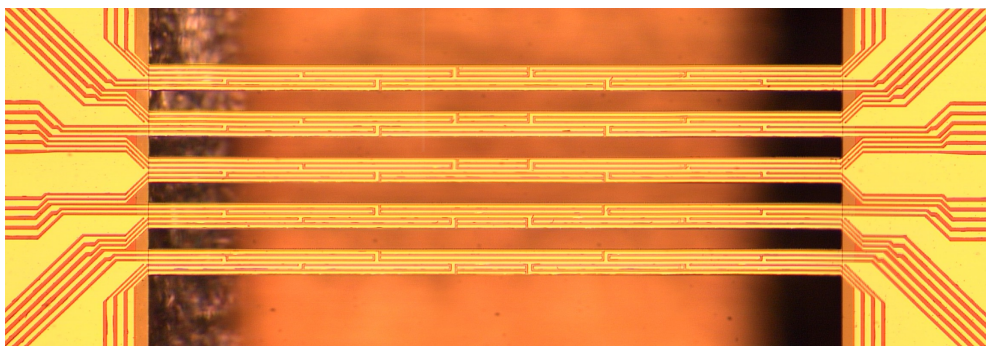


**Figure 3.11:** Photograph of flow sensor array with nine segments per beam

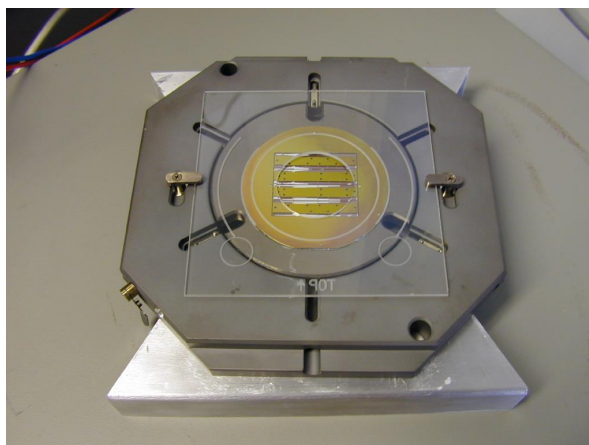


**Figure 3.12:** Pre-bond chuck with quartz mask with wafers clamped in between taken out of the mask aligner. The small holes for glue can be filled.

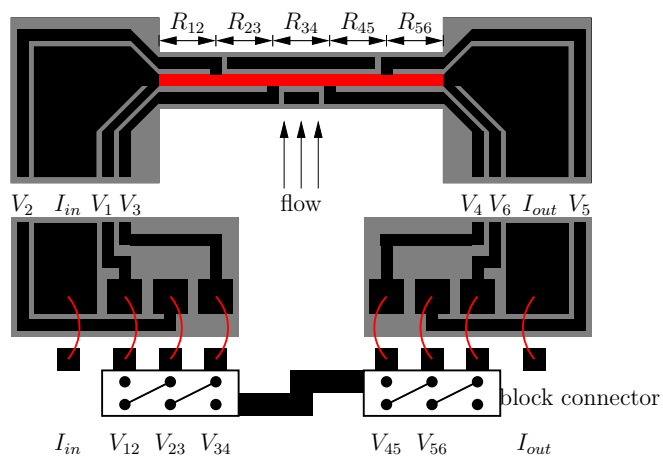
with a thickness of approximately  $380\ \mu\text{m}$ . A special mask structure is used to find the crystallographic orientation precisely [35]. This is necessary because of the large length to width ratio of the channel. A slight misalignment results in a large underetch, which widens the channel.

The next steps are the deposition of a  $100\ \text{nm}$  thin polysilicon sacrificial layer and selective removal by RIE. After the deposition and patterning of a  $1\ \mu\text{m}$   $\text{Si}_x\text{N}_y$  layer, a  $10\ \text{nm}$  chromium layer for adhesion and a  $200\ \text{nm}$  platinum layer are sputtered followed by lift-off. The last step is the KOH etching for releasing the beam and forming a part of the  $250\ \mu\text{m}$  deep channel. For the cap the same sequence is used, except for the polysilicon and metal layers related steps.

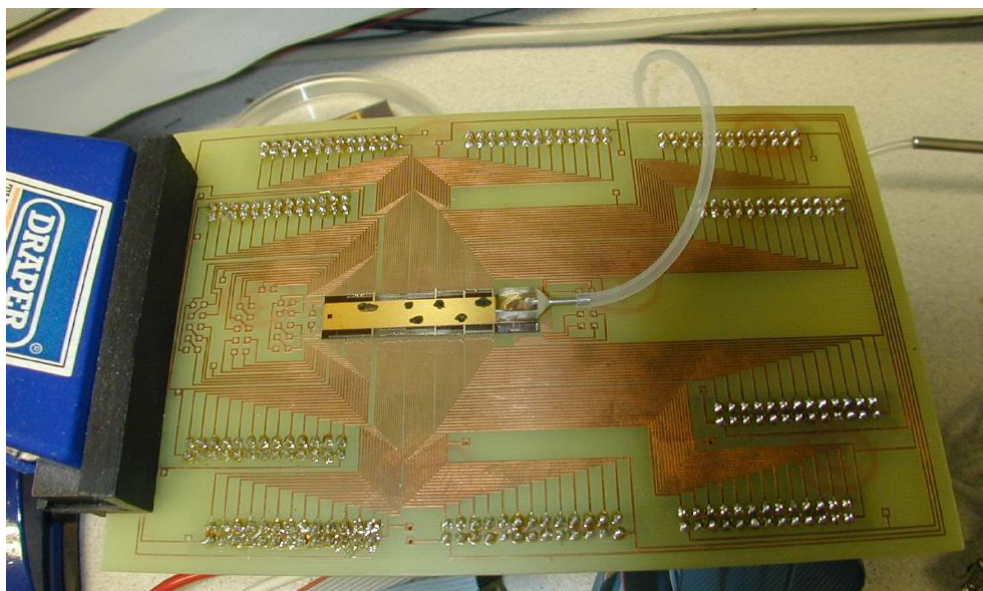
It is possible to etch beams free without using a sacrificial layer by placing beams misaligned to the crystal orientation of the  $\langle 100 \rangle$  silicon wafer. We have chosen for a sacrificial layer because it was needed for other structures on the same chip as well, like the thermal conductivity sensor.

Figure 3.10 shows photographs of a realized device. The leads for the current are made as wide as possible to reduce heating of the substrate. Nine out of 25 segments of each beam can be seen in figure 3.10(b). A version with nine segments per beam is shown in figure 3.11. The heart to heart of the beams is  $70\ \mu\text{m}$ . The top wafer has been mounted onto the bottom wafer by using a mask aligner with a transparent mask, see figure 3.12. The frame and mask with the aligned wafers clamped in between by metal springs can be taken out of the mask aligner. Then the small holes in the cap are filled with glue. The glued devices are broken out of the wafer-pair and mounted on PCB for wire bonding, see figure 3.14. The bond pads of the voltage contact leads of one half of the beam are laid around the current bond pad to have a simple connection to the PCB: on the PCB this should have taken much more room. Via block connectors and flat cable the PCB is connected to instrumentation equipment.

The fabrication process of the probe structure is very similar. A difference is that compensation structures are needed to protect convex corners of the beam suspension. In figure 3.15(a) a top view of the probe with compensation structures is shown.



**Figure 3.13:** Configuration of leads on the chip and PCB



**Figure 3.14:** Chip glued onto the PCB with the block connectors soldered.

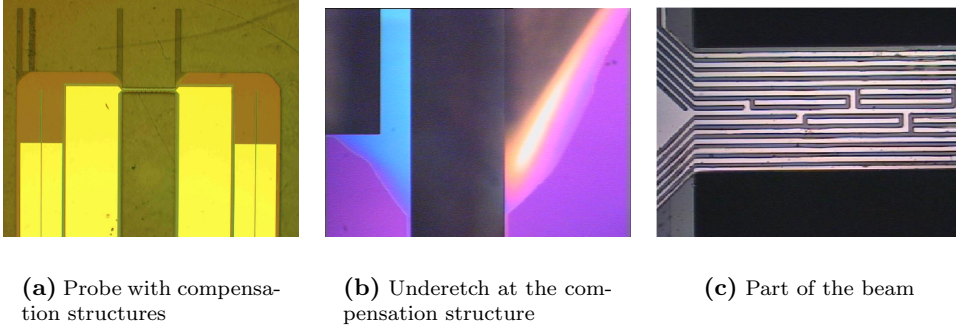


**Figure 3.15:** Photographs of the probe

The compensation structure is to prevent fast etching of the corners, as indicated in figure 3.15(b): the left side, the corner of the probe with compensation structures, shows a small underetch and the right part, a corner on the wafer, which has a large underetch. In figure 3.15(c) a beam similar to the beam of figure 3.10 can be seen.

## 3.4 Experiments

Firstly the measurement method will be discussed, followed by the measurements with the beam in the pseudo hexagonal duct and by the measurements with the probe.

### 3.4.1 Measurement method

A four point measurement method is used for obtaining the electrical resistance of the resistor segments. The spread in resistance values is believed to be primarily due to random variations of the platinum line-width due to the lift-off process, see figure 3.16(a). The first and last segments are larger because of the design. The mean value and the standard deviation of the other segments at 0.25 mA are 7.45 and 0.08  $\Omega$ , respectively.

The temperature rise  $\Delta T$  [K] can be calculated from the measured resistance  $R$  [ $\Omega$ ] and the initial resistance  $R_0$  [ $\Omega$ ] via

$$\Delta T = \frac{R - R_0}{\alpha R_0} \quad (3.14)$$

where  $\alpha$  [ $K^{-1}$ ] is the Temperature Coefficient of Resistance. All resistances have been measured at the currents  $I_{highest}/10$  in steps of  $I_{highest}/10$  up to  $I_{highest}$ . In the measurements of figure 3.16(b) the highest current was 2.5 mA. The dependence on the applied current is due to the resulting change in temperature. The relative change in resistance is a measure for the temperature. We see that this change is largest for the center segment (thirteenth element), which has the highest temperature. The initial resistance  $R_0$  at zero current, this is without self heating, has been obtained by extrapolation of the linear relation between the change in resistance and the applied power. The resistances are normalized to the resistance at highest current. The value

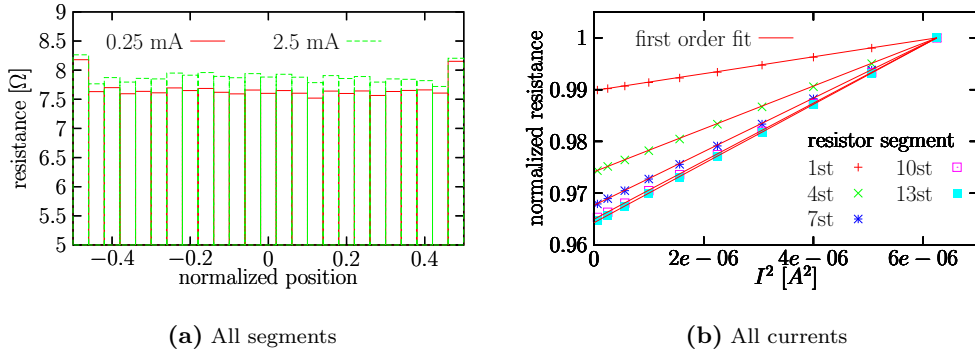


**Figure 3.16:** Resistances of the segments for currents from 0.25 to 2.5 mA. The fit is linear and gives the extrapolated resistance at  $I=0$  A. The temperature rise is proportional to the applied power.

**Table 3.3:** Fit parameters  $A0_{conv}$  for zero flow and  $A_{cond}$  and  $B_{conv}$  for nonzero flow. Temperature per unit line power for several gases.

gas	$A0_{conv}$	$A_{cond}$	$B_{conv}$	$C_{0.664}$
CO2	2.3e+00	1.9e+00	2.3e+00	1.1e+00
N2	2.4e+00	1.8e+00	1.6e+00	1.1e+00
He	1.4e+00	1.4e+00	2.7e-01	5.2e-01

of the extrapolated initial resistance at  $I = 0$  deviates within a factor of  $1 \pm 10^{-5}$  from the value measured at 0.25 mA.

For each measurement a positive and a negative current have been used and the measurements are averaged to reduce thermal disturbances, see figure 3.18 of measurements on another device. Thermo couple voltages arise between two junctions of two metals that have different temperatures.

The temperature coefficient of resistance is determined by measuring the resistances at several temperatures in an oven. The resistance at ambient temperature, the initial resistance, is plotted versus the temperature in figure 3.17(a). For each segment the TCR is calculated, resulting in figure 3.17(b). At the edges of the beam the value decreases. The mean value is  $2.0 \cdot 10^{-3} [K^{-1}]$  and the relative difference between the lowest and highest value is 7%. We don't have an explanation for this yet. For the processing of the data the mean value has been taken for all segments.

### 3.4.2 Beams in micromachined channel

The temperature rise at zero flow is less than 30 K and decreases with increasing flow. The temperature rise is kept small to prevent changes of gas properties with temperature. The maximum change of a gas parameter is about 15%.

The temperature distribution per line power along the beam is measured for several flows for carbon dioxide, nitrogen and helium fluids, see figures 3.19 (a, c and e). To be able to compare the measurements of the different gases, which make use of

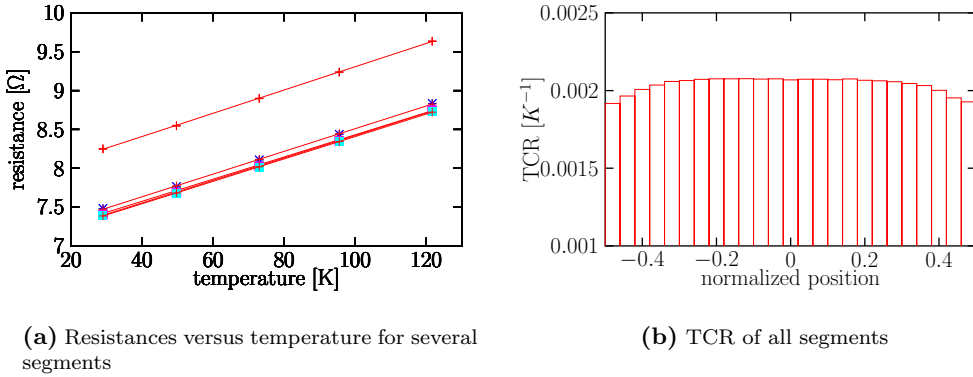


**Figure 3.17:** Extrapolated initial resistances of the segments as function of several oven temperatures to obtain the TCR. Despite the linear behavior the TCR deviates 7% with respect to the center

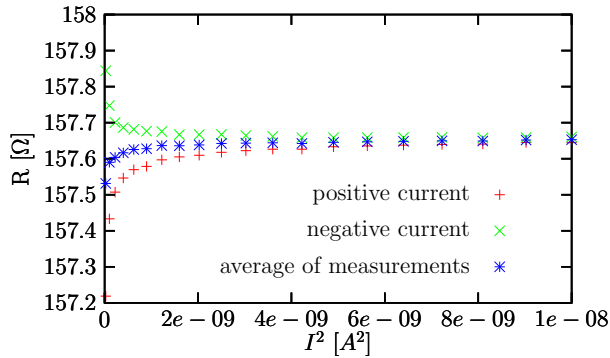
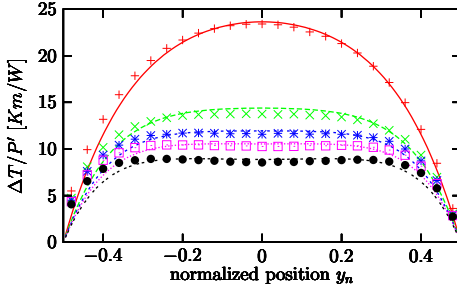


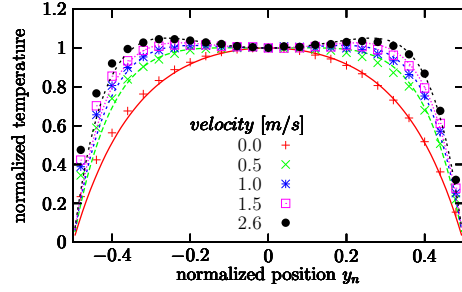
**Figure 3.18:** Average of measurements with positive and negative current for another device

**Table 3.4:** Fit parameters  $A_{0_{conv}}$  for zero flow and  $A_{cond}$  and  $B_{conv}$  for nonzero flow. Temperature normalized to temperature at the center for several gases

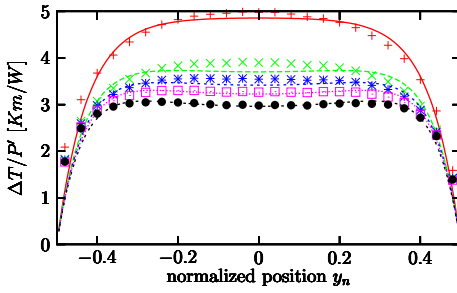
gas	$A_{0_{conv}}$	$A_{cond}$	$B_{conv}$	$C_{0.664}$
CO2	2.8e+00	2.7e+00	3.8e+00	1.8e+00
N2	2.5e+00	2.8e+00	2.3e+00	1.6e+00
He	1.1e+00	6.6e-01	3.2e-01	6.0e-01



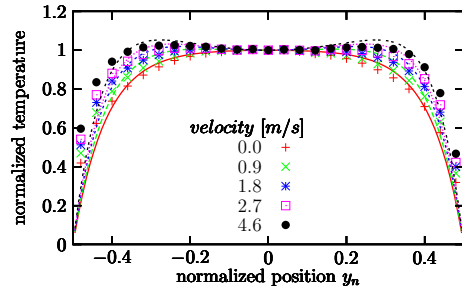
(a) Carbon dioxide



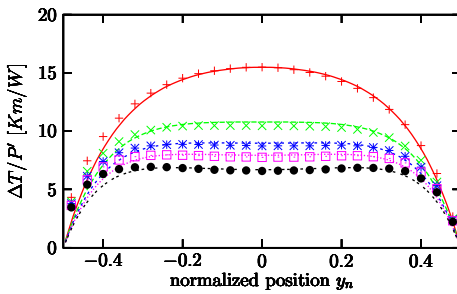
(b) Carbon dioxide



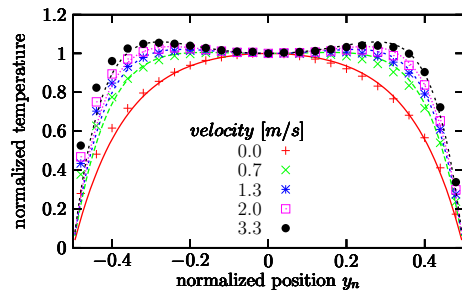
(c) Helium



(d) Helium



(e) Nitrogen



(f) Nitrogen

**Figure 3.19:** Measured temperature distribution per line power versus the normalized position for several gases. The parabolic flow profile in the channel influences the temperature distribution. For the 25 resistor segments are carrying a current of 2.5 mA ( $P' = 1.2 \text{ W/m}$ ) for carbon dioxide and nitrogen and 5 mA ( $P' = 4.9 \text{ W/m}$ ) for helium.

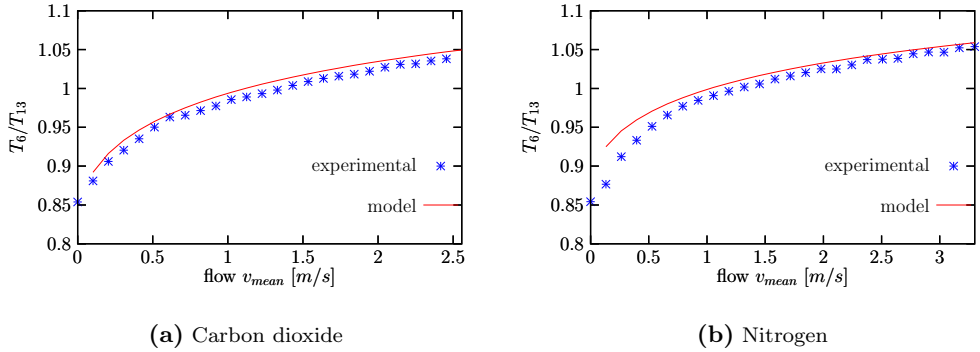


**Figure 3.20:** Ratio of the temperature rise of segment six to the center segment of the beam in the micro-machined channel as function of the flow velocity for nitrogen and carbon dioxide

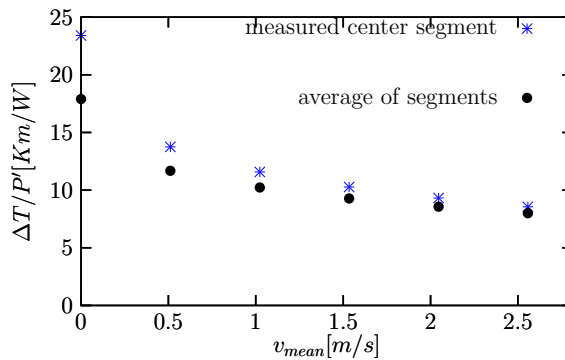


**Figure 3.21:** Measured temperature of the segment in the middle of the beam and the beam mean temperature versus the velocity for carbon dioxide.



different powers, the ratio of the temperature to the power per unit length has been plotted. The volume flow for nitrogen was 0.1 liter/min. For each gas the same heating powers are applied to the channel using a mass flow controller of Bronkhorst High Tech. Using the mass flow controller for another type of gas than the reference gas nitrogen, a conversion factor has to be applied that is defined as

$$factor_{conversion} = \frac{\rho_{N2} c_{N2}}{\rho_{gas} c_{gas}} \quad (3.15)$$

The thermal resistance of the beam has been taken:  $8.5 \cdot 10^8 K/(Wm)$  for all gases. Normalizing the data to the temperature rise of the center segment gives figures 3.19 (b, d and f). For clarity the measurement data are plotted as marks. Strictly speaking the marks should be short horizontal lines, because they represent an average over the length of a segment. The measurement data of the zero flow situation is fitted using the analytical formula 3.3 resulting in a value for the fit parameter  $A0_{cond}$ , see table 3.3. Equation 3.5 can not be used, because there is no boundary layer for no flow, see figure 3.7(b). In the model the temperature has not been averaged over the length of each segment. For the nonzero flows the lumped element model is used, resulting in the parameters  $A_{cond}$  for the conduction part and  $B_{conv}$  for the forced convection part. For the lumped element model 101 nodes have been used. The temperature of each segment is the average of four nodes, except the center segment which contains five nodes.

The differences between the fit parameters of the plots of 3.19 (a, c and e) and (b, d and f), given in the tables 3.3 and 3.4, is due to the cancellation of the  $\frac{1}{G}$  part of equation 3.3 in the case the temperature is normalized to the temperature rise of the center segment: information has been thrown away. An advantage is the independence of the TCR.

The ratio of the temperature rise of the sixth segment to the center segment as function of the flow is given in figure 3.20(a) for carbon dioxide and in figure 3.20(b) for nitrogen. The CO2 data fits better than the nitrogen data: for low velocities the model expects a more uniform temperature profile. Probably this is due to the assumed position independent conduction: the inclined walls will result in an extra cooling at the edges of the beam.

Measuring only the center segment gives a higher sensitivity in comparison with the average of all segments, see figure 3.21.

Measurements on the five beams in the micromachined channel have been carried out for several flows (0, 1.6, 3.3 and 6.7 m/s), see figure 3.22 for the temperature distributions normalized to the temperature rise in the center. All heaters have been heated simultaneously. Some segments are missing, because they could not be read out properly due to failing connections. The first beam downstream has the largest side lobes, because the flow at the center of the channel at the second beam has already been heated up by the first beam. Downstream the temperature distribution becomes more uniform. From the change of the profile going from one beam to the next extra information can be obtained. Based on this we are working on a kinematic viscosity sensor, which is proposed in [21].

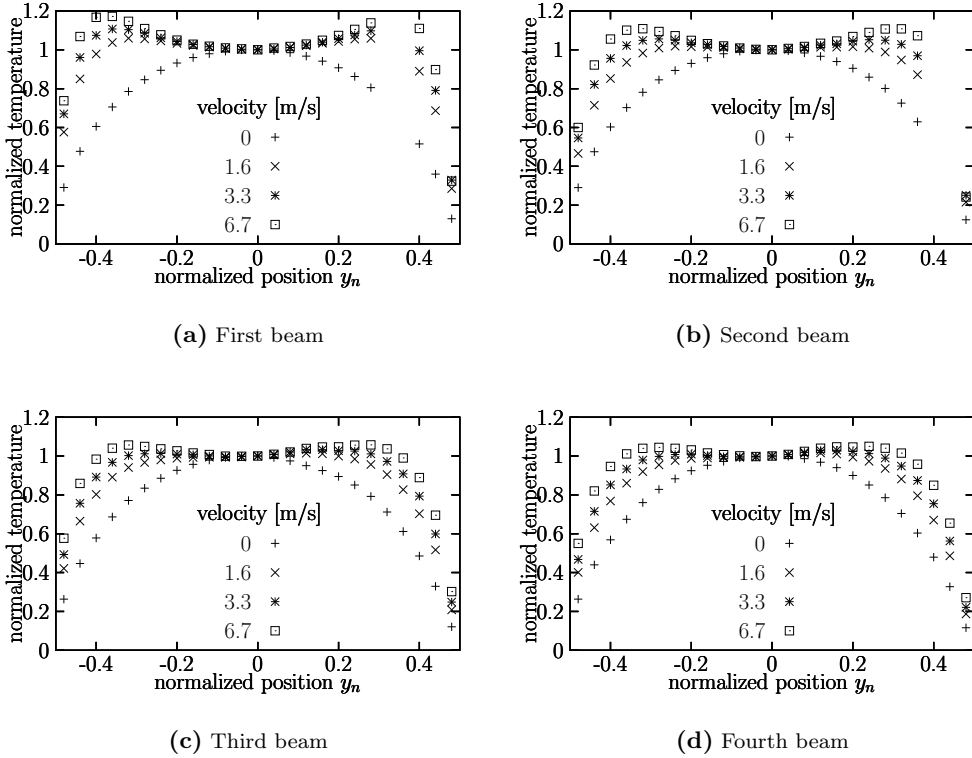


**Figure 3.22:** Normalized measured temperature distribution of a beam on the probe for several uniform flows, carrying 2.5 mA

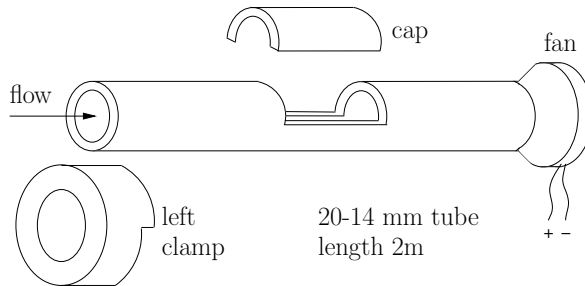


**Figure 3.23:** Schematic overview of the probe in a tube

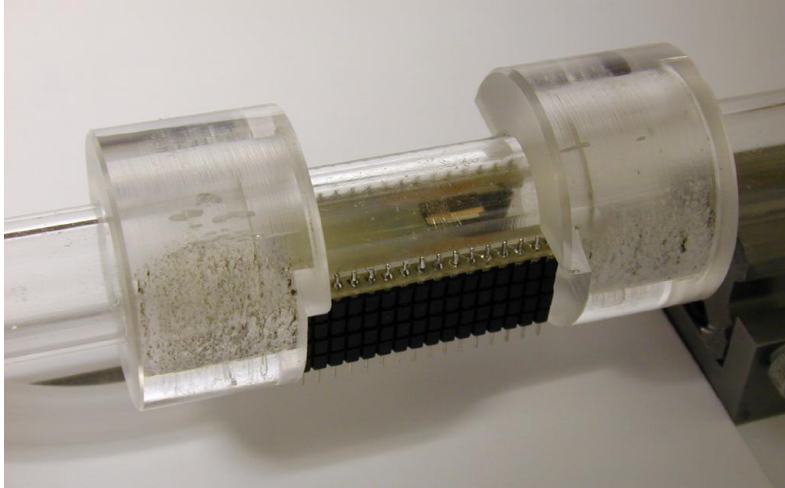
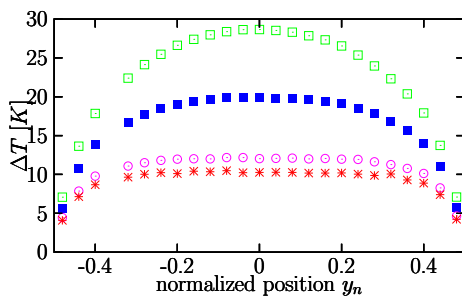
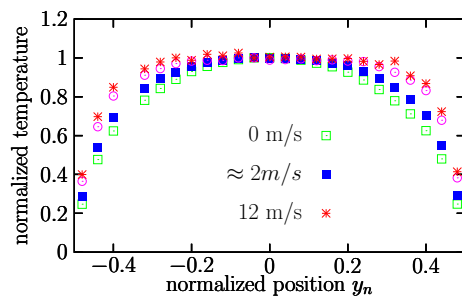


**Figure 3.24:** Photograph of probe in a tube



(a) Temperature distribution



(b) Normalized temperature

**Figure 3.25:** Measured temperature distribution of a beam on the probe for several uniform flows, carrying 2.5 mA

### 3.4.3 Probe structure

Measurements have also been carried out with the probe. The probe has been glued on a PCB and placed in a plastic tube with a fan at the end. The diameter of the tube is 14 mm and compared to the beam of 1 mm the parabolic flow can be assumed uniform along the beam. In figure 3.23 a schematic overview of the flow set-up is given and in figure 3.24 a photograph. The small fan has a maximum debet of 0.9 liter per second. We applied several voltages to the fan, but didn't measure the flow velocity precisely. Neglecting the hydraulic resistance in the tube at highest debet the mean velocity should be 6 m/s, in the center 12 m/s. The temperature distribution for the uniform flows have been shown in figure 3.25(a) and normalized to the center temperature in figure 3.25(b) for several velocities.

## 3.5 Conclusions

A segmented beam with platinum heater and voltage contact leads has been realized in a micro-machined duct. With this structure the temperature distribution along the beam perpendicular to the flow was measured. The flow profile influences the temperature distribution and theoretically the inverse should also be possible. From the temperature distribution the flow velocity is measured independently of the temperature coefficient of resistance (TCR) of the platinum resistors. In practice, it is not necessary to measure the entire temperature distribution, but it would be sufficient to measure the temperature at two positions. A similar beam positioned at the ends of arms has been realized according the same principle.

## Chapter 4

# V-grooved Pirani pressure sensor with distributed temperature sensing

A Pirani pressure sensor is based on the fact that in the molecular range the thermal conductance through a gas is dependent on the pressure. The operation range of Pirani sensors is limited at the low-pressure end by the heat loss through the mechanical structure and at the high-pressure end by the small mean free path of the gas molecules, the latter resulting in a constant thermal conductance. The structure presented in this chapter consists of a heated microbeam, which is placed above a V-groove in the substrate. The temperature distribution along the microbeam is a measure for the thermal conductivity of the surrounding gas. Measuring the temperature distribution instead of the average temperature of the beam has two advantages: the measurement becomes independent of the Temperature Coefficient of Resistance of the temperature sensing resistors and the heat loss to the substrate is implicitly taken in account, which extends the lower pressure range.

### 4.1 Introduction

Pirani absolute-pressure sensors are widely used in vacuum systems [39]-[41]. The operation of these sensors is based on the fact that in the molecular range the thermal conductance through a gas is proportional to the pressure, which was found by M. von Pirani in 1906 [17]. Usually, a Pirani sensor consists of a hot filament, which is suspended at close distance from a heat sink. Like other thermal sensors, two operation modes are commonly used. One is the constant-power mode, in which heating is done at a constant power level and the temperature of the filament becomes a measure for the absolute pressure. The other mode is the constant-temperature mode, in which the power needed to keep the filament at a certain temperature is the pressure-dependent output signal.

In a Pirani pressure sensor the heat conduction from a heat source to a heat sink becomes pressure dependent because the distance between the source and sink is

smaller than the mean free path of the gas molecules. This will be further explained in section 4.2. An important advantage of Pirani sensors is their robustness. They do not contain any moving parts (e.g. a bending membrane) and are not damaged when an overpressure is applied. A disadvantage is that the output signal also depends on the type of gas. This can be overcome by combining the output signals of two (or more) sensors with different geometries, see e.g. [6],[42],[43].

Like other thermal sensors, thermal pressure sensors can benefit from miniaturization [44], [45]. The reduction of parasitic thermal losses and thermal time constants can yield lower power consumption and faster response. These benefits, as well as the prospect of providing single-chip sensing systems, have led to the development of a large number of micromachined thermal pressure sensors [43]-[46]. In most of these designs, the heat transport is perpendicular to the wafer surface and the silicon substrate acts as the heat sink, however there are also examples with lateral heat transport [25],[47].

The heater element can have many shapes, e.g. a cantilever beam [25], [48], a microbridge [6], [49]-[51], a suspended plate [44]-[45], [26], [52]-[55], a coil [47], or a membrane [56]. The gap between the heater and heat sink can be bulk micromachined, e.g. a V-groove under a microbridge [49]-[51] or a cavity under a suspended plate [44],[45], surface micromachined using a thin sacrificial layer [53]-[55], or it can be realized by bonding two wafers together [56]. An interesting technique to etch a shallow gap under a membrane was presented by Chou et al. and involves the use of (111)-oriented silicon wafers [55]. An extremely small Pirani sensor was realized by Puers et al. using focused ion beam (FIB) deposition and milling [46]. However, although the complete sensor structure is extremely small, the gap size between heater and heat sink is still 400 nm, which is larger than the gaps that can be fabricated by sacrificial layer etching [53]-[55].

The sensor presented in this chapter consists of a heated microbridge, which is placed above a V-groove in the substrate. The difference with existing sensors is that the temperature distribution is measured instead of the average temperature of the bridge. The shape of this temperature distribution depends on the pressure, which makes the small absolute temperature rise unimportant. This has the advantage that the measurement becomes independent of the Temperature Coefficient of Resistance of the temperature sensing resistors. Furthermore, the heat loss by conduction through the beam to the substrate is implicitly taken in account, which extends the lower pressure range.

Figure 4.1 shows a schematic drawing of the structure. A platinum heater is placed along the center of a thin silicon nitride carrier. Additional platinum leads are connected to the heater, dividing it into five segments. The voltage drop across each of these segments can be measured individually. The temperature dependent electrical resistance can be calculated from the voltage drop and the current through the heater. The average temperature of each segment is calculated from the change in electrical resistance of the segment. A discretized analytical model for fitting the average temperatures of the five segments is used to extract the pressure.

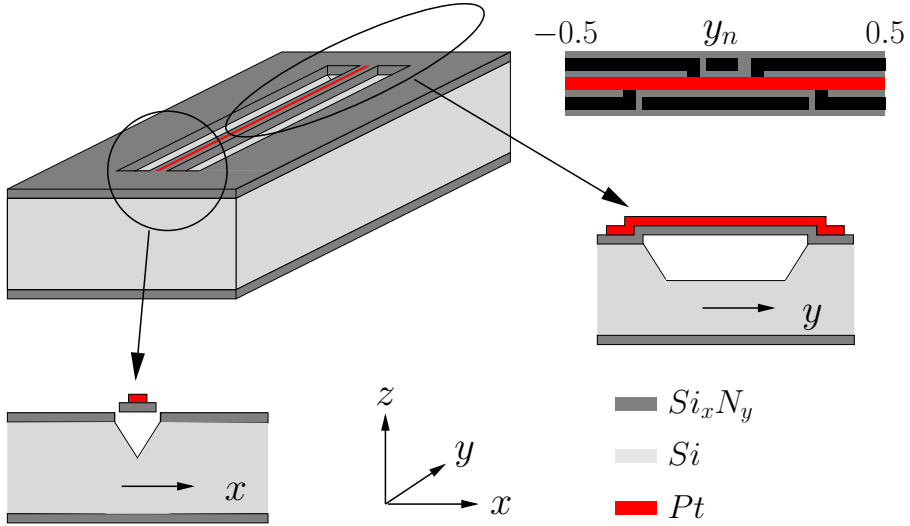


Figure 4.1: Schematic drawing of the structure

## 4.2 Theory

The pressure dependence of the heat transfer from a heater through a gas to a heat sink can be split up in three regions: molecular, viscous slip and viscous, as indicated in figure 4.2. From microscopic considerations of kinetic theory the following expression can be derived for the thermal conductivity  $\kappa$  [ $W/(Km)$ ] of an ideal, dilute gas [57]:

$$\kappa = \frac{1}{3} n \bar{v} c \lambda \quad (4.1)$$

with  $c$  [ $J/K$ ] the pressure independent specific heat per molecule,  $\bar{v}$  [ $m/s$ ] the mean molecular velocity,  $n$  [ $m^{-3}$ ] the number of particles per unit volume and  $\lambda$  [ $m$ ] the mean free path of the particles. The thermal conductivity of a gas, as a material property, does not change with pressure, since the pressure dependence of  $n$  and  $\lambda$  cancels. However, in a thermal conductivity pressure sensor it appears to change because the characteristic length of the system limits the mean free path. Thus, in the molecular region in figure 4.2, the characteristic length, i.e. the distance between the heater and heat sink, defines the mean free path and the thermal conductivity in this region is proportional to  $n$ .

The pressure dependence of the thermal conductance  $G_g$  [ $W/K$ ], measured between the heater and heat sink in a Pirani pressure sensor, can be described by the following expression [33]:

$$G_g = A_s K P \left( \frac{P_t}{P + P_t} \right) \quad (4.2)$$

where  $A_s$  [ $m^2$ ] is the effective surface area of the sensor,  $P_t$  [ $Pa$ ] is the transition pressure that depends on the characteristic length of the system and  $K$  [ $W/(K Pa m^2)$ ] is a constant that depends on the type of gas and the so-called accommodation effect,

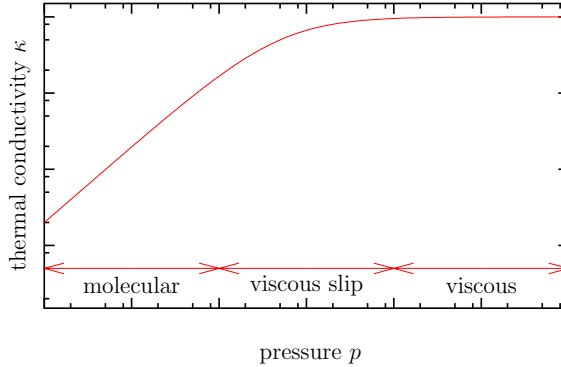


**Figure 4.2:** Measured thermal conductivity as a function of pressure (log-log plot)

which accounts for the fact that an average molecule colliding with a surface does not fully reach thermal equilibrium with that surface. It can be shown that for a simple parallel-plate sensor configuration the transition pressure  $P_t$  is inversely proportional to the distance between the plates [43], [50], but for practical sensor geometries this dependence is more complicated. Paul [25] compared the transition pressure for several geometries as a function of the gap distance  $d$  and found a dependence proportional to  $d^{-0.75}$ .

### 4.3 Model

The temperature profile  $T(y)$  along the length of the beam is dependent on the ratio of the heat transport through the gas to the heat transport through the beam. This is illustrated in figure 4.3 for an infinitesimal part  $dy$  of the beam. The temperature profile can be calculated by solving the following second-order differential equation, which describes the heat balance in a differential element of the microbridge [51], [1]:

$$-\frac{1}{R'_b} \frac{\partial^2 T(y)}{\partial y^2} + G'_f T(y) = P' \quad (4.3)$$

In this equation  $P'(y)$  is the electrical line power in  $[W/m]$  dissipated at position  $y$ ,  $G'_f$  is the line conductance through the gas in  $[W/(Km)]$ , so that the second term corresponds to the power flowing through the gas to the heat sink.  $R'_b$  is the thermal line resistance of the beam in  $[K/Wm]$ , so that the first term is the net power flowing through the beam away from  $y$ . By using the dimensionless normalized position  $y_n$ , ranging from -0.5 to 0.5, equation 4.3 transforms into:

$$-\frac{1}{R'_b l^2} \frac{\partial^2 T(y_n)}{\partial y_n^2} + G'_f T(y_n) = P' \quad (4.4)$$

with  $l$  [m] the length of the beam. The solution of equation 4.4 with the boundary conditions  $T(y_n = -0.5) = 0$  and  $T(y_n = 0.5) = 0$  is given by [1]:



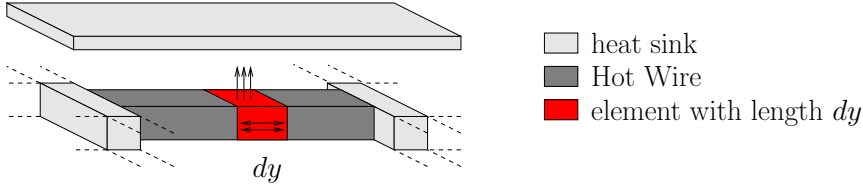


**Figure 4.3:** An infinitesimal part  $dy$  of the beam with heat conduction through the gas to the heat sink and heat conduction through the beam to the support

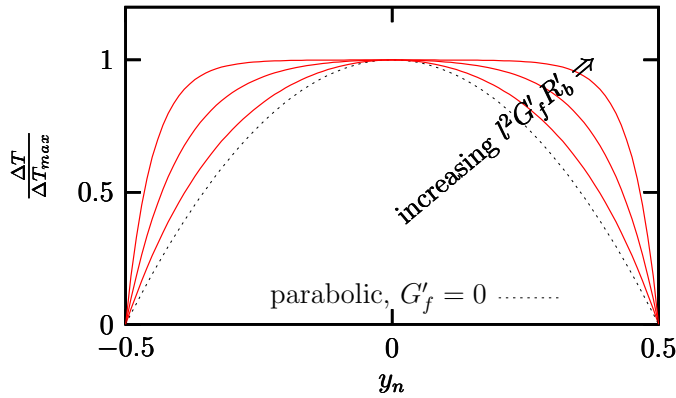


**Figure 4.4:** Normalized temperature distribution along the beam as function of the shape factor  $\sqrt{R'_b G'_f}$

$$T(y_n) = \frac{P'}{G'_f} \left( 1 - \frac{\cosh\left(y_n \cdot l \sqrt{R'_b G'_f}\right)}{\cosh\left(\frac{1}{2} l \sqrt{R'_b G'_f}\right)} \right) \quad (4.5)$$

Normalizing the temperature of equation 4.5 to the temperature at the center of the beam results in:

$$T_n(y_n) = \frac{T(y_n)}{T(0)} = \frac{\cosh\left(\frac{1}{2} l \sqrt{R'_b G'_f}\right) - \cosh\left(y_n \cdot l \sqrt{R'_b G'_f}\right)}{\cosh\left(\frac{1}{2} l \sqrt{R'_b G'_f}\right) - 1} \quad (4.6)$$

Figure 4.4 shows a plot of the normalized temperature distribution for values of the term  $l \sqrt{R'_b G'_f}$  ranging from 0 to 20. An important advantage of normalizing in this way is that the normalized temperature distribution can be measured independent of the exact value of the Temperature Coefficient of Resistance (TCR).

In a practical sensor the heater segments cannot be made infinitely small, and therefore it is not possible to measure the temperature in a single point. Instead the average temperature over a segment is measured. Integration of equation 4.5 over a segment and dividing it by the length of the segment results in the average

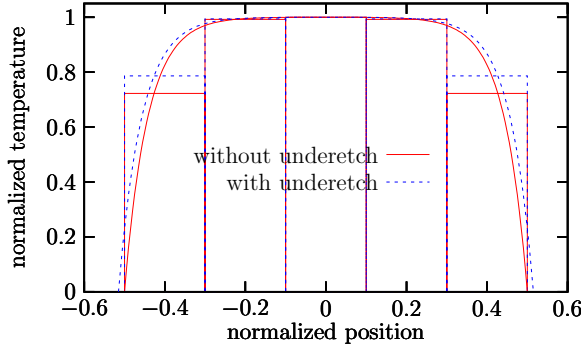


**Figure 4.5:** Average of the normalized temperature of the segments (4.8) and the normalized temperature distribution (4.6) with and without underetch.

segment temperature per unit applied line power  $[W/(Km)]$ . For a segment with lower boundary  $a$  and upper boundary  $b$ , which are both normalized to  $l$ , we have:

$$\frac{\bar{T}(a, b)}{P'} = \frac{1}{G'_f} \left( 1 - \frac{\sinh(b l \sqrt{R'_b G'_f}) - \sinh(a l \sqrt{R'_b G'_f})}{(b - a) l \sqrt{R'_b G'_f} \cosh\left(\frac{1}{2} l \sqrt{R'_b G'_f}\right)} \right) \quad (4.7)$$

Averaging the normalized temperature distribution of equation 4.6 over the length of the resistor segment gives:

$$\bar{T}_n(a, b) = \frac{\cosh\left(\frac{1}{2} l \sqrt{R'_b G'_f}\right)}{\cosh\left(\frac{1}{2} l \sqrt{R'_b G'_f}\right) - 1} - \frac{\sinh(b l \sqrt{R'_b G'_f}) - \sinh(a l \sqrt{R'_b G'_f})}{(b - a) l \sqrt{R'_b G'_f} (\cosh\left(\frac{1}{2} l \sqrt{R'_b G'_f}\right) - 1)} \quad (4.8)$$

Figure 4.5 shows a plot of the normalized temperature distribution (equation 4.6) together with the average temperature per segment (equation 4.8), which is indicated by boxes.

Due to underetch the beam length  $l$  will be somewhat larger than designed. The dashed curve in figure 4.5 illustrates the influence of this underetch. Equation 4.8 is used for interpretation of the measurement results using a realistic value for  $l$  to include the underetch.

### 4.3.1 Obtaining an estimate for the thermal line conductance

The easiest way to obtain an estimate for the thermal line conductance  $G'_f$  in equations 4.5 to 4.8 is by approximating the V-groove by a parallel plate configuration [26], as indicated in figure 4.6. An alternative is to use a lumped element model, which will be discussed below. In both cases only the heat transfer in the direction perpendicular to the beam is considered: heat transfer in the direction parallel to the beam is neglected.

The thermal line conductance  $G'_f$  depends on the pressure in exactly the same way as  $G_g$  in equation 4.2. In fact, we only have to replace the surface area  $A_s$  by the width  $w$  of the beam. Thus, we can write  $G'_f$  as:

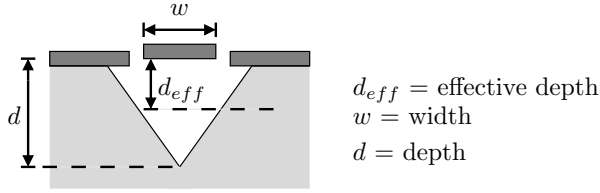


**Figure 4.6:** Cross section of the V-groove, with underetched support, and effective depth  $d_{eff}$

$$G'_f = wKP \frac{P_t}{P + P_t} \quad (4.9)$$

The depth of the V-groove under the beam is approximately  $45 \mu\text{m}$ . Therefore, for the parallel plate approximation an effective gap distance  $d_{eff}$  in the order of  $20 \mu\text{m}$  seems reasonable. In that case, the transition pressure  $P_t$  will be around 2 to 3 kPa [25], which is well below atmospheric pressure. Therefore, at atmospheric pressure we can simplify equation 4.9 considerably:

$$G'_f = wKP_t \quad (4.10)$$

Comparing equation 4.10 to the thermal conductance found by using the thermal conductivity  $\kappa_g$  of the gas, we find:

$$G'_f = w \cdot K \cdot P_t = \kappa_g \frac{w}{d_{eff}} \quad (4.11)$$

from which follows

$$K = \frac{\kappa_g}{d_{eff}P_t} \quad (4.12)$$

Thus for our sensor structure we have for nitrogen at atmospheric pressure:

$$\kappa_g = 26 \cdot 10^{-3} \text{ W}/(\text{Km})$$

$$w = 25 \mu\text{m}$$

$$K = 5 \cdot 10^5 \text{ W}/(\text{KPa m}^2)$$

$$G'_f = 0.03 \text{ W}/(\text{Km})$$

Of course, the parallel plate approximation only gives a very rough indication. Therefore, the lumped element model shown in figure 4.7 was used to obtain a better approximation.

In figure 4.7  $G_p$  and  $G_l$  represent the thermal conductances through the fluid in vertical and horizontal direction, respectively. The conductances  $G_c$  represent the silicon nitride flaps, the conductances  $G_b$  represent the beam and the conductances  $G_g$  represent the gap between the beam and the flaps. For each node in the lumped element model Kirchhoff's current law can be applied [58] resulting in the thermal

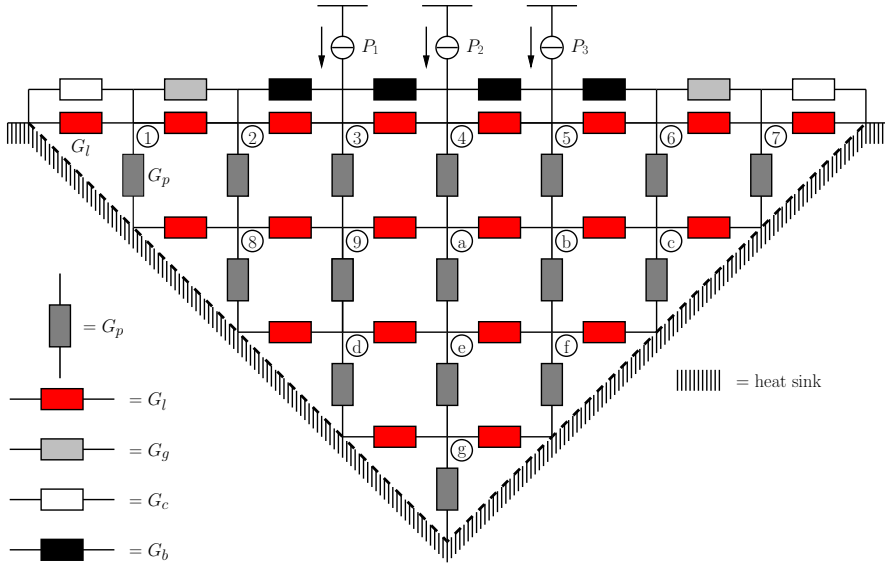


**Figure 4.7:** Lumped element model of the V-groove sensor. For simplicity only nine nodes are shown

conductance matrix  $G$ . Inverting this matrix and multiplying it with the power matrix  $P$  gives the temperature distribution matrix  $T$  in the V-groove under the beam.

Using a thermal conductivity of  $3 \text{ W}/(\text{Km})$  for silicon nitride [59] and  $71 \text{ (W/Km)}$  for platinum and using the fact that only 60% of the beam is covered by platinum, an effective thermal conductivity of  $10 \text{ W}/(\text{Km})$  is calculated for the beam. The ratio of the total applied power to the average temperature of the beam gives the effective thermal line conductance  $G'_f$ . In the model, this value is calculated by dividing each power source  $P_i$  by the temperature at the corresponding node and then adding the resulting conductance values. This results in a value of  $G'_f$  of  $0.15 \text{ W}/(\text{Km})$ , which is five times larger than the value obtained from the parallel plate approximation. However, this can be explained by the fact that the parallel plate approximation neglects the power flowing through the narrow gaps between the beam and the silicon nitride flaps.

Figure 4.8 shows a plot of the calculated temperature distribution in the V-groove. To have an idea of the shape of the temperature distribution a rough approximation of the term  $l\sqrt{R'_b G'_f}$  can be made. Using a value of  $3.6 \cdot 10^9 \text{ K}/(\text{Wm})$  for the thermal line resistance of the beam gives a value of 23. Thus, the temperature distribution will be slightly more uniform than the most uniform curve indicated in figure 4.3, which corresponds to a value of 20.

## 4.4 Realization

Figure 4.9 shows the process sequence used for fabrication of the sensor chips. The first step of the process is the deposition of a  $1 \mu\text{m}$  thick silicon nitride layer on a silicon

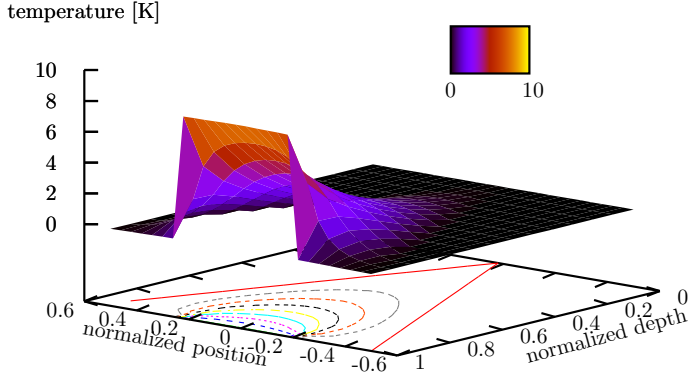


**Figure 4.8:** 2D Temperature distribution in the V-groove

$\langle 100 \rangle$  wafer, with a thickness of approximately  $380 \mu\text{m}$ . A special mask structure is used in combination with KOH-etching for precisely finding the crystallographic orientation [35]. This step is necessary because of the large length-to-width ratio of the V-groove. Slight misalignment results in a large underetch, giving a wider V-groove.

The next steps are selectively stripping of the silicon nitride layer and the deposition of a  $100 \text{ nm}$  thick sacrificial polysilicon layer. The latter is needed for underetching of the beam. After patterning the poly-Si layer a  $1 \mu\text{m}$  thick silicon nitride layer is deposited and patterned. A  $10 \text{ nm}$  chromium primary layer and a  $200 \text{ nm}$  platinum layer are sputtered and patterned by lift-off. Finally, KOH etching is used for releasing the beam. Normally, the KOH etching would stop at a depth of about  $21 \mu\text{m}$ . However, due to a very long etching time, which was required for other structures on the same chip [21], a significant underetch occurs. As a result, the realized V-grooves had a depth of approximately  $45 \mu\text{m}$ . This is not due to misalignment to the crystal orientation, because the underetch is the same along the entire length of the V-groove.

Figure 4.10 shows a photograph of the first two segments of a beam (with a total of five segments). The underetch is clearly visible. The carrier itself has a length of  $1 \text{ mm}$ , a width of  $25 \mu\text{m}$  and a thickness of  $1 \mu\text{m}$ . The platinum heater and voltage leads have a width of  $5 \mu\text{m}$  and a thickness of  $200 \text{ nm}$ .

## 4.5 Measurement results

As mentioned before, the voltage drop across each segment can be measured individually. To measure the resistance of a segment a current is applied to the heater and the resulting voltage drop is measured using additional leads. This four-point resistance measurement eliminates the voltage drop over the additional leads, because there is no current flowing in the voltage measurement leads. The polarity of the current is reversed periodically to eliminate thermo-electric disturbances. Figure 4.11 shows a plot of the resistance values for two different heating currents:  $30 \mu\text{A}$  and  $0.3 \text{ mA}$ .

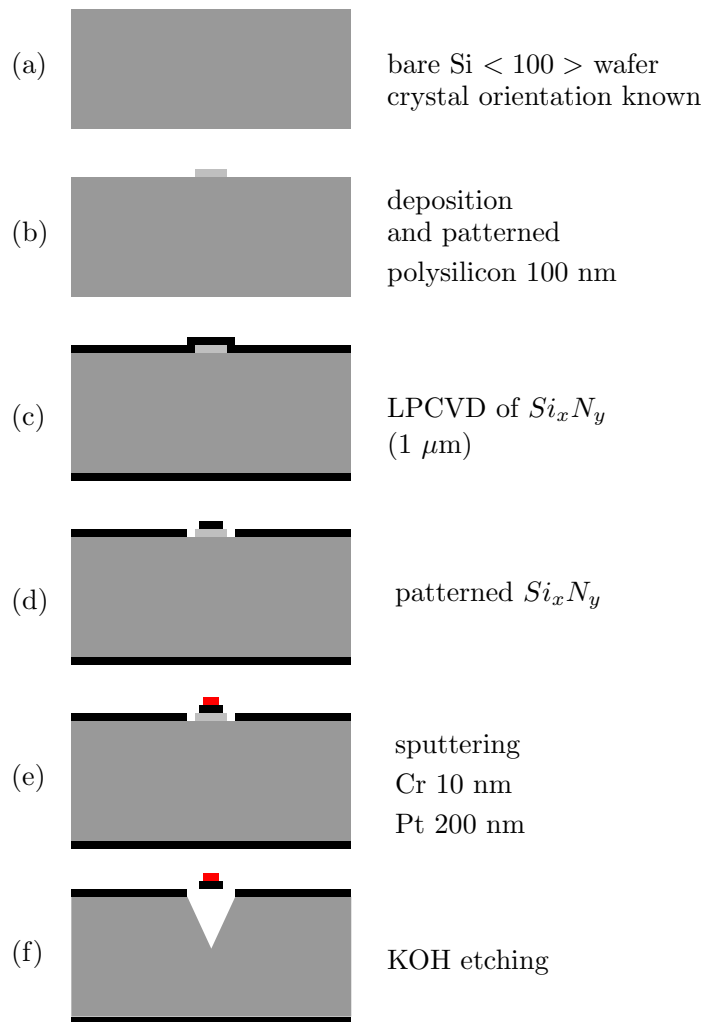


**Figure 4.9:** Summary of the fabrication process

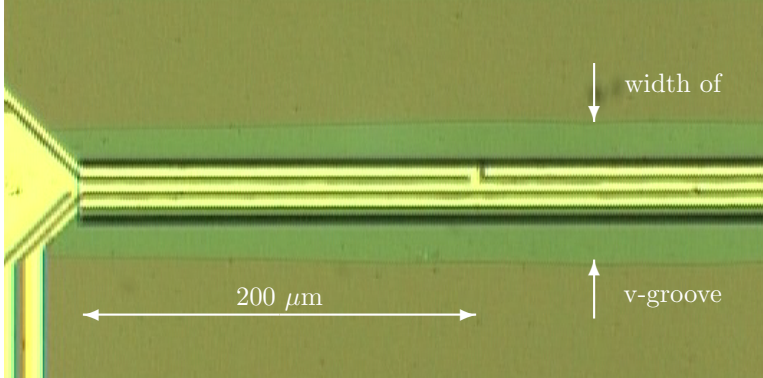


**Figure 4.10:** Photograph of part of the beam, showing the first two segments. Also the underetch is clearly visible.

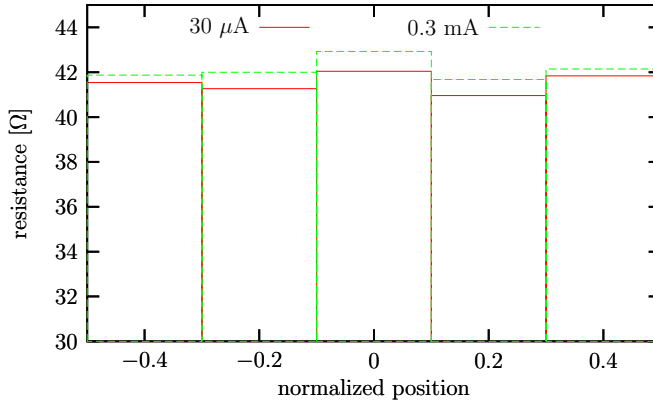


**Figure 4.11:** Measured segment resistances at currents of 30 and 300  $\mu\text{A}$  and a pressure of 3.5 Pa. The current dependence is due to the changing temperature.

The dependence on the applied current is due to the resulting change in temperature. The spread in resistance values is due to random variations of the platinum line-width due to the lift-off process.

From figure 4.11 we see that the spread in resistance values is larger than the effect of the temperature increase. This is typical for all measurements presented in this section and it is due to the small change in temperature (5 to 10 K) in combination with the small TCR ( $0.002 \text{ K}^{-1}$ ) of the platinum layer. Increasing the temperature change by applying a larger current would result in a larger signal, however, as mentioned in chapter 2, we want to keep the temperature change as small as possible to avoid any influence on the fluid parameters.

The relative change in resistance of the heated heater is a measure for the temperature. In figure 4.11 we see that this change is largest for the center segment, which has the highest temperature. To obtain the temperature of a segment we first need to know the resistance when there is no heating current applied. Therefore, the re-

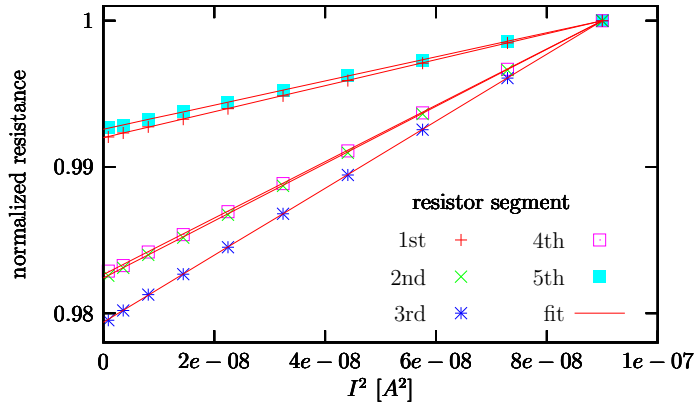


**Figure 4.12:** Measured segment resistances as a function of square of the current and normalized with respect to the value at  $30 \mu\text{mA}$ . A linear fit provides the extrapolated resistance at zero current, because the temperature rise is proportional to the power and, thus, to  $I^2$ .

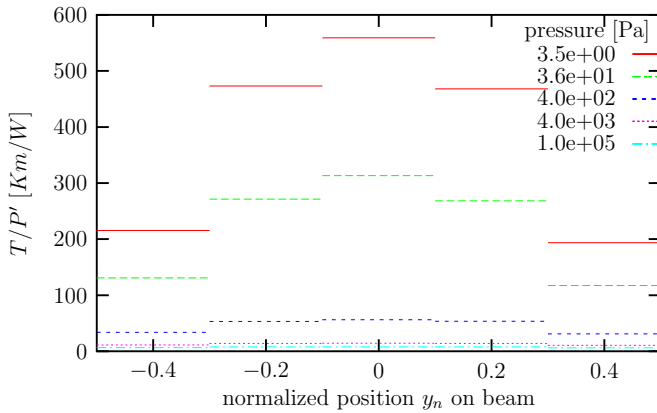


**Figure 4.13:** Measured segment temperatures per unit line power versus the position on the beam for several pressures



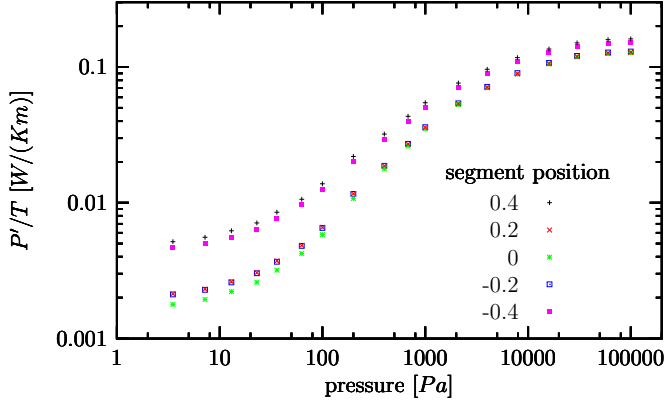


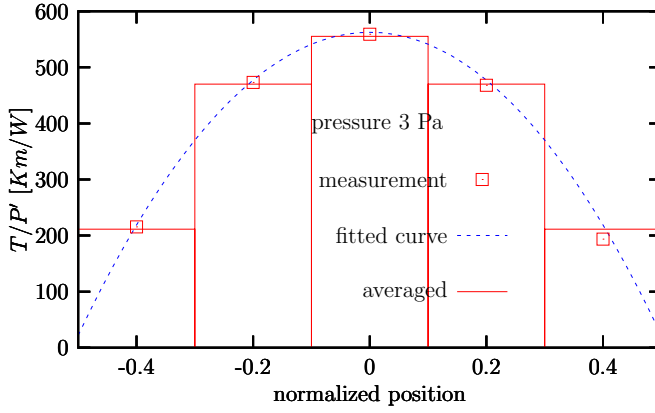
**Figure 4.14:** Measured ratio of the line power to the temperature rise as a function of the pressure for each segment

sistance is measured at several current levels as shown in figure 4.12. The resistance is linearly dependent on the temperature and, therefore, on the heating power. All curves are normalized to the value at a current of 0.3 mA. Extrapolation of the curves results in the resistance value at zero heating current.

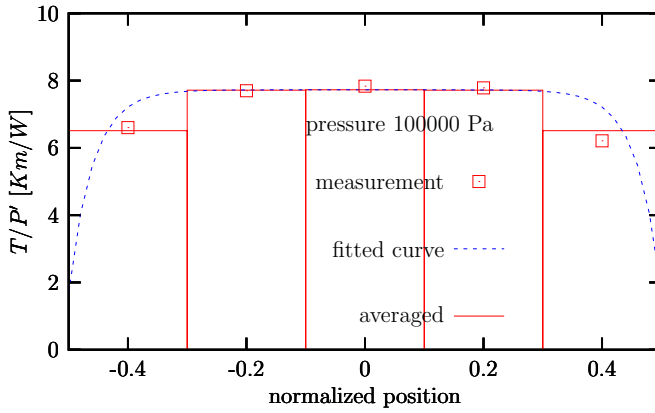
Measurements have been performed using nitrogen with the pressure ranging from 3.5 Pa up to atmospheric pressure. For the different pressures the applied power is adjusted in order to keep the maximum temperature rise between 5 and 10 K to prevent the change of the gas parameters. To eliminate the variation of the applied power in the plotted results, the measured temperatures are divided by the line power. The results are shown in figures 4.13 and 4.14. Figure 4.13 shows the segment temperatures per unit line power versus the position on the beam for several pressures. The change in shape of the temperature distribution is clearly visible. Figure 4.14 shows the ratio of line power to temperature rise as a function of the pressure for each segment. The bottom curve corresponds to the center segment and the top curves correspond to the outer segments of the beam. The two upper curves are not identical as would be expected. This is due to the fact that a cap was placed over the chip, which was needed for other structures on the same chip [21]. Misalignment of this cap causes a slightly asymmetrical temperature profile.

The curves in figure 4.14 are typical for Pirani pressure sensors. At high pressures we see that the sensitivity decreases due to the fact that the mean free path of the gas molecules becomes smaller than the gap distance in the sensor. This is the effect indicated in figure 4.2. At low pressures we see that the sensitivity also decreases. This is due to the fact that the heat transfer through the beam starts to dominate the heat transfer through the gas. Usually, a constant power is subtracted from the curves to compensate for the heat loss through the beam. We will see below that fitting the model presented in section 4.3 to the measured temperature profile also results in compensation of this heat loss.

Figures 4.15 shows the measured temperature distribution of figure 4.13 for 3.5 and  $10^5$  Pa, together with the corresponding distribution predicted by the model. For this purpose, the average temperature over each segment (equation 4.7) has been



(a)



(b)

**Figure 4.15:** Measured temperature distribution of figure 4.13 for (a) 3.5 and (b)  $10^5$  Pa, together with the temperature distributions predicted by the model from section 4.3.

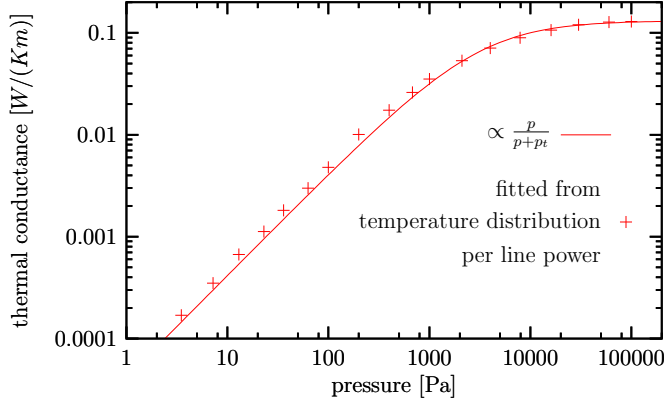


**Figure 4.16:** Thermal conductance as function of pressure obtained from the temperature distribution per line power.

fitted to the measurement data using an implementation of the nonlinear least-squares Marquardt-Levenberg algorithm, giving the thermal line conductance  $G'_f$  and beam resistance  $R'_b$ . The dashed curve is the resulting temperature distribution calculated using equation 4.5. For the thermal line resistance  $R'_b$ , a value of  $4.7 \cdot 10^9 \text{ K}/(\text{Wm})$  was found, which is slightly larger than expected. The pressure-dependent thermal line conductance  $G'_f$  is plotted in figure 4.16. The transition pressure  $P_t$  is  $2.5 \cdot 10^3 \text{ Pa}$ , which agrees very well with the expected value [25]. The thermal line conductance  $G'_f$  at atmospheric pressure is  $0.13 \text{ W}/(\text{Km})$ , which corresponds very well to the value of  $0.15 \text{ W}/(\text{Km})$  found by using the lumped element model.

The fit also indicates an effective elongation of the beam by  $20.5 \mu\text{m}$  at both ends due to underetch. In reality the underetch was  $40 \mu\text{m}$ , however, the difference can easily be explained by the fact that the underetching does not change the end points of the beam in the nitride layer and most of the heat will flow away sideways.

To obtain figure 4.16 we have used both the shape and the magnitude of the temperature distribution and to obtain the temperature values we needed the TCR of the platinum layer. We will now show that it is possible to obtain a similar result by only using the shape of the temperature distribution, thus canceling out the influence of the TCR. For this we divide the measured temperature by the temperature of the center segment. Figure 4.17 shows the resulting normalized temperature distribution using the measurement data from figure 4.12. This figure still clearly shows the change in shape due to the changing pressure, but can be obtained independent of the TCR. Figure 4.18 shows the results of fitting equation 4.8 to the measurement data. Note that in this case the product  $R'_b G'_f$  is fitted instead of the individual parameters, because in equation 4.8 the influence of  $R'_b$  and  $G'_f$  cannot be distinguished. The dashed line in figure 4.18 shows the calculated normalized temperature distribution using equation 4.6 with the fitted value for the product  $R'_b G'_f$ . Figure 4.19 shows a plot of the fitted product as a function of pressure and normalized to the value at atmospheric pressure. This plot is indeed very similar to figure 4.16.

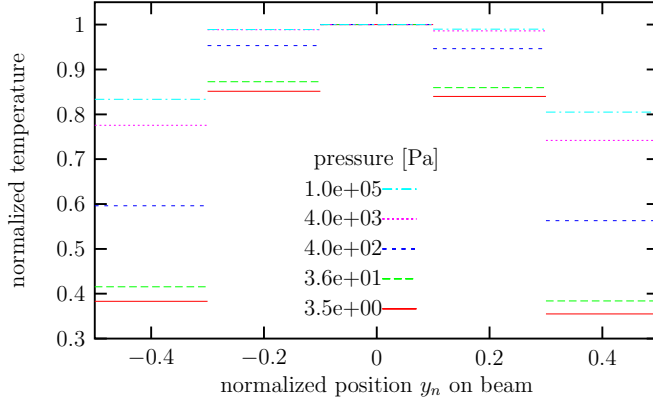
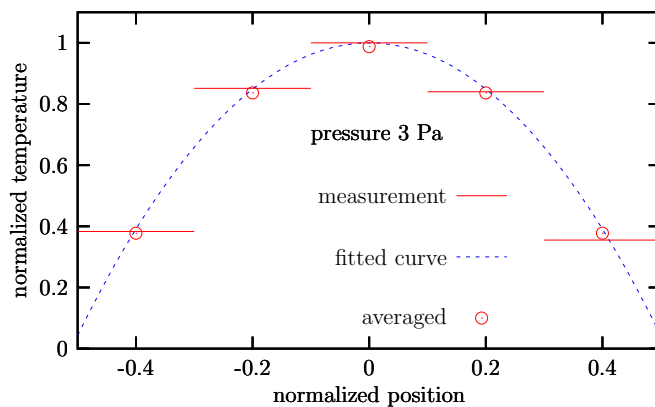


**Figure 4.17:** Measured temperature distribution normalized to the temperature of the center segment as function of the position on the beam.

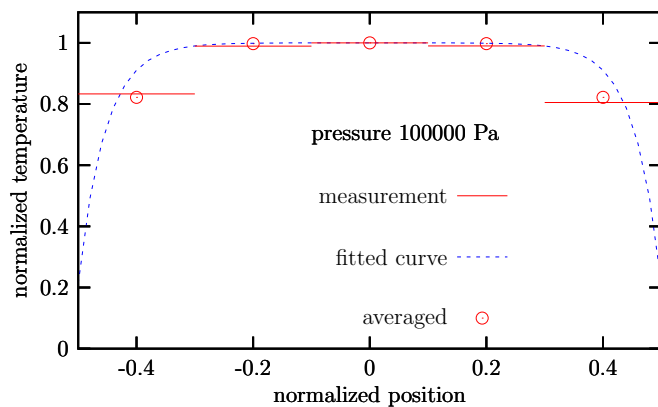
## 4.6 Conclusions

A Pirani pressure sensor consisting of a heated beam with distributed temperature sensing above a V-grooved heat sink has been realized. Compared to a sensor that measures only the average temperature of the beam, the advantages are the independence from the Temperature Coefficient of Resistance (TCR) of the sensors on the beam and the intrinsic compensation for the heat loss through the beam. The first advantage is due to the normalization of the temperature distribution to the temperature rise at the center, which eliminates the TCR. The second advantage is due to the fact that the model that is used to describe the temperature distribution takes into account the heat transfer through the beam to its support.

It was shown that even though the temperature measurements cannot be performed in a single point but are averaged over a resistor segment, it is still possible to accurately measure the temperature distribution by including the averaging effect in the model. The realized sensor has been tested for pressures ranging from 3.5 to  $10^5$  Pa. The measured transition pressure of  $2.5 \cdot 10^3$  Pa corresponds very well to the expected value. The transition pressure can be increased by using a smaller gap size, as will be demonstrated in the next chapter.



(a)



(b)

**Figure 4.18:** Measured normalized temperature distribution for a pressure of (a) 3.5 and (b)  $10^5$  Pa, together with the normalized temperature distributions predicted by the model from section 4.3.

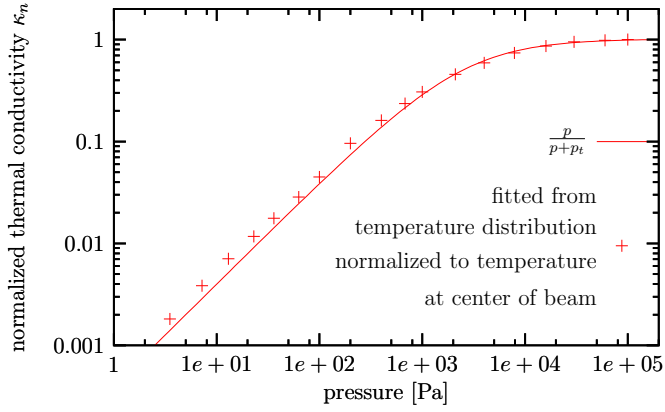


**Figure 4.19:** Normalized thermal conductivity as a function of pressure obtained from the normalized temperature distribution.

# Chapter 5

## Combined -Pirani/bending membrane- pressure sensor

In the previous chapter a Pirani pressure sensor was realized consisting of a beam suspended above a bulk-micromachined V-groove. This sensor was originally designed to measure thermal conductivity and, therefore, had a relatively low transition pressure. In this chapter a similar sensor is presented with a much smaller gap between heater and heat sink, so that the absolute pressure measurement range is extended to atmospheric pressure levels. Furthermore, the heater is realized on a membrane, which can bend due to an applied pressure difference. As a result, the distance between heater and heat sink changes and, thus, the sensor can also be used to measure pressure differences.

### 5.1 Introduction

Two distinct classes of pressure sensors are formed on one hand by bending membrane pressure sensors, where a pressure difference results in a membrane deflection, and on the other hand by thermal pressure sensors, where the thermal conductivity of a gas is used as a measure for the absolute pressure. In this chapter a sensor is presented, which combines these two measurement principles. As a result, the sensor can be used for simultaneous measurement of a pressure difference and the absolute pressure.

In the case of bending membrane pressure sensors, the membrane deflection is usually measured using a change in electrical capacitance or by integrating strain gauges in the membrane [12]. An alternative is to measure the thermal conductance between the membrane and a heat sink placed at a close distance. This was demonstrated in [18], where a heater was integrated on the membrane and the membrane temperature was measured using thermopiles. The heat sink was realized by bonding a second wafer on top of the wafer containing the membrane. The distance between the heated membrane and heat sink was in the order of 10  $\mu\text{m}$ .

The sensors presented in this chapter have a much smaller distance between membrane and heat sink, which is essential for using the structure to measure absolute pressure levels around atmospheric pressure. Furthermore, the sensor can be realized

in a simple and reliable fabrication process based on etching of a sacrificial poly-Si layer between two silicon nitride layers [60], [61].

Several sensor types have been realized, with membrane diameters ranging from 80 to 240  $\mu\text{m}$ . Three different heater designs were used:

- Single spiral  
In this case the membrane contains a single platinum heater spiral which is used for both heating and temperature measurement.
- Double spiral  
In this case the membrane contains two platinum spirals, so that the heating and sensing functions can be separated.
- Meandering heater  
In this case the membrane contains a single meandering heater which is divided into a number of segments so that the temperature profile across the membrane can be measured. As discussed in the previous chapters, this has the advantage that the measurement can be made independent of the Temperature Coefficient of Resistance (TCR). Furthermore, by measuring the temperature profile it should be possible to distinguish between the influence of absolute and differential pressure changes.

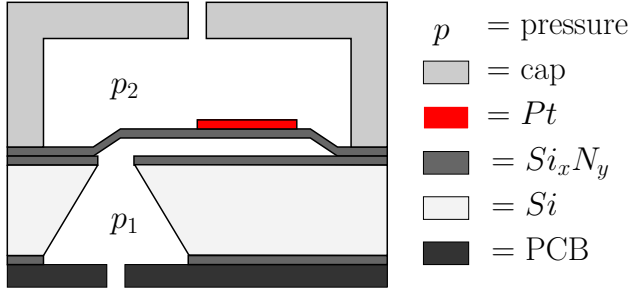
## 5.2 Operation principle

Figure 5.1 shows the basic structure of the sensor. It consists of a circular silicon nitride membrane positioned 1  $\mu\text{m}$  above the silicon substrate. A channel connects the cavity below the membrane with a hole at the backside of the wafer. Thus, a pressure difference between the front and backside of the wafer causes the membrane to bend. A platinum resistor is integrated on top of the membrane and acts both as heater and as temperature sensor. An identical platinum resistor on the substrate is used as a reference sensor. When a constant current through the electrical resistor heats the membrane the resulting membrane temperature, with respect to the substrate, is dependent on both the distance from the substrate, i.e. the membrane deflection, and the pressure dependent thermal conductivity of the medium between the membrane and substrate. In principle the thermal readout is suitable for operation at high temperatures, because the temperature difference between the membrane and the substrate is measured, which is in first order approximation independent of the absolute temperature [18].

The temperature distribution over the membrane is defined by the ratio of the heat transport through the medium to the heat transport through the membrane to the edge of the membrane. In the case that the membrane is uniformly heated, not deflected, and that the heat transport through the medium is much larger than the heat transport through the membrane we can assume that the membrane has a uniform temperature. Then, the thermal resistance between the heated membrane and the substrate can be expressed by:

$$\frac{\Delta T}{Q} = R_{therm} = \frac{l}{\kappa_f A} \quad (5.1)$$





**Figure 5.1:** Schematic drawing of the structure

where  $l$  [m] is the distance between membrane and substrate,  $A$  [ $m^2$ ] is the area of the membrane, and  $\kappa_f$  [ $W/(Km)$ ] is the effective thermal conductivity of the fluid, which is dependent on both the pressure and the distance  $l$ , as described in the previous chapter.

Equation 5.1 provides a simple but very rough indication of the membrane temperature as a function of the applied power. Especially at low pressures the membrane temperature will not be homogeneous and we have to solve the following differential equation to obtain the membrane temperature as a function of the distance  $r$  [m] from the membrane center for a non-deflected membrane (see also in [62]):

$$-h\kappa_s \left( \frac{d^2T}{dr^2} + \frac{1}{r} \frac{dT}{dr} \right) + \frac{\kappa_f}{l} T = Q'' \quad (5.2)$$

In this equation,  $\kappa_s$  [ $W/(Km)$ ] is the thermal conductivity of the solid membrane,  $h$  [m] is the membrane thickness and  $Q''$  [ $W/m^2$ ] is the applied heating power per unit area.

Using as boundary conditions that the temperature at the radius  $R$  [m] of the membrane is equal to the substrate temperature, i.e.  $T(R) = 0$ , and that there is no temperature gradient in the center of the membrane,  $\frac{dT(0)}{dr}$ , the following solution is found:

$$T(r) = \frac{Q''}{G_f''} \left( 1 - \frac{\text{BesselJ}_0 \left( r \sqrt{-G_f'' R_s''} \right)}{\text{BesselJ}_0 \left( R \sqrt{-G_f'' R_s''} \right)} \right) \quad (5.3)$$

where  $G_f'' = G_f/l$  [ $W/(Km^2)$ ] is the thermal square conductance through the fluid, and  $R_s'' = 1/(\kappa_s h)$  [ $K/W$ ] is the thermal square resistance of the membrane. Equation 5.3 is plotted in figure 5.2 indicating the temperature distribution for zero pressure difference, i.e.  $p_1 - p_2 = 0$  Pa.

When a pressure difference is applied over the membrane, it will bend and the distance  $l$  changes. For a circular membrane the deflection  $w$  [m] is given by [12]:

$$w(r) = \frac{3}{16} \frac{1 - \nu^2}{Eh^3} (R^2 - r^2)^2 \cdot \Delta p \quad (5.4)$$

with  $\nu$  the Poisson ratio,  $E$  the Young's modulus, and  $\Delta p$  the pressure drop. For a deflected membrane, equation 5.3 is difficult to solve. Instead, the lumped element

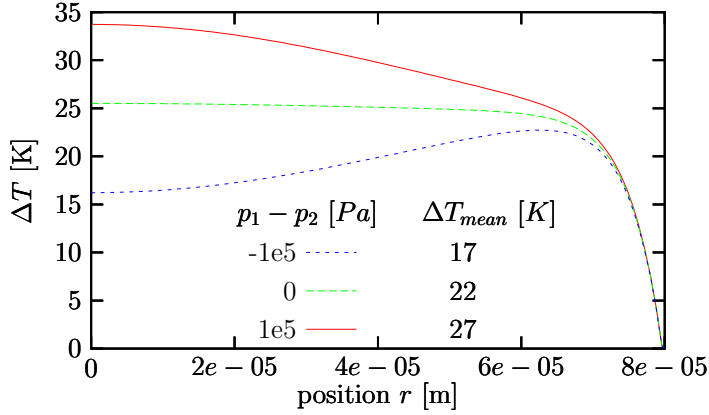


**Figure 5.2:** Calculated temperature distributions for a non-deflected (middle curve, calculated using equation 5.3) and deflected membrane (top and bottom curve, calculated using the lumped element model from figure 5.3).

model indicated in figure 5.3 is used to calculate the temperature distribution. The basic structure of the model is similar to the lumped element models presented in the previous chapters. The most important difference is that we now use a circular symmetry: the left part of figure 5.3 represents the center of the membrane ( $r = 0$ ) and the right part of the figure corresponds to the edge of the membrane ( $r = R$ ).

In the lumped element model, the heat conductance through the membrane is represented by the conductances indicated by  $G_{si}$  [W/K]. An expression for these conductances is obtained by solving the heat equation without heat generation [34]:

$$\frac{1}{r} \frac{d}{dr} \left( \kappa_s r \frac{dT}{dr} \right) = 0 \quad (5.5)$$

Combining the solution with Fourier's law results in:

$$G_{si} = \frac{2\pi h \kappa_s}{\ln \left( \frac{r_{i+1}}{r_i} \right)} \quad (5.6)$$

with  $i$  the index of the element.

The heat conductance through the fluid to the substrate is modeled by the conductances  $G_{fi}$  [W/K], which are dependent on the membrane deflection. An expression for these conductances is easily found by using the reciprocal of equation 5.1:

$$G_{fi} = \kappa_f \frac{\pi (r_i^2 - r_{i-1}^2)}{l} \quad (5.7)$$

The dissipated power is given by:

$$P_i = \pi (r_i^2 - r_{i-1}^2) Q'' \quad (5.8)$$

Figure 5.2 shows the calculated temperature distributions for an upward and downward deflection of the membrane (top and bottom curve, respectively). As discussed

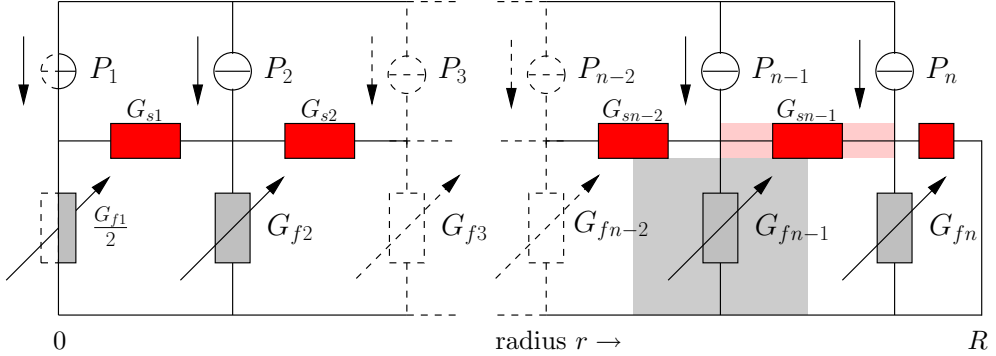


**Figure 5.3:** Lumped element model used for calculating the temperature distribution of a deflected membrane.

in chapter 4, the thermal conductance through the fluid becomes dependent on the absolute pressure when the distance between the heated membrane and the substrate is smaller than the mean free path of the molecules. Around atmospheric pressure this effect becomes noticeable when the distance is in the order of  $1 \mu\text{m}$ . The effect can easily be included in the lumped element model by inserting a pressure dependent term in equation 5.7.

## 5.3 Fabrication process

In [60] it was shown that sacrificial poly-Si etching can be used to create very long channels (several millimeters long,  $10\text{-}80 \mu\text{m}$  wide and  $1 \mu\text{m}$  high). For the combined Pirani/bending membrane sensor this technique is used in combination with anisotropic KOH etching from the backside of the wafer. Etching starts at the backside and continues through the entire wafer. When the front side of the wafer is reached the poly-silicon sacrificial layer is etched. In this way, silicon nitride membranes are realized on the surface of the wafer with the cavity connected by a channel to the etch opening at the backside of the wafer. The process appears to be very reproducible and results in high yield. A very long KOH etching time of approximately 19 hours is needed, but no negative effects of this have been detected. An important advantage compared to other sacrificial layer processes is that it is not necessary to seal etching channels needed to have access to the sacrificial layer. The hole on the backside can easily be closed or connected to a tube.

Figure 5.4 shows a summary of the fabrication process. The process starts by deposition (LPCVD) of a low stress  $\text{Si}_x\text{N}_y$  layer on a bare silicon (100) wafer (a). The layer is patterned by plasma etching to form the hole that will later connect the cavity under the membrane to the hole at the backside of the wafer (b). Next, a  $1 \mu\text{m}$  thick polysilicon sacrificial layer is deposited and patterned that defines the gap between the membrane and silicon substrate (c). The polysilicon and silicon nitride layers that are deposited on the backside of the wafer are stripped. Next, a second low stress  $\text{Si}_x\text{N}_y$  layer is deposited that forms the membrane on the front side. On the backside the layer is patterned to serve as etch mask during the final KOH etching

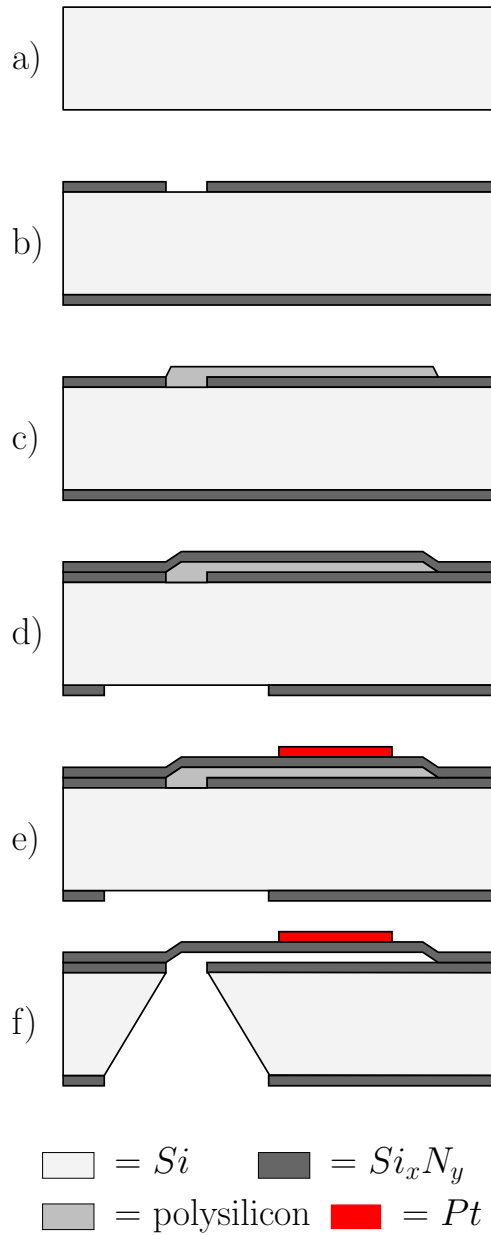


**Figure 5.4:** Process outline

step (d). Next, a 10 nm Cr adhesion layer and 200 nm Pt layer are sputtered and patterned by lift-off (e). The last step is the etching in KOH (f).

Membrane diameters ranging from 80 to 240  $\mu\text{m}$  with a thickness of 1  $\mu\text{m}$  have been realized. The gap between membrane and heat sink was 1  $\mu\text{m}$  (defined by the poly-Si sacrificial layer). The metal heater/sensor on top of the membrane consists of a 10 nm Cr adhesion layer and a 200 nm Pt layer, with a width and spacing between the lines of 5  $\mu\text{m}$ . Note that the same fabrication process can be used to realize a strain gauge or capacitive readout simply by changing the platinum pattern. Different readout principles can even be combined on a single chip.

Figure 5.5 shows photographs of three different sensor structures: with a single heater/sensor resistor, with separate heater and sensor, and with segmented heater/sensor for measuring the temperature distribution.

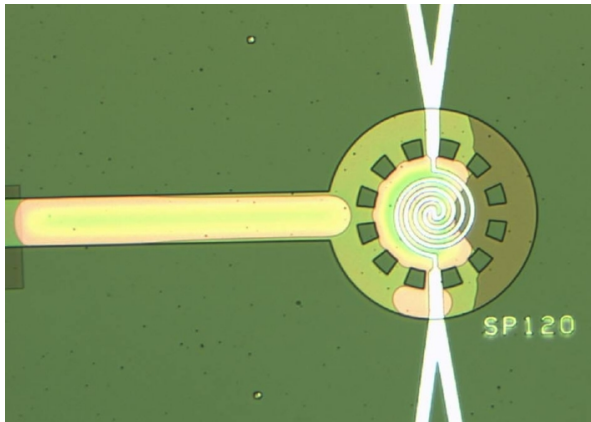
## 5.4 Measurement results

### 5.4.1 Single heater/sensor device

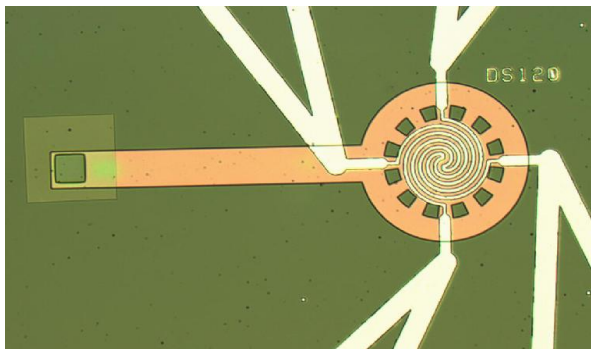
A sensor containing a membrane with a diameter of 160  $\mu\text{m}$  and a single heater/sensor spiral was tested at several applied pressures. The results are shown in figure 5.6. The membrane was heated by a current of 4.5 mA. As before, the polarity of the current is periodically reversed in order to eliminate the influence of thermo-electric disturbances. The resistance of the heater was approximately 600  $\Omega$ , so that the total heating power was about 12 mW. The resulting average temperature rise at atmospheric pressure was 23 K.

Figure 5.6(a) shows the measured change in the average temperature as a function of the applied pressure. Pressure is applied in three different ways:

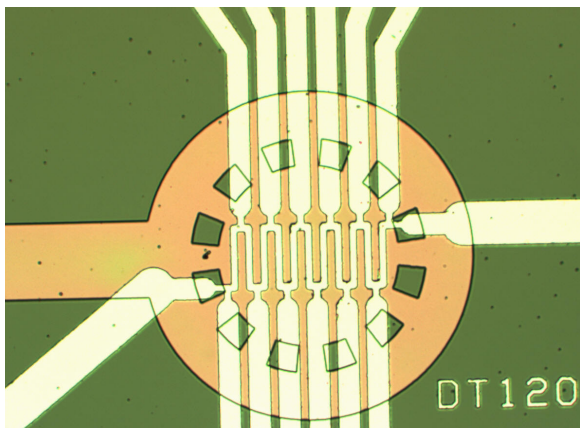
- Above the membrane  
In this case the pressure below the membrane  $p_1$  is equal to atmospheric pressure and an overpressure is applied above the membrane so that the membrane will deflect downwards. The measured temperature is shown by the curve labeled  $\Delta p = p_2 - p_1$  in the figure. We see that the temperature decreases with pressure because the distance to the substrate decreases.
- Below the membrane  
In this case an overpressure is applied under the membrane and  $p_2$  is kept at atmospheric pressure. The measured temperatures are labeled as  $\Delta p = p_1 - p_2$ . We see that in this case the temperature increases with pressure due to the increasing distance from the substrate. We also see that the dependence is not linear and not as strong as in the previous situation. This is due to the Pirani effect: due to the higher pressure under the membrane the thermal conductivity increases which partly compensates the effect of the larger distance.
- At both sides of the membrane  
In this case the overpressure is applied at both sides of the membrane. The membrane will not deflect because the pressure difference is zero. Thus, we now measure only the Pirani effect. In figure 5.6 these measurements are marked as  $\Delta p + 1e5 = p = p_1 = p_2$ . We see that the temperature decreases with



(a)

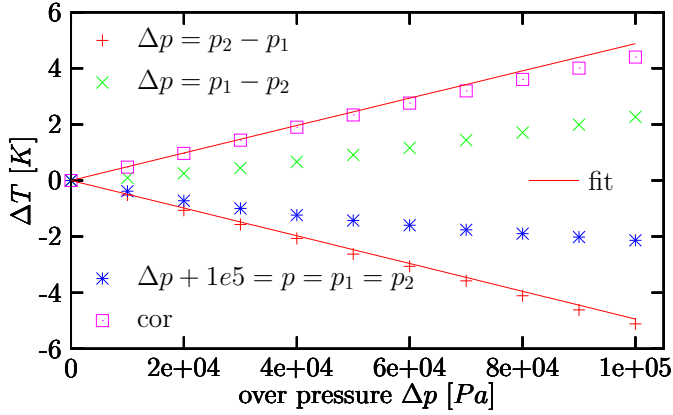


(b)

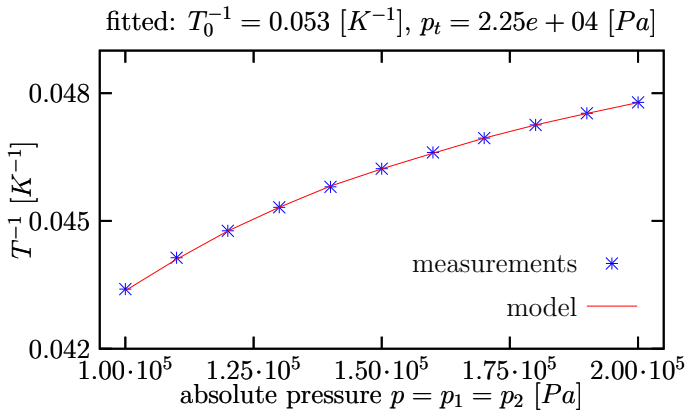


(c)

**Figure 5.5:** Photographs of three different sensor structures: (a) with a single heater/sensor resistor, (b) with separate heater and sensor, and (c) with segmented heater/sensor for measuring the temperature distribution. Photograph (a) was made during KOH etching and clearly shows the hydrogen bubble formation under the membrane.



(a)



(b)

**Figure 5.6:** Measurement results for a device with a single heater/sensor spiral (see text): (a) measured temperature change as a function of applied pressure for pressures applied above, below and at both sides of the membrane, and (b) the reciprocal value of the measured temperature as a function of absolute pressure.

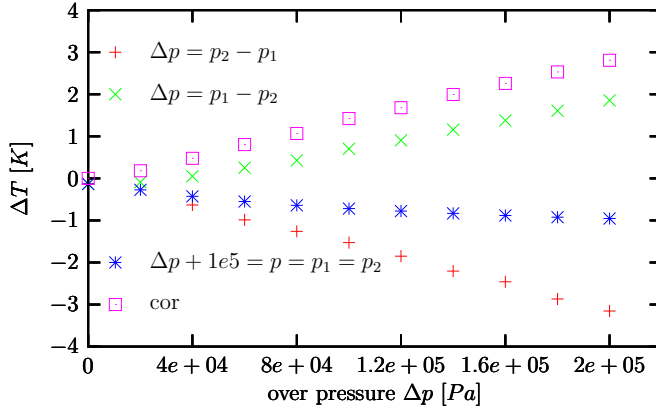


**Figure 5.7:** Measurement temperature change of the center segment of a distributed heater/sensor as a function of applied pressure

pressure due to the increasing thermal conductivity. The same data is plotted in figure 5.7 together with a fitted first order pressure dependence. The fitted transition pressure  $P_t$  is  $2.3 \cdot 10^4$  Pa, which corresponds very well with the value predicted by [25].

Correcting the measurement obtained by applying the pressure below the membrane for the change in thermal conductivity, i.e. subtracting the values obtained by applying the pressure at both sides from this measurement, gives the data labeled as “cor”. We see that the corrected data is, apart from the sign, almost identical to the data obtained by applying the pressure above the membrane. This shows that the membrane deflection is symmetrical. The small deviation is explained by the fact that the correction is not perfect since the Pirani effect changes a little bit due to the deflection of the membrane.

## 5.4.2 Distributed temperature measurement

For measurement of the temperature distribution a device was used with a membrane diameter of  $120 \mu\text{m}$  and a meandering heater/sensor element consisting of eleven segments. First, the previous measurements were repeated for the distributed device with the difference that now the temperature at the center of the membrane was measured instead of the average temperature. A heating current of 3 mA was used. The heater resistance was  $125 \Omega$ , resulting in a heating power of 1.1 mW. Still, the resulting temperature rise of the center heater segment is approximately 8 K at atmospheric pressure. Note that the heating power is almost a factor of 12 smaller than in the previous case with the spiral-shaped heater, but that the difference in temperature rise is only a factor of 3. This is due to the fact that the membrane is smaller ( $120$  instead of  $160 \mu\text{m}$  diameter) and that a relatively long part of the spiral heater is close to the edge of the membrane with a relatively low temperature.

Figure 5.7 shows the measured temperature change as a function of pressure for pressures applied above, below and at both sides of the membrane. As expected, the



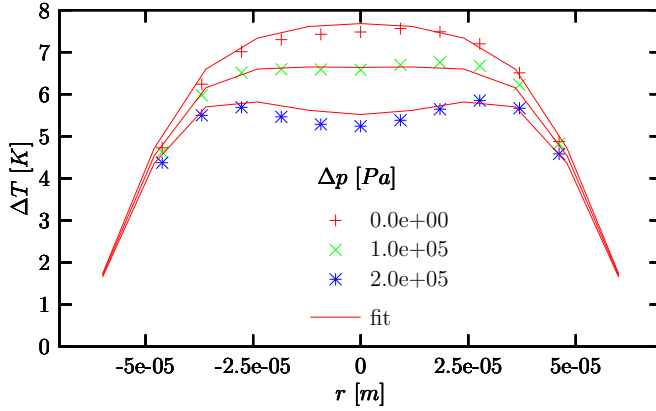


**Figure 5.8:** Measurement temperature distribution for different pressures applied above the membrane. The downward deflection of the membrane causes a decrease of the temperature with increasing pressure. Equation 5.3 was fitted to the data giving the plotted curves.

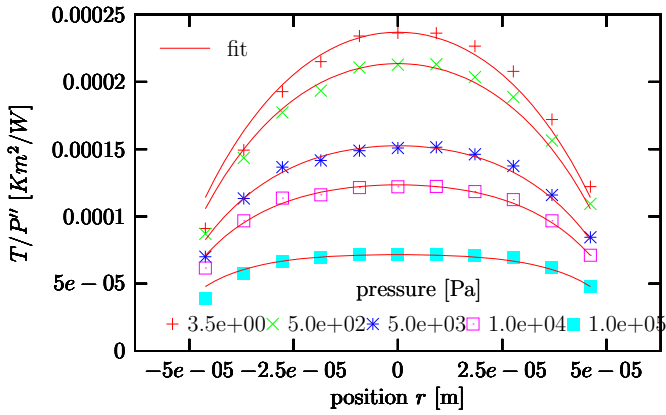
result is very similar to figure 5.6(a) for the spiral-shaped heater.

Figure 5.8 shows the measured temperature distribution as a function of pressure applied above the membrane. The pressure difference causes a deflection of the membrane towards the substrate, resulting in a decrease in temperature with increasing pressure. The membrane deflection is the strongest at the center, resulting in the local minimum in the temperature distribution at higher pressures. The curves in the figure were obtained by fitting equation 5.3 to the measured data.

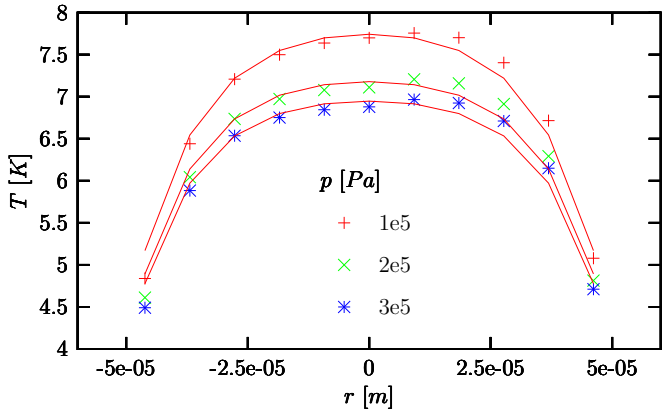
### 5.4.3 Operation as absolute pressure sensor

The temperature distributions were measured as a function of absolute pressure, applied at both sides of the membrane. In that case the membrane does not deflect and operates as a Pirani absolute pressure sensor. Figure 5.9(a) was obtained for pressures down to 3.5 Pa by placing the device in a vacuum chamber. In this case the heater power had to be adjusted in order to keep the maximum temperature rise between 5 and 10 K. Therefore, the figure shows the temperature change divided by the applied power per surface area ( $Q''$  in equation 5.3). Figure 5.9(b) shows the measured temperature distribution at higher pressures. In that case the heater current was equal to 3.5 mA for all pressures.

Fitting equation 5.3 to the data in figure 5.9 gives a value for the thermal conductance through the fluid per unit area  $Gf'' = G/A[W/(Km^2)]$ . The fitted curves are also shown in the figure. To obtain a good fit a correction factor was needed: the position of the heater segments  $r$  was multiplied by 0.92. Furthermore, the conductivity of the membrane,  $\kappa_s$ , resulting from the fit was  $2 W/(Km)$ , which is 30% lower than the value found for the beam structure in chapter 4. These deviations are due to the fact that equation 5.3 is based on a homogeneously heated membrane. In the actual sensor this is certainly not the case and a more accurate model should be developed. Still, the calculated temperatures and the values found for  $G_f''$  seem to give a good indication of the actual values. Figure 5.10 shows a plot of the fitted values of  $G_f''$  for



(a)



(b)

**Figure 5.9:** Measured temperature distributions as a function of absolute pressure. The same pressure is applied at both sides of the membrane so that the deflection is zero and the sensor operates as a Pirani pressure sensor. The fits are obtained from equation 5.3.

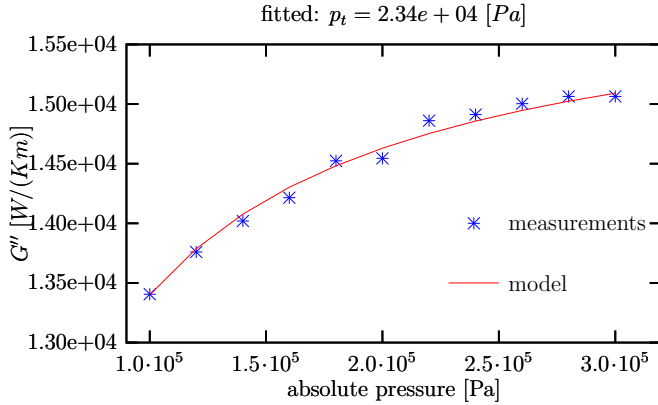


**Figure 5.10:** Fitted thermal conductance through the fluid per unit area obtained from the data from figure 5.9(b).

pressures ranging from  $10^5$  to  $3 \cdot 10^5$  Pa. The transition pressure obtained from this figure is  $2.3 \cdot 10^4$  Pa, which corresponds to the value found for the membrane with spiral-shaped heater, which is heated much more homogeneously.

Applying several pressures from below results in the temperature distributions of figure 5.11. The curves are the superposition of the curves from figure 5.8 and 5.10.

Normalizing the temperature distribution of figure 5.8 to the center segments shows the change of the shape as function of the pressure difference, see figure 5.12. The temperature coefficient of resistance has been eliminated.

## 5.5 Conclusions

Combined Pirani/bending membrane pressure sensors with various heating/sensing structures have been realized. First measurement results confirm that the sensor is sensitive to both absolute pressure and pressure difference. The former causes a change in the thermal conductance through the narrow gap between the heated membrane and the substrate. The latter causes a bending of the membrane, which results in a changing distance between the membrane and the substrate. A simple lumped element model has been presented that describes the two effects. However, especially in sensor allowing distributed temperature measurements the membrane heating is not uniform. This results in discrepancies between the model and measurement results. A more accurate model should be developed to be able to distinguish between the influence of absolute and differential pressure changes.

As shown in the previous chapters, using the temperature distribution instead of the actual temperature in principle allows cancellation of the influence of the temperature coefficient of resistance. This should be further investigated for the sensors presented in this chapter. Furthermore, it may be sufficient to measure the temperature only in a few strategically chosen positions on the membrane. This should also be further investigated.

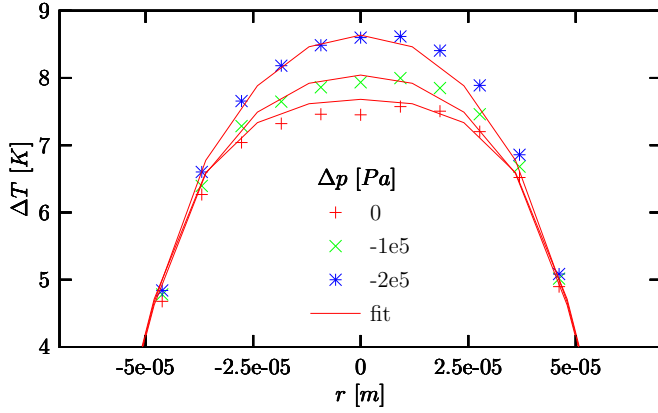


**Figure 5.11:** Measured temperature change as a function of the pressure drop applied over the membrane, including pressure dependent thermal conductivity

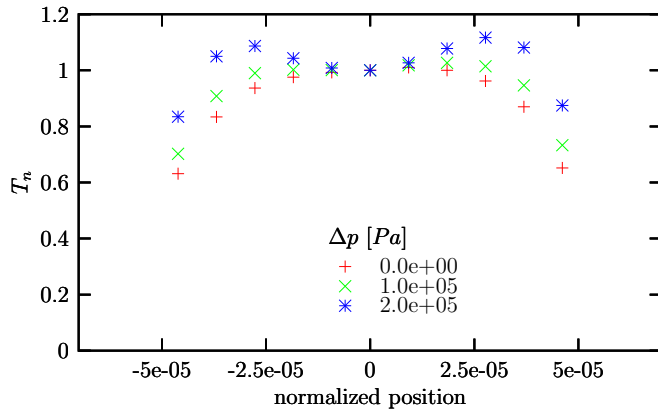


**Figure 5.12:** Plot of figure 5.8 normalized to the temperature rise of the center segment, which makes it independent of the TCR

# Chapter 6

## TCR and kinematic viscosity sensors

In this chapter two more sensors will be discussed. These sensors are necessary to realize the complete measurement scheme presented in chapter 2. However, due to time limitations these sensors have only been designed and fabricated, but so far no measurements have been performed.

### 6.1 Introduction

In this chapter designs of the TCR and the kinematic viscosity sensors will be discussed and the photographs of the structures will be shown.

For the TCR sensor two versions with distributed temperature sensing have been designed: one with a heater along the beam and one with a heater only at the center. Both make use of the properties of silicon and the assumption that the heat transfer through the beam is dominant over the heat transfer to the fluid.

Two versions of the kinematic viscosity sensor will be shown: one with one segment at the center and one with five segments along the beam. The membrane in the hexagonal channel is formed by several beams with heaters. The temperature distribution is difficult to model analytically. Therefore currently a student is simulating in a FEM package the flow profile and the temperature distribution of the membrane.

### 6.2 TCR-sensor

With the TCR-sensor we want to obtain the TCR of the platinum layer. Therefore we need a structure with a known and stable temperature distribution. The TCR sensor consists of a thick beam with a heater on top of it, see figure 6.1. The beam is thick to fulfill the assumption that the heat transfer through the beam is dominant over the heat transfer to the fluid, which makes the temperature distribution independent of the type of fluid. From the measured electrical resistance  $R$  [ $\Omega$ ], the electrical initial resistance  $R_0$  [ $\Omega$ ] and the temperature rise  $\Delta T$  [ $K$ ] the Temperature Coefficient of Resistance  $\alpha$  [ $K^{-1}$ ] can be obtained using

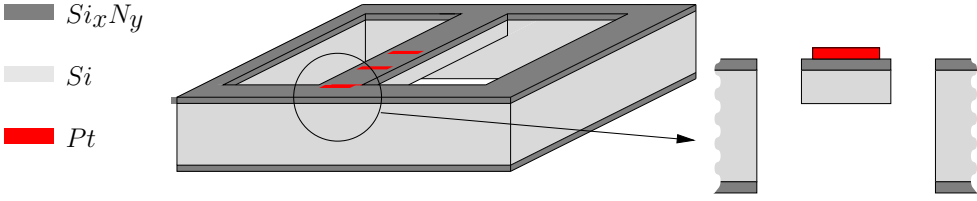


**Figure 6.1:** Schematic drawing of TCR-sensor with a thick beam with distributed sensing



**Figure 6.2:** Schematic drawing of TCR-sensor with a thick beam with distributed sensing

$$R = R_0 (1 + \alpha \Delta T) \quad (6.1)$$

The temperature rise can be calculated from the applied power  $P$  [W] and the thermal resistance of the beam  $R_{therm}$  [K/W].

$$\Delta T = R_{therm} P \quad (6.2)$$

Two versions have been designed for measuring the TCR of the metal heater, see figure 6.2. The first version has a homogeneously heated heater along the beam that is divided in several segments for distributed temperature sensing. The power consumption can be decreased by reducing the heat transport at the edges of the beam to the support: therefore the second version has only a heater at the center together with a few sensors to measure the temperature profile. Due to symmetry the sensors are placed on one side. This makes possible the use of broad current leads of the heater on the other side.

The assumption that the heat transfer through the beam is dominant over the heat transfer through the fluid will be explained by a simple lumped element model. In this model the beam is approximated by a cylindrical heater with radius  $r_1$  in a cylinder of fluid with radius  $r_2$  having the outer surface at zero temperature difference, see figure 6.3. For the thermal conductance of the cylinder equation 3.9 can be used. The quotient of the conductances of the fluid and half of the beam can be expressed by:

$$\frac{G_{fluid}}{G_{beam}} = \frac{2\pi\kappa_f l/2}{\ln(\frac{r_2}{r_1})} / \frac{\kappa_s A}{l/2} = \frac{\kappa_f}{\kappa_s} \frac{l^2}{2\ln(\frac{r_2}{r_1})r_1^2} \quad (6.3)$$

with  $A = \Pi r_1^2$  [m<sup>2</sup>] the cross-sectional area of the beam and  $l$  [m] the length of the beam.

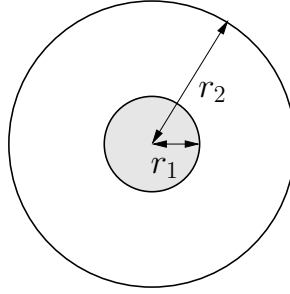


**Figure 6.3:** Simplification of TCR-beam..

The beam is 1 mm long, 150  $\mu\text{m}$  wide and 100  $\mu\text{m}$  high. The cross sections of the real beam and the cylindrical heater are taken equal:  $r_1 = \sqrt{150\mu\text{m} \cdot 100\mu\text{m}/\pi} = 69\mu\text{m}$ . The channel depth is 250  $\mu\text{m}$ : for the outer radius 300  $\mu\text{m}$  will be taken. Due to symmetry half of the length of the beam,  $l/2$ , has been taken. The thermal conductivities  $\kappa_f = 26 \cdot 10^{-3} \text{ W}/(\text{Km})$  for the fluid in case of nitrogen and  $\kappa_s = 100 \text{ W}/(\text{Km})$  for silicon result in a ratio of  $\approx 0.02$ : that means that 2% of the heat will flow through the fluid. For the beam with homogeneous heating this will be even better, because the thermal resistance near the edge to the support is smaller than from the center to the support. Compensation for the heat loss through the fluid is possible by using the temperature distribution, which results in a reduction of the error to well below one percent.

### 6.2.1 Heater along beam

In figure 6.2(a) a schematic drawing of the TCR-sensor with a meandering heater along a thick beam is shown. The heater is divided in five segments by voltage leads. The temperature distribution normalized to the temperature rise at the center can be obtained. As discussed in the chapters 3 and 4 the product of the parameter  $G_f$  and  $R_b$  can be fitted from the normalized temperature distribution. In this manner the assumption that the heat transfer through the beam is dominant over the heat transfer to the fluid can be verified.

In the case  $G_f$  is taken zero equation B.38 will turn into

$$-\frac{1}{R'_b l^2} \frac{\partial^2 T(y_n)}{\partial y_n^2} = P' \quad \text{for} \quad -\frac{1}{2} \leq y_n \leq \frac{1}{2} \quad (6.4)$$

where  $y_n$  is the normalized position along the beam and  $P'$  is the electrical line power in  $[\text{W}/\text{m}]$ . For the boundary conditions  $T(y_n = -0.5) = 0$  and  $T(y_n = 0.5) = 0$  the solution becomes

$$T = \frac{1}{2} P' R'_b l^2 \left( \frac{1}{4} - y_n^2 \right) \quad (6.5)$$

The temperature has to be averaged over each segment between the boundaries  $a$  and  $b$ .

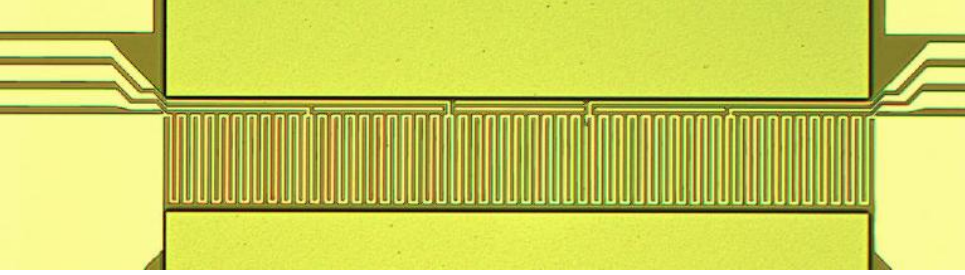


**Figure 6.4:** Photograph of meandering heater divided into five segments

$$\bar{T} = P' R_b' l^2 \left( \frac{1}{8} - \frac{1}{6} \frac{b^3 - a^3}{b - a} \right) \quad (6.6)$$

with  $-0.5 \leq a < 0.5$  and  $-0.5 < b \leq 0.5$ . From the change in the resistance of the sensors the TCR can be obtained using equation 6.1.

In figure 6.4 a photograph of the beam of the TCR-sensor is shown. The voltage contact leads are positioned at one side of the beam to be able to divide the heater in parts with equal length. A DC current will be applied for the measurements.

### 6.2.2 Heater at center

In figure 6.2(b) a schematic drawing of the TCR-sensor with a heater at the center is shown. The TCR sensor consists of a thick silicon beam with in the middle a heater-sensor and at one side sensing resistors for obtaining the temperature distribution, see figure 6.1. A known power  $P$  [W] is applied to the heater at the center. The three sensors will be used to detect linearity. The temperature will have a maximum at the center of the beam and will decrease linearly to the ends of the beam, where it is connected to the bulk. Two resistors are sufficient to measure the TCR or  $\alpha$  [ $K^{-1}$ ], using the temperature drop  $\Delta T$  [K] over the resistors:

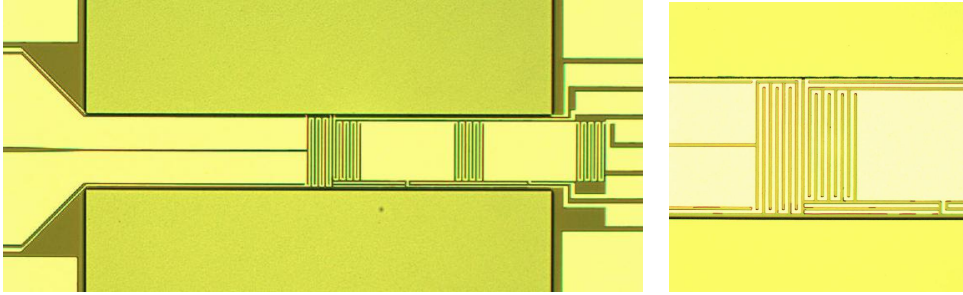
$$\frac{R_2}{R_1} = 1 + \alpha \underbrace{R_b P}_{\Delta T} \quad (6.7)$$

where  $R_1$  [ $\Omega$ ] and  $R_2$  [ $\Omega$ ] are the resistances of two sensing resistors having the same initial resistance,  $P$  [W] is the applied power and  $R_{therm}$  [ $K/W$ ] is the thermal resistance of the silicon beam between two sensing resistors. Probably there will be a small non-linearity, because the heat is applied at the top of the beam. Photographs are shown in figure 6.5. At the left broad current leads, which are used to minimize the Joule heating, and the narrow voltage leads can be seen. The sensors are put in series.

### 6.2.3 TCR obtained from other distributed sensors

In principle it is also possible to determine the TCR from the Pirani or flow sensors from chapters 3 and 4. From the normalized temperature distribution the product  $R_b G_f$  can be fitted using equation 6.8.





(a) Overview of TCR sensor

(b) Magnification of heater at center and closest sensor

**Figure 6.5:** Photograph of TCR-sensor. A heater with two current and two voltage leads at the left. On the right sensors are connected serially.

$$T_n(y_n) = \frac{\Delta T(y_n)}{\Delta T(0)} = \frac{\cosh\left(\frac{1}{2} l \sqrt{R'_b G'_f}\right) - \cosh\left(y_n \cdot l \sqrt{R'_b G'_f}\right)}{\cosh\left(\frac{1}{2} l \sqrt{R'_b G'_f}\right) - 1} \quad (6.8)$$

Using the  $R'_b G'_f$  and knowing the  $R'_b$  the temperature distribution can be obtained from equation 6.9. From the measured change in resistance the TCR can be calculated.

$$\Delta T(y_n) = \frac{P'}{G'_f} \left( 1 - \frac{\cosh\left(y_n \cdot l \sqrt{R'_b G'_f}\right)}{\cosh\left(\frac{1}{2} l \sqrt{R'_b G'_f}\right)} \right) \quad (6.9)$$

Of course, the highest accuracy will be obtained by using the structures that are optimized for TCR measurements.

### 6.3 Kinematic viscosity sensor

The operation of the kinematic viscosity sensor is based on the disturbance of the flow in a channel. This can be done in several ways, e.g. by using a curved channel, by placing an obstacle, by changing the cross section or by splitting the flow. Due to the used technology for processing the latter has been chosen. The kinematic viscosity sensor basically consists of a membrane that splits the fully developed flow in a hexagonal channel, see figure 2.8(a). This influences the heat transfer from the membrane to the fluid. The heat transfer can be measured using several heaters with distributed temperature sensing on the membrane.

The sensor structure is similar to the flow sensor of chapter 3. In the kinematic viscosity sensor the distance between the beams is decreased to a slit and they are interconnected by small beams to form a plate, see figure 6.6. For the flow sensors it

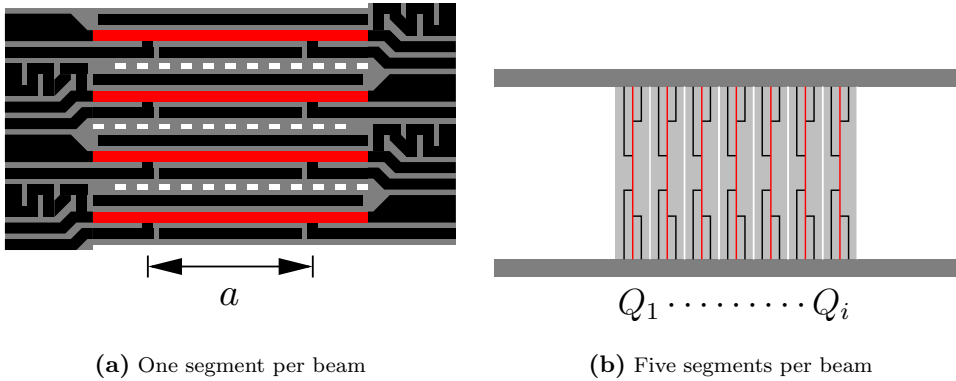


**Figure 6.6:** Schematic drawing of beams of the kinematic viscosity sensor

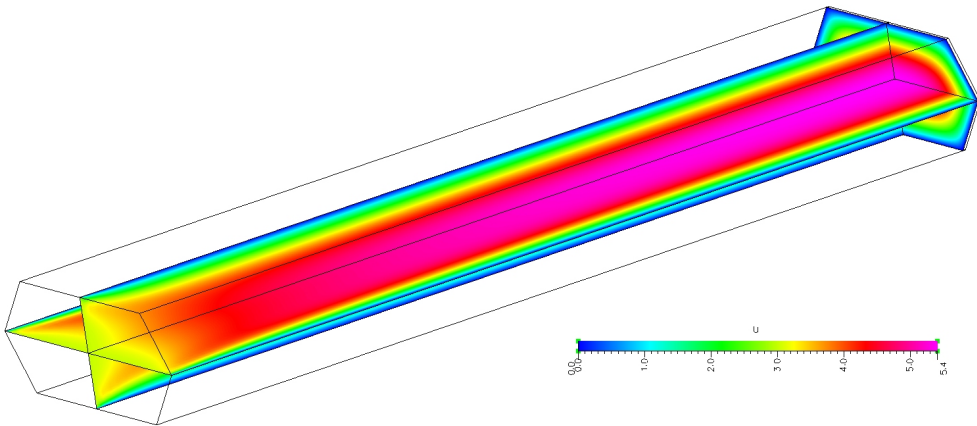


**Figure 6.7:** The flow develops from uniform to fully developed.

was shown that the temperature distribution changes downstream. The temperature of the segment at the center can be kept constant or the current trough all beams can be kept constant.

A FEM simulation of the fluid flow has been carried out, because there are no analytical solutions found. The uniform flow at the entrance develops to a fully developed flow, see figure 6.7. In figure 6.8 the developed flow enters the membrane. Currently a student is including heat transfer.

Two versions have been designed, see figure 6.6: a membrane of 30 beams having one segment per beam and a membrane of 18 beams having five segments per beam. On one side of each beam a reference sensor has been placed. To reduce the forming of destructive hydrogen bubbles the structures have been etched in TMAH in stead of KOH. A photograph of membrane containing beams with distributed sensors is shown in figure 6.9.

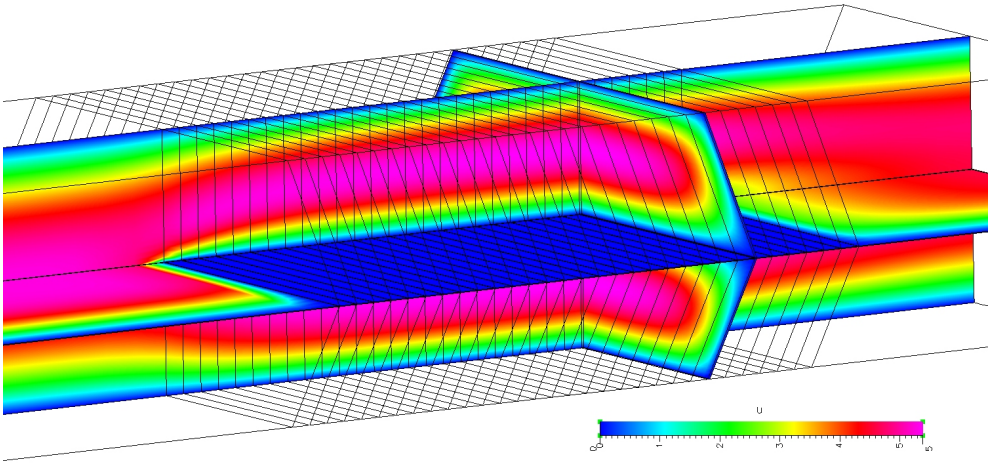


**Figure 6.8:** A cross-section and two longitudinal sections of the flow profile in the channel

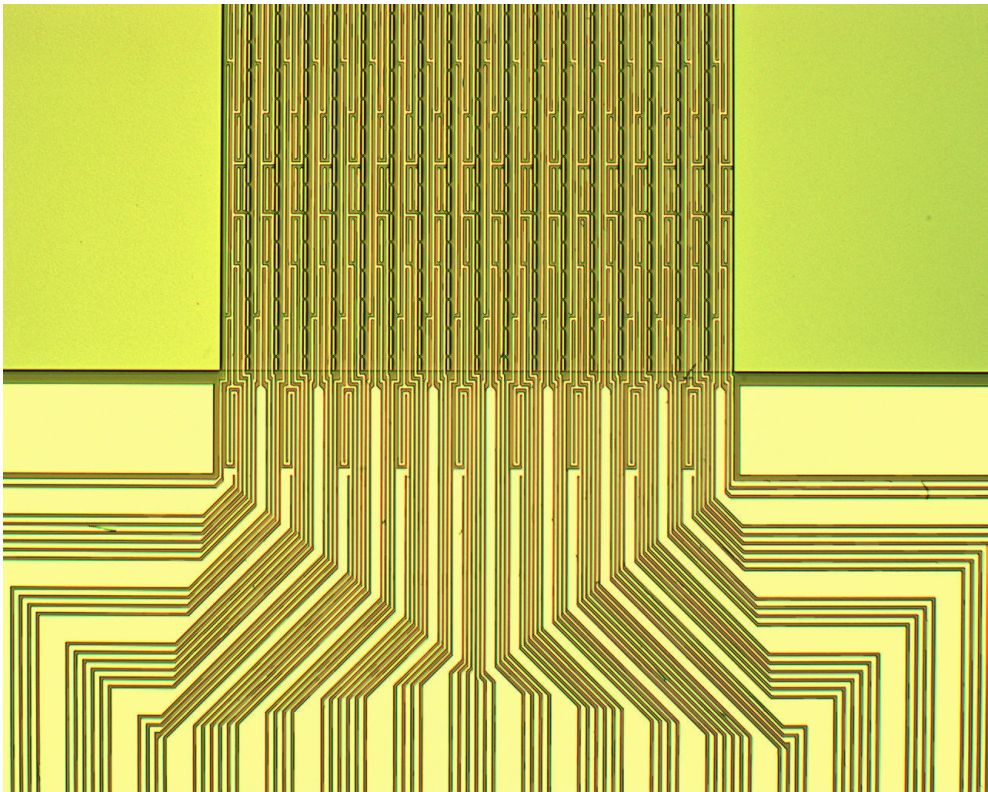


**Figure 6.9:** Photographs of kinematic viscosity sensor

## 6.4 Conclusions

Two designs of a sensor for measuring the TCR have been realized. A FEM model for the kinematic viscosity sensor is currently under construction. Two versions have been realized

## Acknowledgments

Thanks to doctoral student Wilco Verweij for designing, modeling and fabrication of the kinematic viscosity sensor.

# Chapter 7

## Conclusions and outlook

In this thesis a measurement strategy has been proposed, which in principle allows measurement of the parameters thermal conductivity, specific heat, viscosity, density, pressure and flow velocity, using only resistive elements. It was shown that four basic structures are needed. A TCR-sensor was proposed for autocalibration. From these structures only the flow, pressure and thermal conductivity sensors have been realized and characterized. The kinematic viscosity sensor and the TCR sensor have only been designed and realized; so far no measurements have been performed.

### 7.1 Conclusions

#### Chapter 2

A number of structures have been proposed for measuring various fluid and flow parameters. Each structure is optimized for a particular parameter and some have to make use of parameters gained from another sensor. All structures can be realized in the same fabrication process and, therefore, they can be easily combined in a single device. The advantages of beams or membranes with distributed temperature sensing are the elimination of the TCR and the possibility of taking in account the heat loss to the support.

#### Chapter 3

A segmented beam with platinum heater and voltage contact leads has been realized in a micro-machined duct. With this structure the temperature distribution along the beam perpendicular to the flow was measured. The flow profile influences the temperature distribution and theoretically the inverse should also be possible. From the temperature distribution the flow velocity is measured independently of the temperature coefficient of resistance (TCR) of the platinum resistors. In practice, it is not necessary to measure the entire temperature distribution, but it would be sufficient to measure the temperature at two positions. A similar beam positioned at the ends of arms has been realized according the same principle.

## Chapter 4

A Pirani pressure sensor consisting of a heated beam with distributed temperature sensing above a V-grooved heat sink has been realized. Compared to a sensor that measures only the average temperature of the beam, the advantages are the independence from the Temperature Coefficient of Resistance (TCR) of the sensors on the beam and the intrinsic compensation for the heat loss through the beam. The first advantage is due to the normalization of the temperature distribution to the temperature rise at the center, which eliminates the TCR. The second advantage is due to the fact that the model that is used to describe the temperature distribution takes into account the heat transfer through the beam to its support.

It was shown that even though the temperature measurements cannot be performed in a single point but are averaged over a resistor segment, it is still possible to accurately measure the temperature distribution by including the averaging effect in the model. The realized sensor has been tested for pressures ranging from 3.5 to  $10^5$  Pa. The measured transition pressure of  $2.5 \cdot 10^3$  Pa corresponds very well to the expected value.

## Chapter 5

Combined Pirani/bending membrane pressure sensors with various heating/sensing structures have been realized. First measurement results confirm that the sensor is sensitive to both absolute pressure and pressure difference. The former causes a change in the thermal conductance through the narrow gap between the heated membrane and the substrate. The latter causes a bending of the membrane, which results in a changing distance between the membrane and the substrate. A simple lumped element model has been presented that describes the two effects. However, especially in sensor allowing distributed temperature measurements the membrane heating is not uniform. This results in discrepancies between the model and measurement results. A more accurate model should be developed to be able to distinguish between the influence of absolute and differential pressure changes.

As shown in the previous chapters, using the temperature distribution instead of the actual temperature in principle allows cancellation of the influence of the temperature coefficient of resistance. This should be further investigated for the sensors presented in this chapter. Furthermore, it may be sufficient to measure the temperature only in a few strategically chosen positions on the membrane. This should also be further investigated.

## Chapter 6

Two designs of a sensor for measuring the TCR have been realized. A FEM model for the kinematic viscosity sensor is currently under construction. Two versions have been realized

## 7.2 Outlook

The research presented in this thesis is not finished. Several items remain to be done:

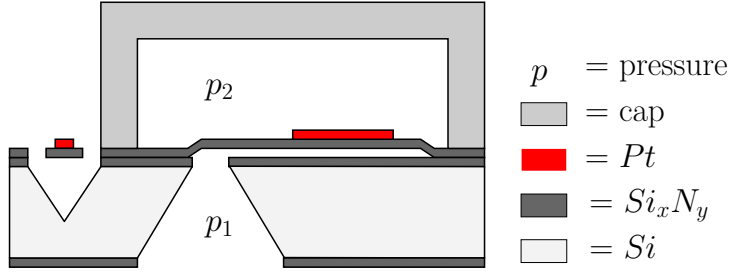


**Figure 7.1:** Schematic drawing of the v-groove pressure sensor on the left and bending membrane pressure sensor on the right, each containing a heater with distributed temperature sensing

- The modeling of the kinematic viscosity sensor has to be improved. Measurement have to be carried out to test the performance of the sensor and compare this to the FEM results.
- Combining a v-groove and bending membrane sensor, as indicated in figure 7.1. The difference in transition pressure can be used to measure the pressure independent of the type of gas [6].
- Dynamic measurements: transient (time of flight) and  $\omega - 3\omega$ , as indicated in appendix C.2
- Measurements on the TCR-sensors

Next, all sensor structures should be combined into a complete measurement system as described in chapter 2





# References

- [1] H.H. Bruun. *Hot-Wire Anemometry*. Oxford University Press, 1994.
- [2] T. Ebefors, E. Klvesten, and G. Stemme. Three dimensional silicon triple-hot-wire anemometer based on polyimide joints. *Proc. MEMS Heidelberg*, pages 93–98, 1998.
- [3] H.E. de Bree. *The Microflow*. Number ISBN 9036515793. 2001.
- [4] Meyer and van Herwaarden. *Thermal sensors*. Number ISBN 0-7503-0220-8. Institute of Physics Publishing, 1994.
- [5] Y. Zhang and K. D. Wise. High-accuracy multi-element silicon barometric pressure sensor. *Digest int. Conf. on Solid-State Sensors and Actuators (Transducers95)*, pages 608–611, 1995.
- [6] Ulrich Bonne and Dave Kubisiak. Burstproof, thermal pressure sensor for gases. *Solid-State Sensor and Actuator Workshop Hilton Head*, pages 78–81, 1994.
- [7] S. Billat et.al. Convection-based micromachined inclinometer using soi technology. *MEMS*, pages 159–162, 2001.
- [8] A. Leung, J.Jones, E. Czyzewska, J. Chen, and M. Pascal. Micromachined accelerometer with no proof mass. *IEDM Washington DC*, pages 899–902, 1997.
- [9] U.A. Dauerstädt, P.M. Sarro, and P.J. French. Temperature dependence and drift of thermal accelerometer. *Sensors and Actuators*, A 66:244–249, 1998.
- [10] T.S.J. Lammerink, N.R. Tas, G.J.M. Krijnen, and M. Elwenspoek. A new class of temperature flow sensors using  $\delta t=0$  as control signal. *MEMS conference, Miyazaki, Japan*, pages 525–530, 2000.
- [11] H.E. de Bree et.al. The microflow. *Sensors and Actuators*, A 54:552–557, 1996.
- [12] M. Elwenspoek and R.J. Wiegerink. *Mechanical microsensors*. Springer Verlag, 2000.
- [13] L.V. King. On the convection of heat from small cylinders in a stream of fluid: determination of the convection constants of small platinum wires with application to hot wire anemometry. *Proc. Roy. Soc. London*, 90 A:563–570, 1914.

- [14] Fukang Jiang. *Silicon-Micromachined flow sensors*. PhD thesis, California Institute of Technology, 1998.
- [15] K. Chen and Y. Wu. Thermal analysis and simulation of the microchannel flow in miniature thermal conductivity detectors. *Sensors and Actuators*, 79:211–218, 2000.
- [16] Y. Huang and H.H. Bau. The effects of forced convection on the power dissipation of constant-temperature thermal conductivity sensors. *Journal of heat transfer*, 119(1):30–36, 1997.
- [17] M. von Pirani. Selbszeigendes vakuummefsinstrument. *Verhandlungen der Deutschen Physikalischen Gesellschaft*, pages 686–694, 1906.
- [18] U.A. Dauerstädt, C.M.A. Ashruf, and P.J. French. A new high temperature pressure sensor based on a thermal read-out principle. *Transducers*, pages 525–530, 1999.
- [19] J.J. van Baar, R.J. Wiegerink, T.S.J. Lammerink, J.W. Berenschot, G.J.M. Krijnen, and M. Elwenspoek. Combined -pirani/bending membrane-pressure sensor. *MEMS Las Vegas*, 2002.
- [20] H. Ohji, N. Yutani, M. Taruya, A. Koshimizu, S. Kodama, and K. Tsutsumi. A new pressure sensor measured by heat transfer. *IEEE*, 67.3, 2002.
- [21] J.J. van Baar, R.J. Wiegerink, T.S.J. Lammerink, G.J.M. Krijnen, and M. Elwenspoek. Micro-machined structures for thermal measurements of fluid and flow parameters. *J. of MicroMech. and MicroEng*, volume 11, issue 4 (July):311–318, 2001.
- [22] W. Zheng, Z. Yinping, L. Xingang, and G. Xinshi. Long/short hot-probe method for determining thermophysical properties. *Measurement Science and Technology*, 5(8):964–968, 1994.
- [23] J. van Kuijk. Multi-parameter detection in fluid flows. *Sensors and Actuators*, A 46-47:369–372, 1995.
- [24] W Zobel, J Hetfleisch, and J Fricke. Measurement of thermal diffusivity with a guarded-hot-plate device using a dynamic method. *Measurement Science and Technology*, 5(7):842–846, 1994.
- [25] O. Paul and Baltes. Vacuum gauging with complementary metal-oxide semiconductor microsensors. *J. Vac. Sci. Technol.*, A 13(3):503–508, 1995.
- [26] Ping Kuo Weng and Jin-Shown Shie. Micro-pirani vacuum gauge. *Rev. Sci. Instrum.* 65 (2), pages 492–499, 1994.
- [27] K.L. Chopra. *Thin film phenomena*. McGraw-Hill, 1969.
- [28] K. Tsutsumi, A. Yamashita, and H. Ohji. The experimental study of high temperature thin films for thermal sensors. *IEEE*, 31.1, 2002.

- [29] David K. Lambert and Sterling Heights. Thermal diffusion fluid flow sensor, 1986. patent no. 4,576,050.
- [30] Sultan Michel F and Charles R. Harrington. Differential ac anemometer, 1993. patent no. 5,263,380.
- [31] H.S. Carslaw and J.C. Jaeger. *Conduction of heats in solids*. Oxford University Press, 1959.
- [32] Frank M. White. *Fluid Mechanics*. McGraw-Hill, 1994.
- [33] M. von Smoluchowski. Zur theorie der warmteleitung in verdunnten gasen und der dabei auftretenden druckkrafte. *Annalen der Physik*, 35:983–1004, 1911.
- [34] Frank P. Incropera and David P. DeWitt. *Fundamentals of Heat and Mass Transfer*. John Wiley, 1996.
- [35] Mattias Vangbo and Ylva Bäcklund. Terracing of (100) si with one mask and one etching step using misaligned v-grooves. *Journal of Micromechanics and Microengineering*, 6(1):39–41, 1996.
- [36] Richard. J. Goldstein. *Fluid Mechanics Measurements, second edition*. Taylor & Francis, 1996.
- [37] N.T. Nguyen and R. Kiehnscherf. Low-cost silicon sensors for mass flow measurement of liquids and gases. *Sensors and Actuators*, 49 A:17–20, 1995.
- [38] A.F.P. van Putten and S. Middelhoek. Integrated an integrated silicon anemometer. *Electronics Letters*, 10 (21):425–426, 1974.
- [39] J.F. O’Hanlon. *A Users guide to Vacuum Technology*. Wiley, 1980.
- [40] J.H. Leck. *Pressure Measurement in Vacuum Systems*. Chapman and Hall, 1964.
- [41] L. Carpenter. Vacuum technology, an introduction. *American Elsevier*, pages 49–55, 1970.
- [42] A.W. van Herwaarden and P.M. Sarro. Performance of integrated thermopile vacuum sensors. *J. Phys. E: Sci. Instrum.*, 21:1162–1167, 1988.
- [43] A.W. van Herwaarden. *Thermal vacuum sensors based on integrated silicon thermopiles*. PhD thesis, Delft University of Technology, 1987.
- [44] E.H. Klaassen and G.T.A. Kovacs. Integrated thermal conductivity vacuum sensor. *Solid State Sensor and Actuator Workshop*, pages 249–252, 1996.
- [45] A.M. Robinson, P. Haswell, and R.P.W. Lawson. A thermal conductivity microstructural pressure sensor fabricated in standard complementary metal-oxide semiconductor. *Rev. Sci. Instrum.*, 63(3):2026–2029, 1992.
- [46] R. Puers, S. Reyntjens, and D. De Bruyker. The nanopirani an extremely miniaturized pressure sensor fabricated by focused ion beam rapid prototyping. *Sensors and Actuators A*, pages 97–98, 2002.

- [47] Nicholas R. Swart and Arokia Nathan. An integrated cmos polysilicon coil-based micro-pirani gauge with high heat transfer efficiency. *IEEE*, pages 135–138, 1994.
- [48] A.W. van Herwaarden and P.M. Sarro. Double-beam integrated thermal vacuum sensor. *J. Vac. Sci. Technol.*, A 5(4):2454–2457, 1987.
- [49] S.D. James, R.G. Johnson, and R.E. Higashi. A broad range absolute pressure microsensor. *IEEE Solid State Sensor and Actuator Workshop*, pages 107–108, 1988.
- [50] C.H. Mastrangelo and R.S. Muller. Fabrication and performance of a fully integrated -pirani pressure gauge with digital readout. *Proceedings of Transducers 91*, pages 245–248, 1991.
- [51] C.H. Mastrangelo and R.S. Muller. Microfabricated thermal absolute-pressure sensor with on-chip digital front-end processor. *IEEE J. Solid-State Circuits*, 26:1998–2007, 1991.
- [52] J.S. Shie, B.C.S. Chou, and Y.-M. Chen. High performance pirani vacuum gauge. *Vac. Sci. Technol. A*, 13(6):2972–2979, 1995.
- [53] B.C.S. Chou and J.S. Shie. An innovative pirani pressure sensor. *Transducers 97*, pages 1465–1468, 1997.
- [54] B.C.S. Chou, C.N. Chen, and J.S. Shie. Fabrication and study of a shallow-gap pirani vacuum sensor with a linearly measurable atmospheric pressure range. *Sensors and Materials*, 11(6):383–392, 1999.
- [55] Bruce C.S. Chou, Chung-Nan Chen, and Jin-Shown Shie. Micromachining on 111-oriented silicon. *Sensors and Actuators 75*, pages 271–277, 1999.
- [56] W.J. Alvesteffer, D.C Jacobs, and D.H. Baker. Miniaturized thin film thermal vacuum sensor. *J. Vac. Sci. Technol.*, A 13(6):2980–2985, 1995.
- [57] Frederick Reif. *Fundamentals of statistical and thermal physics*. McGraw-Hill, 1965.
- [58] Jiri Vlach and Kishore Singhal. *Computer methods for circuit analysis and design*. van nostrand reinhold, 1983.
- [59] C.H. Mastrangelo, Y.C. Tai, and R.S. Muller. Thermophysical properties of low-residual stress, silicon-rich, lpcvd silicon nitride films. *Transducers 89*, pages 856–860, 1989.
- [60] J.W. Berenschot, N.R. Tas, T.S.J. Lammerink, M. Elwenspoek, and A. van den Berg. Advanced sacrificial poli-si technology for fluidic systems. *Transducers '01 Munich Germany*, 2001.
- [61] Xing Yang, Yu-Chong Tai, and Chih-Ming Ho. Micro bellow actuators. *Transducers*, pages 45–48, 1997.
- [62] O. Paul and H. Baltes. Novel fully cmos-compatible vacuum sensor. *Sensors and Actuators A*, pages 143–146, 1995.

# Appendix A

## Process scheme

The process scheme of a mass flow and fluid velocity sensor, a thermal conductivity sensor and a structure for built-in auto-calibration of the TCR will be discussed.

The device contains three types of sensors, which are made within the same processes: a flow sensor in a hexagonal duct, a beam to measure the temperature coefficient resistance and a thermal conductivity sensor. The channel is formed by two wafers: one for the cap with in- and outlets and the other with the structures. The TCR-sensor and thermal conductivity sensor are placed at the end of the duct in a dead volume for reducing the influence of forced convection. Because of the large aspect ratio of the channel a wagon wheel is used to obtain the crystal orientation. Besides this mask six other masks are needed: two for the cap and four for the wafer with metal structures.  $Si_xN_y$  and polysilicon layers have to be deposited and metal has to be sputtered. Used etchants are Reactive Ion Etching for patterning the polysilicon and  $Si_xN_y$ , HF for removing  $Si_xN_y$  and KOH for bulk etching. The wafers will be glued on top of each other and the devices will be broken out of the wafer. The chips will be glued and wire-bonded on Printed Circuit Board.

### A.1 General

A TCR-sensor, thermal conductivity sensor, flow sensor and channel with in- and outlets will be made within the same processes. An impression of the device is given in figure A.1. It contains two compartments: a dead volume and a flow part. The TCR-sensor and thermal conductivity sensor are placed at the end of the duct in a dead volume for reducing the influence of forced convection. Only diffusion of the fluid will take place. A "refreshment burst" can be given to accelerate it.

The channel is formed by two wafers: one for the cap with in- and outlets and the other containing the structures. After alignment the wafers will be glued on each other and the samples will be broken out of the wafer.

The geometry has been optimized for their function. So the metal resistors on the sensors are deposited simultaneously and will operate under similar circumstances: same gas and pressure.

The length of the hexagonal duct is 40 mm, the width is 1 mm and its height is 0.5 mm. The beams over the channel are placed about on three quarters from the

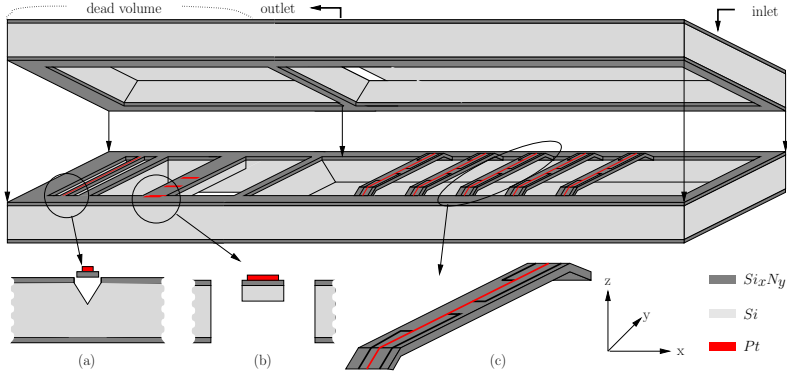


**Figure A.1:** Thermal conductivity, TCR and mass flow sensors

**Table A.1:** Three types of beams

number segments	width [ $\mu\text{m}$ ]	length [ $\mu\text{m}$ ]	center to center spacing [ $\mu\text{m}$ ]
25	100	1000	200
9	40	1000	70
9	40	750	70

entrance, because in this part the flow has to develop fully. Three variations of beam length and width are available, see table A.1. Increasing the number of segments on a beam, increases the spatial resolution and decreases the value of the measured voltages. A compromise has to be chosen between the spatial resolution and the required power

A polysilicon layer of minimal 50 nm for under-etching the beams has to be deposited. This results in a little step, but will be smoothed due to the etching of the resist at the edges.

The thermal conductivity sensor is a narrow beam above a V-groove with little depth in a dead volume. Taking a beam of 25  $\mu\text{m}$  width with five resistor segments and on both sides a 2.5  $\mu\text{m}$  space for etching and preventing a thermal shortcut. In this case the KOH etching stops at a maximum depth of 21  $\mu\text{m}$ .

Because of the large aspect ratio of beam length to the channel width a good alignment to the crystal orientation is necessary to minimize the underetch. A 150 nm  $\text{Si}_x\text{N}_y$  layer is deposited and patterned with Vangbo mask for obtaining the crystal orientation. This  $\text{Si}_x\text{N}_y$  layer will be used as etch mask for forming the channel. For the other wafer this layer has to be removed using HF.

Four types of structures are realized, see table A.1: a variation in width of beams, the spacing and the inclusion of a TCR-sensor and TCD and width of channel.

Using  $(w_h + 2ma_h) + (w_l + s_l) \left( \frac{\text{number of segments} - 1}{2} \right)$  the width of the beam can be calculated with  $w_h$  the width of the heater,  $ma_h$  the misalignment of the heater,  $w_l$  width of the voltage leads and  $s_l$  the spacing of the leads.

The thickness of the TCR-beam is determined by the thickness of the wafer minus the channel depth. The most optimal shape should have a large volume to area ratio.

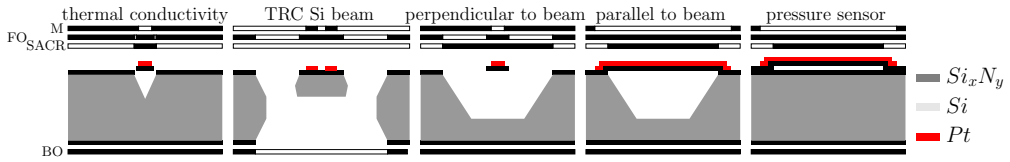


**Figure A.2:** Cross section of some parts of structure and needed masks. The pressure sensor has been realized in another run.

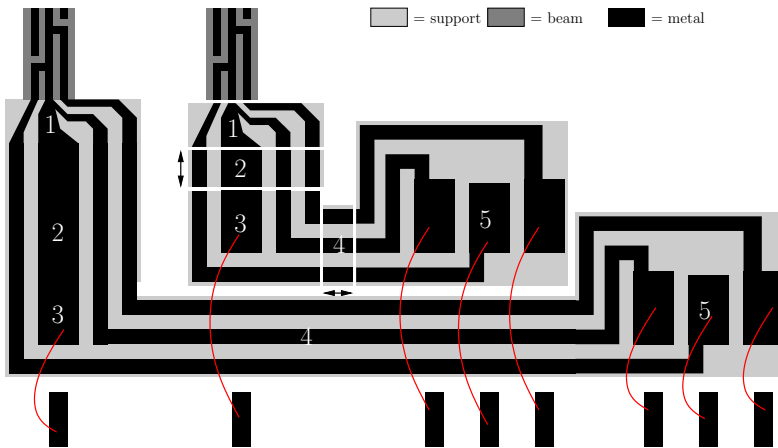


**Figure A.3:** Simplification of part of mask/structure

## A.2 Masks

In figure A.3 a simplified drawing of the modular drawing can be seen. Modules 2 and 4 have got a rubber length<sup>1</sup> to be able to draw the mask easily. In table A.2 the function and some other parameters are given. Remark: the top and bottom wafers are with respect to each other mirrored.

<sup>1</sup>a rubber length has a natural length and a degree of elasticity

**Table A.2:** Specifications of the masks

mask name	inside white/black	mirrored	function
poly	black	æ∂∂	sacrificial layer
metal	white	æ∂∂	lift-off
top	black	æ∂∂	front opening
bottom	black	no	bottom opening
top cap	black	no	top opening cap
bottom cap	black	æ∂∂	bottom opening cap

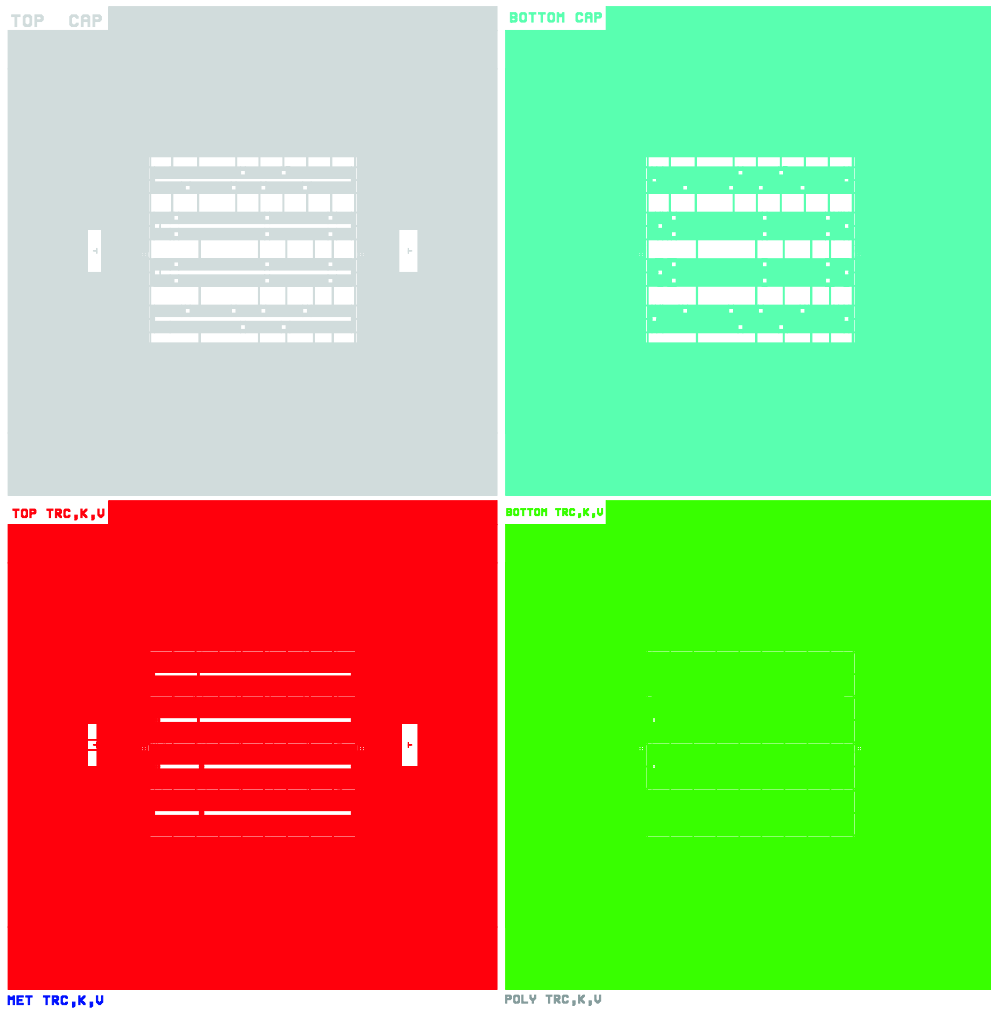
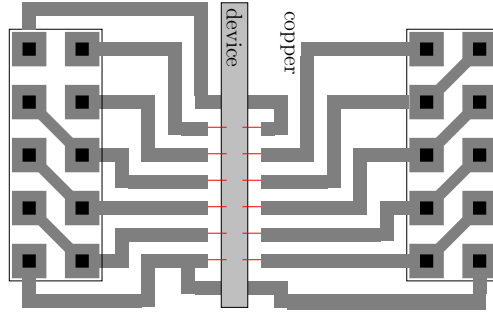


Figure A.4: Overview of the masks





**Figure A.5:** Simplification of part of PCB with holes for connectors

### A.3 Connection to the macro world

From the bond pads on the chip aluminium wire bonds, with a diameter of  $20\ \mu\text{m}$ , are connected to the copper leads on the PCB, see figure A.5. On this PCB headers are soldered, which are attached to the block connectors of the flat cables.

The spacing of the copper leads is  $400\ \mu\text{m}$  ( $200\ \mu\text{m}$  copper +  $200\ \mu\text{m}$  empty space). For 4 cm this gives a maximum of 100 copper leads for one side of the channel.

### A.4 Fabrication

In figure A.6 the structures are plotted next to each other. A thin  $\text{Si}_x\text{N}_y$  layer has first deposited and etched for obtaining a good alignment to the crystal orientation, because of the large aspect ratio of beam length to channel width. The next steps are selectively stripping the  $\text{Si}_x\text{N}_y$  and the deposition of polysilicon for etching the beams free and the deposition of  $\text{Si}_x\text{N}_y$ . After sputtering platinum KOH etching. KOH etching stops at a maximum depth of  $21\ \mu\text{m}$  for the thermal conductivity sensor. The channel depth is about  $250\ \mu\text{m}$ . The TCR-beam is etched from both sides. The cap will be glued on the bottom wafer and the devices will be broken out of the wafer. Afterwards the structure will be glued on printed circuit board (PCB).

### A.5 Wafer

- 3 inch
- $n$  or  $p$  type (only used as carrier, conductivity not important)
- $\langle 100 \rangle$  oriented
- single sided polished
- measured thickness about  $380\ \mu\text{m}$

### A.6 Process outline

The parameters used for each processing step are given in the long table.

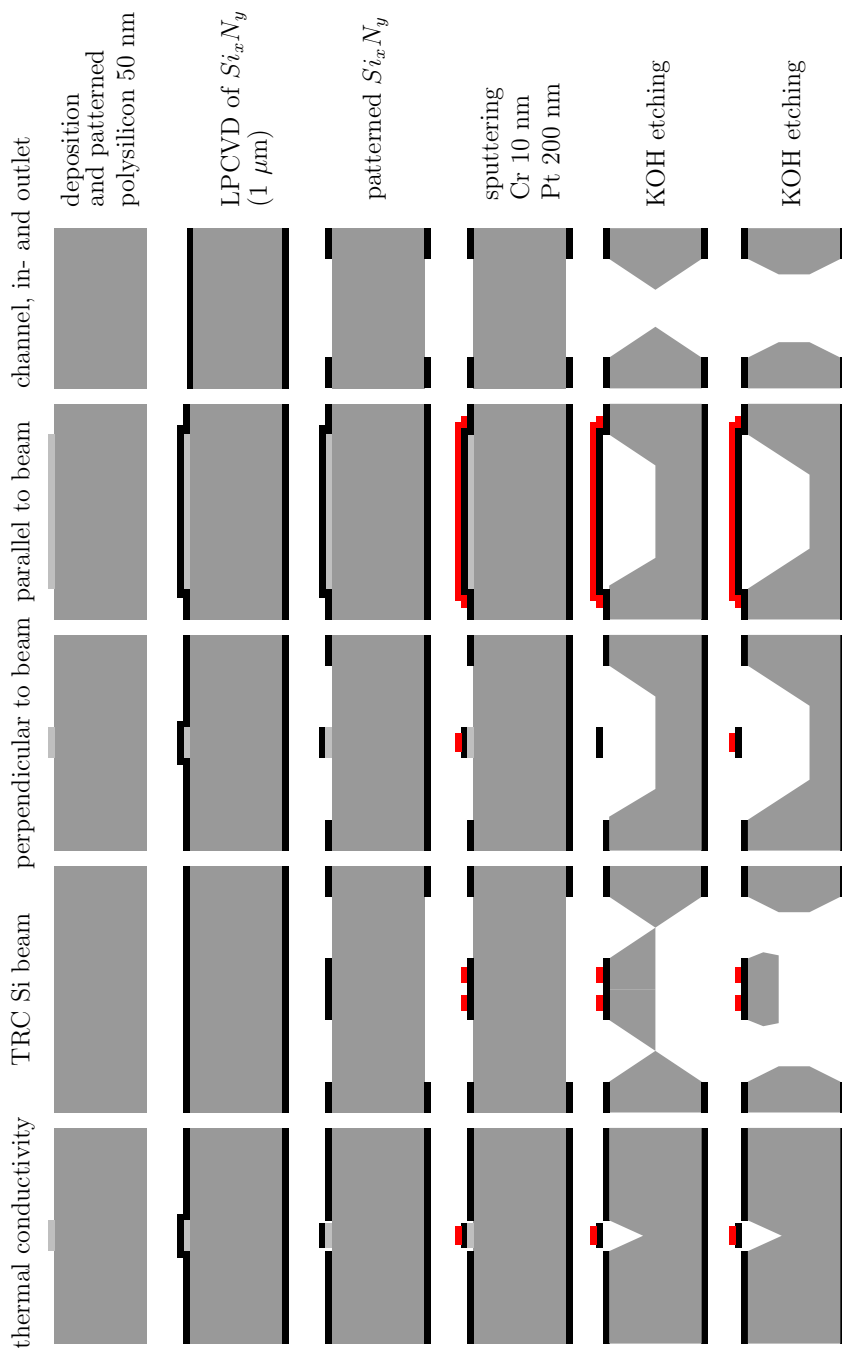


Figure A.6: Overview of the process steps of the wafers

Project : Distributed sensing  
 Author : John van Baar

File : procTCRkmf.sxw

Page : 1  
 Date: 10/30/02

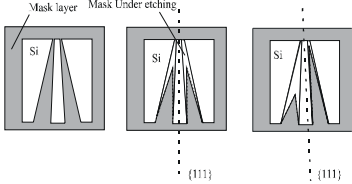
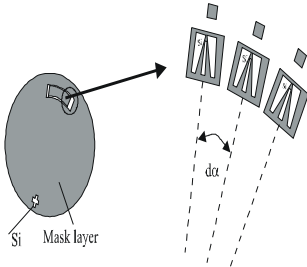
Process scheme of structure for measuring  $TCR$ ,  $\kappa$ ,  $\rho c$  and  $\nu$

Step	Process	Parameters	Remarks
01b	<a href="#">Cleaning introduction</a>	<b>Wet Bench SC</b> -HNO <sub>3</sub> (100%) Selectipur:MERCK 100453 -HNO <sub>3</sub> (69%) VLSI: MERCK 116445  -HNO <sub>3</sub> (100%) (II), 5min -quick dump rinse, DI, <0.1μS -HNO <sub>3</sub> (69%) (95°C), 15min -quick dump rinse, DI, <0.1μS -spin drying	<i>Removal of light organic particles and metals</i>
02b	<a href="#">LPCVD SiRN-S&amp;A (standard low stress)</a>	-Tempress LPCVD Furnace -Tube 6 S&A -program Nxx -SiH <sub>2</sub> Cl <sub>2</sub> flow 70sccm -NH <sub>3</sub> flow 18sccm -temperature 850°C -pressure 200mTorr -deposition rate 8.3nm/min (3" wafers) -deposition rate 7.3 nm/min (4" wafers) -Nf :2.14 -stress : 10,6*10-10 dyne/cm <sup>2</sup> -uniformity (wafer)xxxxx % -uniformity (batch)xxxxx%	<b>Cleaning required</b> 150 nm
03b	<a href="#">Lithography-Olin907-17SSP</a>	<b>S&amp;A Litho Bench/ElectronicVisions AI-6</b> -dehydration bake/priming scheme: Hotplate 140°C, 60 sec + gas priming of HMDS ( <i>Gamma 60</i> ) -resist: Olin 907-17, 4000rpm, 20sec -prebake: hotplate 95°C, 90sec -Exposure parameters 4" or 5"      xxx      20μm 4. or 6 mm    xxx      30μm 3" / 4"      top/bot    100/10N 0.4/0.6mm    xxx      xxs (5sec) 2 -after exposure bake: 120°C, 60sec -development: OPD 4262, 45-60s -quick dump rinse, DI, <0.1μS -spin drying -visual microscopic inspection -postbake: hotplate 120°C, 30min	

Project : Distributed sensing  
 Author : John van Baar

File : procTCRkmf.sxw

Page : 2  
 Date: 10/30/02

04b	<a href="#">Plasma etching of SiN</a>	<p>-Elektrotech PF 310/340 (Etske)          -dirty chamber          -styros electrode          -electrode temp.: 10°C          -CHF<sub>3</sub> flow 25sccm          -O<sub>2</sub> flow 5sccm          -pressure 10mTorr          -power 75W          -etchrate SiRN 60-90nm/min          -etchrate Olin resist 95nm/min          -profile: slightly tapered for PR          -profile: directional for metal mask</p>	<b>Reservation necessary</b> time=3 minutes
05b	<a href="#">Stripping of Olin 907 by oxygen plasma</a>	<p><b>Nanotech Plasmaprep 100</b>          -O<sub>2</sub> flow 55sccm          -power 120W          -electrode temperature 150°C          -pressure 2.00mbar          -time 20min          -visual microscopic inspection</p>	
06b	<a href="#">Etching Si KOH-crystal-alignment to {111}</a>	<p><b>Procedure Vangbo</b>          Finding {111} orientation with etch structures <a href="#">[Vangbo96]</a></p>  <p>-Left: to find {111} planes,          -Center: perfect alignment          -Right: misaligned etch structure</p> <p>The etch mask structure used in <a href="#">[Vangbo96]</a> can be seen in fig above. In the center fig. can be seen how symmetric under etch profiles arise when the etch structure is aligned parallel to an {111} plane. When the aligning is not perfect the under-etching is no longer symmetric (fig. right). In fig. below it can be seen how the structures can be used in the fabrication process.</p> 	

Project : Distributed sensing  
 Author : John van Baar

File : procTCRkmf.sxw

Page : 3  
 Date: 10/30/02

		<p>The etch structures, each with a slightly different orientation, are placed on a circle, where the origin of the circle is the cross shown on the wafer drawn left in the figure. This cross is one alignment mark for following lithographic steps. The second alignment mark is the mark standing above the etch structure that shows a symmetric under etch profile after KOH etch (and is thus aligned to the (111) orientation).</p>	
07b	<a href="#">Etching Si KOH-1</a>	<p><b>-Wet Bench KOH-prep</b>          -prepare 25 gew% KOH p.a. (500gr KOH-1500ml DI)          -etch temp.:75°C          -stirrer</p> <p>-SiO<sub>2</sub> (thermisch): 180 nm/hr          -SiRN: &lt; 1 nm/min          -etchrate &lt;100&gt;: 1 µm/min          -etchrate &lt;111&gt;: 12.5 nm/min          -quick dump rinse, DI, &lt;0.1µS          -spin drying</p>	Time=11'30"
08b	<a href="#">Cleaning RCA-2 (HCL/H2O2/H2O)</a>	<p><b>Wet Bench RCA</b>          -HCL (32%) Selectipur: MERCK 100322          -H2O2 (31%) VLSI: MERCK 108552</p> <p>-add HCLto H2O          -HCL:H2O: H2O2 (1:6:1) vol%          -add H2O2 when mixture is 70          -temperature 75-80 °C          -time 10-15 min          -quick dump rinse, DI, &lt;0.1µS          -spin drying</p>	<i>Dissolves alkali ions, and hydroxides of Al, Fe, Mg and Cu, Au</i>
09b	<a href="#">Etching HF (50%) LPCVD SiN</a>	<p><b>-Wet Bench HF/BHF</b>          -Standard S&amp;A HF 50%          -IC-compatible solution          -etchrate 5nm/min          -temperature 20°C          -quick dump rinse, DI, &lt;0.1µS          -spin drying</p>	Ready if surface hydrofobe

Project : Distributed sensing  
 Author : John van Baar

File : procTCRkmf.sxw

Page : 4  
 Date: 10/30/02

10b	<a href="#">Cleaning online</a>	<b>Wet Bench SC</b> -HNO3 (100%) Selectipur:MERCK 100453 -HNO3 (69%) VLSI: MERCK 116445  -HNO3 (100%) (I), 5min -HNO3 (100%) (II), 5min -quick dump rinse, DI, <0.1µS -HNO3 (69%) (95°C), 15min -quick dump rinse, DI, <0.1µS -spin drying	<i>Removal of light organic particles and metals</i>												
11b	<a href="#">LPCVD Poly Si-590-S&amp;A</a>	Tempress LPCVD Furnace -program N5 -SiH <sub>4</sub> flow: 50sccm -temperature: 590°C -pressure: 200mTorr -deposition rate: 6.4 nm/min	<b><i>Cleaning required, check deposition rate</i></b> 16 minutes add dummies for determining thickness												
12b	<a href="#">Lithography-Olin907-17SSP</a>	<b>S&amp;A Litho Bench/ElectronicVisions Al-6</b> -dehydration bake/priming scheme: Hotplate 140°C, 60 sec + gas priming of HMDS ( <i>Gamma 60</i> ) -resist: Olin 907-17, 4000rpm, 20sec -prebake: hotplate 95°C, 90sec -Exposure parameters <table border="0" data-bbox="538 1066 911 1190"> <tr> <td>4"or5"</td> <td>xxx</td> <td>20µm</td> </tr> <tr> <td>4.or6 mm</td> <td>xxx</td> <td>30µm</td> </tr> <tr> <td>3"7/4"</td> <td>top/bot</td> <td>100/10N</td> </tr> <tr> <td>0.4/0.6mm</td> <td>xxx</td> <td>xxs</td> </tr> </table> (5sec) 2 -after exposure bake: 120°C, 60sec -development: OPD 4262, 45-60s -quick dump rinse, DI, <0.1µS -spin drying -visual microscopic inspection -postbake: hotplate 120°C, 30min	4"or5"	xxx	20µm	4.or6 mm	xxx	30µm	3"7/4"	top/bot	100/10N	0.4/0.6mm	xxx	xxs	front side mask: "poly TCR, k, v"
4"or5"	xxx	20µm													
4.or6 mm	xxx	30µm													
3"7/4"	top/bot	100/10N													
0.4/0.6mm	xxx	xxs													
13b	<a href="#">Plasma etching of silicon shallow</a>	-Elektrotech PF 310/340 (Etske) -Clean chamber -styros electrode +4" silicon wafer -Showerhead -electrode temp.: 10°C -SF6 flow 30 sccm -CHF <sub>3</sub> flow 25sccm -O <sub>2</sub> flow 20sccm -pressure 75mTorr -power 40 W etch rate =70 nm/min	<b><i>Reservation necessary</i></b> frontside AND backside <i>No showerhead</i> Tape three little Si-parts on 4" wafer to prevent drifting of the wafer												

Project : Distributed sensing  
 Author : John van Baar

File : procTCRkmf.sxw

Page : 5  
 Date: 10/30/02

14b	<a href="#">Stripping of Olin 907 by oxygen plasma</a>	<b>Nanotech Plasmaprep 100</b> -O <sub>2</sub> flow 55sccm -power 120W -electrode temperature 150°C -pressure 2.00mbar -time 20min -visual microscopic inspection	
15b	<a href="#">Cleaning online</a>	<b>Wet Bench SC</b> -HNO <sub>3</sub> (100%) Selectipur:MERCK 100453 -HNO <sub>3</sub> (69%) VLSI: MERCK 116445  -HNO <sub>3</sub> (100%) (I), 5min -HNO <sub>3</sub> (100%) (II), 5min -quick dump rinse, DI, <0.1μS -HNO <sub>3</sub> (69%) (95°C), 15min -quick dump rinse, DI, <0.1μS -spin drying	<i>Removal of light organic particles and metals</i>
16b	<a href="#">LPCVD SiRN-S&amp;A (standard low stress)</a>	-Tempress LPCVD Furnace -Tube 6 S&A -program Nxx -SiH <sub>2</sub> Cl <sub>2</sub> flow 70sccm -NH <sub>3</sub> flow 18sccm -temperature 850°C -pressure 200mTorr -deposition rate 8.3nm/min (3" wafers) -deposition rate 7.3 nm/min (4" wafers) -Nf :2.14 -stress : 10,6*10 <sup>-10</sup> dyne/cm <sup>2</sup> -uniformity (wafer)xxxxx % -uniformity (batch)xxxxx%	<b>Cleaning required</b> Time=120 minutes
17b	<a href="#">Lithography-Olin907-17SSP</a>	<b>S&amp;A Litho Bench/ElectronicVisions AI-6</b> -dehydration bake/priming scheme: Hotplate 140°C, 60 sec + gas priming of HMDS ( <i>Gamma 60</i> ) -resist: Olin 907-17, 4000rpm, 20sec -prebake: hotplate 95°C, 90sec -Exposure parameters 4"or5"      xxx      20μm 4.or6 mm    xxx      30μm 3"7/4"      top/bot    100/10N 0.4/0.6mm   xxx      xxs (5sec) 2 -after exposure bake: 120°C, 60sec -development: OPD 4262, 45-60s -quick dump rinse, DI, <0.1μS -spin drying -visual microscopic inspection -postbake: hotplate 120°C, 30min	front side mask: "top TCR,k,v"

Project : Distributed sensing  
 Author : John van Baar

File : procTCRkmf.sxw

Page : 6  
 Date: 10/30/02

18b	<a href="#">Plasma etching of SiN</a>	<ul style="list-style-type: none"> <li>-Elektrotech PF 310/340 (Etske)</li> <li>-dirty chamber</li> <li>-styros electrode</li> <li>-electrode temp.: 10°C</li> <li>-CHF<sub>3</sub> flow 25sccm</li> <li>-O<sub>2</sub> flow 5sccm</li> <li>-pressure 10mTorr</li> <li>-power 75W</li> <li>-etchrate SiRN 60-90nm/min</li> <li>-etchrate Olin resist 95nm/min</li> <li>-profile: slightly tapered for PR</li> <li>-profile: directional for metal mask</li> </ul>	<b>Reservation necessary</b> time=15 minutes
19b	<a href="#">Stripping of Olin 907 by oxygen plasma</a>	<p><b>Nanotech Plasmaprep 100</b></p> <ul style="list-style-type: none"> <li>-O<sub>2</sub> flow 55sccm</li> <li>-power 120W</li> <li>-electrode temperature 150°C</li> <li>-pressure 2.00mbar</li> <li>-time 20min</li> <li>-visual microscopic inspection</li> </ul>	
20b	<a href="#">Cleaning online</a>	<p><b>Wet Bench SC</b></p> <ul style="list-style-type: none"> <li>-HNO<sub>3</sub> (100%) Selectipur:MERCK 100453</li> <li>-HNO<sub>3</sub> (69%) VLSI: MERCK 116445</li> <li>-HNO<sub>3</sub> (100%) (I), 5min</li> <li>-HNO<sub>3</sub> (100%) (II), 5min</li> <li>-quick dump rinse, DI, &lt;0.1μS</li> <li>-HNO<sub>3</sub> (69%) (95°C), 15min</li> <li>-quick dump rinse, DI, &lt;0.1μS</li> <li>-spin drying</li> </ul>	<i>Removal of light organic particles and metals</i>
21b	<a href="#">Lithography-Olin907-17SSP</a>	<p><b>S&amp;A Litho</b></p> <p><b>Bench/ElectronicVisions Al-6</b></p> <ul style="list-style-type: none"> <li>-dehydration bake/priming scheme:</li> <li>Hotplate 140°C, 60 sec + gas priming of HMDS (<i>Gamma 60</i>)</li> <li>-resist: Olin 907-17, 4000rpm, 20sec</li> <li>-prebake: hotplate 95°C, 90sec</li> <li>-Exposure parameters</li> <li>4"or5"      xxx      20μm</li> <li>4.or6 mm    xxx      30μm</li> <li>3"7/4"      top/bot    100/10N</li> <li>0.4/0.6mm   xxx      xxs</li> <li>(5sec)</li> <li>2</li> <li>-after exposure bake: 120°C, 60sec</li> <li>-development: OPD 4262, 45-60s</li> <li>-quick dump rinse, DI, &lt;0.1μS</li> <li>-spin drying</li> <li>-visual microscopic inspection</li> <li>-postbake: hotplate 120°C, 30min</li> </ul>	back side mask: "bottom TCR,k,v"



Project : Distributed sensing  
 Author : John van Baar

File : procTCRkmf.sxw

Page : 7  
 Date: 10/30/02

22b	<a href="#">Plasma etching of SiN</a>	<ul style="list-style-type: none"> <li>-Elektrotech PF 310/340 (Etske)</li> <li>-dirty chamber</li> <li>-styros electrode</li> <li>-electrode temp.: 10°C</li> <li>-CHF<sub>3</sub> flow 25sccm</li> <li>-O<sub>2</sub> flow 5sccm</li> <li>-pressure 10mTorr</li> <li>-power 75W</li> <li>-etchrate SiRN 60-90nm/min</li> <li>-etchrate Olin resist 95nm/min</li> <li>-profile: slightly tapered for PR</li> <li>-profile: directional for metal mask</li> </ul>	<b>Reservation necessary</b> time = 15 minutes
23b	<a href="#">Stripping of Olin 907 by oxygen plasma</a>	<p><b>Nanotech Plasmaprep 100</b></p> <ul style="list-style-type: none"> <li>-O<sub>2</sub> flow 55sccm</li> <li>-power 120W</li> <li>-electrode temperature 150°C</li> <li>-pressure 2.00mbar</li> <li>-time 20min</li> <li>-visual microscopic inspection</li> </ul>	
24b	<a href="#">Cleaning online</a>	<p><b>Wet Bench SC</b></p> <ul style="list-style-type: none"> <li>-HNO<sub>3</sub> (100%) Selectipur:MERCK 100453</li> <li>-HNO<sub>3</sub> (69%) VLSI: MERCK 116445</li> <li>-HNO<sub>3</sub> (100%) (I), 5min</li> <li>-HNO<sub>3</sub> (100%) (II), 5min</li> <li>-quick dump rinse, DI, &lt;0.1µS</li> <li>-HNO<sub>3</sub> (69%) (95°C), 15min</li> <li>-quick dump rinse, DI, &lt;0.1µS</li> <li>-spin drying</li> </ul>	<i>Removal of light organic particles and metals</i>
25b	<a href="#">Lithography-Olin907-17 liftoff/no-postbake</a>	<p><b>S&amp;A Litho Bench / ElectronicVisions Al-6</b></p> <ul style="list-style-type: none"> <li>--dehydration bake/priming scheme: Hotplate 140°C, 60 sec + gas priming of HMDS (<i>Gamma 60</i>)</li> <li>-resist: Olin 907/17, 4000rpm, 20s</li> <li>-prebake: hotplate 951C, 90sec</li> <li>-exposure parameters:</li> <li>4 xxx 201</li> <li>m</li> <li>4.0mm Hard contact</li> <li>301m</li> <li>3" Top/bot</li> <li>100/10N</li> <li>0.4mm xxx 5s</li> <li>2</li> <li>-after exposure bake 1201C, 60sec</li> <li>-development: OPD 4262, 45s</li> <li>-quick dump rinse, DI, &lt;0.1µS</li> <li>-spin drying</li> <li>-visual microscopic inspection</li> </ul>	Lift-off on 3" silicon substrates

Project : Distributed sensing  
 Author : John van Baar

File : procTCRkmf.sxw

Page : 8  
 Date: 10/30/02

26b	<a href="#">Sputtering of Cr</a>	Home built equipment "sputterke" Chroom target Gas/flow: Ar/ 45 sccm Temperature: water cooled electrode Base pressure 1.0E-6 mbar Sputter pressure: 5.0E-3 mbar Power 200W Deposition rate: 10nm/min	<a href="#">Deposition adhesion schemes</a>  Use Cr as adhesion layer for PT or Au when KOH and/or HF are used in the process time= 1 minute
27b	<a href="#">Sputtering of Pt</a>	Home built equipment "sputterke" Pt target Gas/flow: Ar/ 45 sccm Temperature: water cooled electrode Base pressure 1.0E-6 mbar Sputter pressure: 5.0E-3 mbar Power 200W Deposition rate: 20 nm/min	<a href="#">Deposition adhesion schemes</a>  Use Cr, Ti or Ta as adhesion layer for Pt When KOH and/or HF are involved use Cr time=10 minutes
28b	<a href="#">Lift-off Olin 907 in acetone</a>	<b>Wet Bench prep</b> -Acetone VLSI: MERCK 100038 -Isopropanol (VLSI) MERCK 107038 -acetone (dirty) BK1 -acetone (clean) BK2 -isopropanol (clean) BK3 -spin drying -visual microscopic inspection	Solutions are user made Optional: Use ultrasonic bath to enhance lift-off process
29b	<a href="#">Etching Si KOH-1</a>	<b>-Wet Bench KOH-prep</b> -prepare 25 gew% KOH p.a. (500gr KOH-1500ml DI) -etch temp.:75°C -stirrer  -SiO <sub>2</sub> (thermisch): 180 nm/hr -SiRN: < 1 nm/min -etchrate <100>: 1 µm/min -etchrate <111>: 12.5 nm/min -quick dump rinse, DI, <0.1µS -spin drying	time=250 minutes

Project : Distributed sensing  
 Author : John van Baar

File : procTCRkmf.sxw

Page : 9  
 Date: 10/30/02

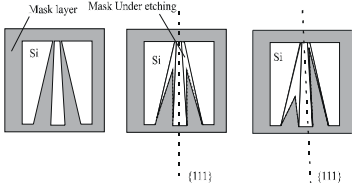
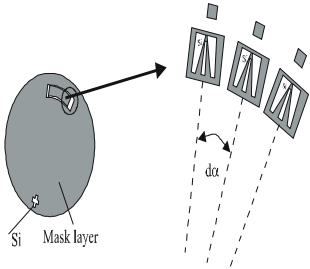
### Process scheme of cap

Step	Process	Parameters	Remarks
01t	<a href="#">Cleaning introduction</a>	<b>Wet Bench SC</b> -HNO3 (100%) Selectipur:MERCK 100453 -HNO3 (69%) VLSI: MERCK 116445  -HNO3 (100%) (II), 5min -quick dump rinse, DI, <0.1μS -HNO3 (69%) (951C), 15min -quick dump rinse, DI, <0.1μS -spin drying	<i>Removal of light organic particles and metals</i>
02t	<a href="#">LPCVD SiRN-S&amp;A (standard low stress)</a>	-Tempress LPCVD Furnace -Tube 6 S&A -program Nxx -SiH <sub>2</sub> Cl <sub>2</sub> flow 70sccm -NH <sub>3</sub> flow 18sccm -temperature 850°C -pressure 200mTorr -deposition rate 8.3nm/min (3`wafers) -deposition rate 7.3 nm/min (4`wafers) -Nf :2.14 -stress : 10,6*10-10 dyne/cm2 -uniformity (wafer)xxxxx % -uniformity (batch)xxxxx%	<b>Cleaning required</b> 150 nm
03t	<a href="#">Lithography-Olin907-17SSP</a>	<b>S&amp;A Litho Bench/ElectronicVisions AI-6</b> -dehydration bake/priming scheme: Hotplate 140°C, 60 sec + gas priming of HMDS ( <i>Gamma 60</i> ) -resist: Olin 907-17, 4000rpm, 20sec -prebake: hotplate 95°C, 90sec -Exposure parameters 4`or5` xxx 20μm 4.or6 mm xxx 30μm 3`/4` top/bot 100/10N 0.4/0.6mm xxx xxs (5sec) 2 -after exposure bake: 120°C, 60sec -development: OPD 4262, 45-60s -quick dump rinse, DI, <0.1μS -spin drying -visual microscopic inspection -postbake: hotplate 120°C, 30min	

Project : Distributed sensing  
 Author : John van Baar

File : procTCRkmf.sxw

Page : 10  
 Date: 10/30/02

<p>04t</p>	<p><a href="#">Plasma etching of SiN</a></p>	<p>-Elektrotech PF 310/340 (Etske)                  -dirty chamber                  -styros electrode                  -electrode temp.: 10°C                  -CHF<sub>3</sub> flow 25sccm                  -O<sub>2</sub> flow 5sccm                  -pressure 10mTorr                  -power 75W                  -etchrate SiN 60-90nm/min                  -etchrate Olin resist 95nm/min                  -profile: slightly tapered for PR                  -profile: directional for metal mask</p>	<p><b>Reservation necessary</b>                  time=3 minutes</p>
<p>05t</p>	<p><a href="#">Stripping of Olin 907 by oxygen plasma</a></p>	<p><b>Nanotech Plasmaprep 100</b>                  -O<sub>2</sub> flow 55sccm                  -power 120W                  -electrode temperature 150°C                  -pressure 2.00mbar                  -time 20min                  -visual microscopic inspection</p>	
<p>06t</p>	<p><a href="#">Etching Si KOH-crystal-alignment to {111}</a></p>	<p><b>Procedure Vangbo</b>                  Finding {111} orientation with etch structures <a href="#">[Vangbo96]</a></p>  <p>-Left: to find {111} planes,                  -Center: perfect alignment                  -Right: misaligned etch structure</p> <p>The etch mask structure used in [Vangbo96] can be seen in fig above. In the center fig. can be seen how symmetric under etch profiles arise when the etch structure is aligned parallel to an {111} plane. When the aligning is not perfect the under-etching is no longer symmetric (fig. right). In fig. below it can be seen how the structures can be used in the fabrication process.</p> 	

Project : Distributed sensing  
 Author : John van Baar

File : procTCRkmf.sxw

Page : 11  
 Date: 10/30/02

		<p>The etch structures, each with a slightly different orientation, are placed on a circle, where the origin of the circle is the cross shown on the wafer drawn left in the figure. This cross is one alignment mark for following lithographic steps. The second alignment mark is the mark standing above the etch structure that shows a symmetric under etch profile after KOH etch (and is thus aligned to the (111) orientation).</p>	
07t	<a href="#">Etching Si KOH-1</a>	<p><b>-Wet Bench KOH-prep</b>          -prepare 25 gew% KOH p.a. (500gr KOH-1500ml DI)          -etch temp.:75°C          -stirrer</p> <p>-SiO<sub>2</sub> (thermisch): 180 nm/hr          -SiRN: &lt; 1 nm/min          -etchrate &lt;100&gt;: 1 µm/min          -etchrate &lt;111&gt;: 12.5 nm/min          -quick dump rinse, DI, &lt;0.1µS          -spin drying</p>	Time=11'30''
08t	<a href="#">Cleaning RCA-2 (HCL/H2O2/H2O)</a>	<p><b>Wet Bench RCA</b>          -HCL (32%) Selectipur: MERCK 100322          -H2O2 (31%) VLSI: MERCK 108552</p> <p>-add HCLto H2O          -HCL:H2O: H2O2 (1:6:1) vol%          -add H2O2 when mixture is 70          -temperature 75-80 °C          -time 10-15 min          -quick dump rinse, DI, &lt;0.1µS          -spin drying</p>	<i>Dissolves alkali ions, and hydroxides of Al, Fe, Mg and Cu, Au</i>
09t	<a href="#">Cleaning online</a>	<p><b>Wet Bench SC</b>          -HNO<sub>3</sub> (100%) Selectipur:MERCK 100453          -HNO<sub>3</sub> (69%) VLSI: MERCK 116445</p> <p>-HNO<sub>3</sub> (100%) (I), 5min          -HNO<sub>3</sub> (100%) (II), 5min          -quick dump rinse, DI, &lt;0.1µS          -HNO<sub>3</sub> (69%) (95°C), 15min          -quick dump rinse, DI, &lt;0.1µS          -spin drying</p>	<i>Removal of light organic particles and metals</i>

Project : Distributed sensing  
 Author : John van Baar

File : procTCRkmf.sxw

Page : 12  
 Date: 10/30/02

10t	<a href="#">Lithography-Olin907-17SSP</a>	<b>S&amp;A Litho Bench/ElectronicVisions AI-6</b> -dehydration bake/priming scheme: Hotplate 140°C, 60 sec + gas priming of HMDS ( <i>Gamma 60</i> ) -resist: Olin 907-17, 4000rpm, 20sec -prebake: hotplate 95°C, 90sec -Exposure parameters 4"or5"      xxx      20µm 4.or6 mm    xxx      30µm 3"7/4"      top/bot      100/10N 0.4/0.6mm   xxx      xxs (5sec) 2 -after exposure bake: 120°C, 60sec -development: OPD 4262, 45-60s -quick dump rinse, DI, <0.1µS -spin drying -visual microscopic inspection -postbake: hotplate 120°C, 30min	front side mask: "top cap"
11t	<a href="#">Plasma etching of SiN</a>	-Elektrotech PF 310/340 (Etske) -dirty chamber -styros electrode -electrode temp.: 10°C -CHF <sub>3</sub> flow 25sccm -O <sub>2</sub> flow 5sccm -pressure 10mTorr -power 75W -etchrate SiRN 60-90nm/min -etchrate Olin resist 95nm/min -profile: slightly tapered for PR -profile: directional for metal mask	<b>Reservation necessary</b> time=15 minutes
12t	<a href="#">Stripping of Olin 907 by oxygen plasma</a>	<b>Nanotech Plasmaprep 100</b> -O <sub>2</sub> flow 55sccm -power 120W -electrode temperature 150°C -pressure 2.00mbar -time 20min -visual microscopic inspection	
13t	<a href="#">Cleaning online</a>	<b>Wet Bench SC</b> -HNO <sub>3</sub> (100%) Selectipur:MERCK 100453 -HNO <sub>3</sub> (69%) VLSI: MERCK 116445  -HNO <sub>3</sub> (100%) (I), 5min -HNO <sub>3</sub> (100%) (II), 5min -quick dump rinse, DI, <0.1µS -HNO <sub>3</sub> (69%) (95°C), 15min -quick dump rinse, DI, <0.1µS -spin drying	<b>Removal of light organic particles and metals</b>

Project : Distributed sensing  
 Author : John van Baar

File : procTCRkmf.sxw

Page : 13  
 Date: 10/30/02

14t	<a href="#">Lithography-Olin907-17SSP</a>	<p><b>S&amp;A Litho Bench/ElectronicVisions AI-6</b>          -dehydration bake/priming scheme:          Hotplate 140°C, 60 sec + gas priming of HMDS (<i>Gamma 60</i>)          -resist: Olin 907-17, 4000rpm, 20sec          -prebake: hotplate 95°C, 90sec          -Exposure parameters          4"or5"      xxx      20µm          4.or6 mm    xxx      30µm          3"7/4"      top/bot    100/10N          0.4/0.6mm   xxx      xxs          (5sec)          2          -after exposure bake: 120°C, 60sec          -development: OPD 4262, 45-60s          -quick dump rinse, DI, &lt;0.1µS          -spin drying          -visual microscopic inspection          -postbake: hotplate 120°C, 30min</p>	back side mask: "bottom cap"
15t	<a href="#">Plasma etching of SiN</a>	<p>-Elektrotech PF 310/340 (Etske)          -dirty chamber          -styros electrode          -electrode temp.: 10°C          -CHF<sub>3</sub> flow 25sccm          -O<sub>2</sub> flow 5sccm          -pressure 10mTorr          -power 75W          -etchrate SiRN 60-90nm/min          -etchrate Olin resist 95nm/min          -profile: slightly tapered for PR          -profile: directional for metal mask</p>	<b>Reservation necessary</b> time = 15 minutes
16t	<a href="#">Stripping of Olin 907 by oxygen plasma</a>	<p><b>Nanotech Plasmaprep 100</b>          -O<sub>2</sub> flow 55sccm          -power 120W          -electrode temperature 150°C          -pressure 2.00mbar          -time 20min          -visual microscopic inspection</p>	
17t	<a href="#">Etching Si KOH-1</a>	<p><b>-Wet Bench KOH-prep</b>          -prepare 25 gew% KOH p.a. (500gr KOH-1500ml DI)          -etch temp.:75°C          -stirrer            -SiO<sub>2</sub> (thermisch): 180 nm/hr          -SiRN: &lt; 1 nm/min          -etchrate &lt;100&gt;: 1 µm/min          -etchrate &lt;111&gt;: 12.5 nm/min          -quick dump rinse, DI, &lt;0.1µS          -spin drying</p>	time=250 minutes





# Appendix B

## Theory

The formulas required for the proposed structures for the determination of the flow velocity and the fluid parameters thermal conductivity, density, specific heat and dynamic viscosity will be discussed in this appendix. A short introduction to hydrodynamics, heat transfer, electricity and mechanics and the analogy between the domains will be given. The analytical expression of the one dimensional temperature distribution in cartesian and cylindrical coordinates will be derived, because this is used for structures with a beam and a circular membrane, respectively. A coefficient before the dependent variable of the differential equation depends on the independent variable, which forces us to use lumped element models. The derivation of the nodal matrix for the lumped element will be given. The principle of Pirani pressure sensor will be explained using statistical mechanics.

### B.1 Physical domains

For our structures four physical domains can be distinguished: the hydraulical, thermal, electrical and mechanical domain. The governing equations will be given for each domain and also the similarity parameters derived from the equations, like the Reynolds number and the Prandtl number.

The basic equations for the different domains are quite similar. The symbols for each domain are given in table B.1. Generalized one can speak about the effort  $e$ , which takes care of the equilibrium and causes the flow  $f$ . The lumped elements are the buffering element  $C$ , which buffers the state  $q$ , the buffering elements  $I$ , which buffers the generalized impulse  $p$  and the resistance  $R$ . The formulas are  $q = Ce$  and  $R = \frac{e}{f}$ ,  $p = If$  and the power  $P = ef$ . In the thermal domain the  $I$  does not exist.

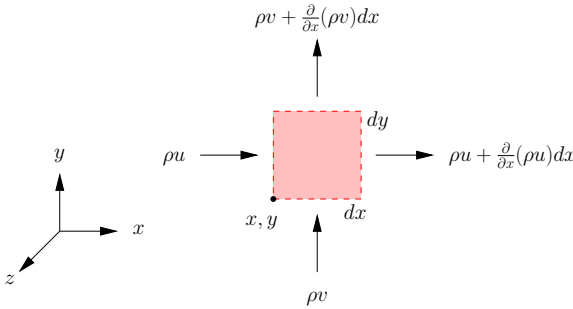
#### B.1.1 Hydraulical

From the divergency of a control volume the continuity equation can be derived. The two dimensional form is shown in figure B.1 and given by:

$$\frac{\partial(\rho u)}{\partial x} + \frac{\partial(\rho v)}{\partial y} = 0 \quad (\text{B.1})$$

**Table B.1:** Overview of the symbols for the domains of interest

domain	state	flow	effort	generalized impulse
	$q$	$f = \frac{dq}{dt}$	$e$	$p = \int edt$
electrical	$q [C]$	$i [A]$	$u [V]$	$\phi [Wb]$
hydraulic	$V [m^3]$	$\phi [m^3/s]$	$p [Pa]$	$\Gamma [Pas]$
mechanical (translation)	$x [m]$	$v [m/s]$	$F [N]$	$p [Ns]$
thermal	$S [J/K]$	$f_S [W/K]$	$T [K]$	fundamental hiatus
pseudo thermal	$Q [J/K]$	$f_Q [W/K]$	$T [K]$	fundamental hiatus

**Figure B.1:** Differential control volume for mass conservation (2D).

with  $\rho$  the density in  $[kg/m^3]$  and  $u$  and  $v$  the velocities in  $[m/s]$  in the  $x$ - and  $y$ -direction respectively.

Applying Newton's second law of motion in one dimension, see figure B.2, which states that the net surface forces balances the fluid momentum fluxes, gives:

$$\rho \left( u \frac{\partial u}{\partial x} + v \frac{\partial u}{\partial y} \right) = \frac{\partial}{\partial x} (\sigma_{xx} - p) + \frac{\partial \tau_{yx}}{\partial x} + X \quad (\text{B.2})$$

with  $\sigma_{xx}$  the normal stress in  $[Pa]$ ,  $\tau_{yx}$  the shear stress in  $[Pa]$ ,  $p$  the pressure in  $[Pa]$  and  $X$  the body forces. To simplify this equation a Newtonian fluid has been assumed and the fluid is characterized as incompressible ( $\rho$  is constant). Because the boundary layer thicknesses are typically very small  $u \gg v$  and  $\frac{\partial u}{\partial y} \gg \frac{\partial u}{\partial x}, \frac{\partial v}{\partial y}, \frac{\partial v}{\partial x}$  can be taken, resulting in:

$$u \frac{\partial u}{\partial x} + v \frac{\partial u}{\partial y} = -\frac{1}{\rho} \frac{\partial p}{\partial x} + \nu \frac{\partial^2 u}{\partial y^2} \quad (\text{B.3})$$

with  $\nu$  the kinematic viscosity in  $[m^2/s]$ . Using the dimensionless parameters  $x^* \equiv \frac{x}{L}$ ,  $y^* \equiv \frac{y}{L}$ ,  $u^* \equiv \frac{u}{V}$ ,  $v^* \equiv \frac{v}{V}$  and  $p^* = \frac{p}{\rho V^2}$ , where  $L$  is the characteristic length in  $[m]$  and  $V$  the velocity upstream of the surface in  $[m/s]$ , the equation becomes:

$$u^* \frac{\partial u^*}{\partial x^*} + v^* \frac{\partial u^*}{\partial y^*} = -\frac{\partial p^*}{\partial x^*} + \frac{1}{Re_L} \frac{\partial^2 u^*}{\partial y^{*2}} \quad (\text{B.4})$$

with the Reynolds number defined as:

$$Re_L = \frac{V L}{\nu} \quad (\text{B.5})$$

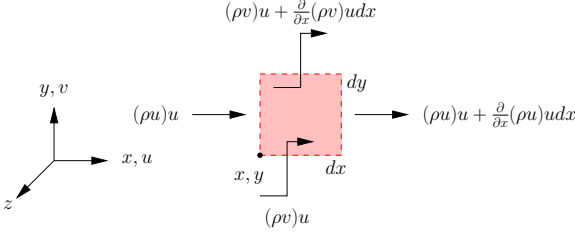


**Figure B.2:** Momentum fluxes for differential control volume (2D).

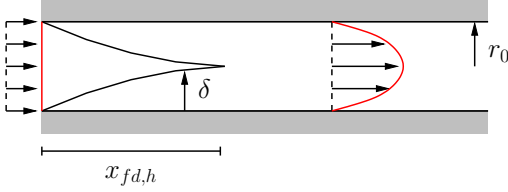


**Figure B.3:** Laminar, hydrodynamic boundary layer development in circular tube, with boundary layer thickness  $\delta$  and outer radius  $r_0$ .

For laminar flow in a circular duct the Reynolds number has to be smaller than 2300. Due to the small diameter of the micromachined channels a laminar flow is expected. In laminar flow the hydrodynamic entrance length  $x_{fd,h}$  [m], the developing length for a flow in a circular duct from a uniform to a parabolic flow profile, is

$$\frac{x_{fd,h}}{D} \approx 0.05 Re_D \tag{B.6}$$

with  $D$  the diameter of the duct in [m], see figure B.3. This formula is used for the flow sensor in the hexagonal duct to predict the flow is laminar at the beam.

In the fully developed region of a duct  $v = 0$  and  $\frac{\partial u}{\partial x} = 0$  equation B.3 becomes

$$0 = -\frac{1}{\rho} \frac{\partial p}{\partial x} + \nu \frac{\partial^2 u}{\partial y^2} \tag{B.7}$$

From the x-momentum equation the balance between shear and pressure forces of a flow in a circular duct is:

$$-\frac{1}{r} \frac{d}{dr} (r\tau_r) = \frac{dp}{dx} \tag{B.8}$$

with  $\frac{dp}{dx}$  the pressure gradient,  $\tau_r$  [Pa] the shear stress and  $r$  [m] the radius. Combined with Newton's law of viscosity

$$\tau_r = -\mu \frac{du}{dr} \tag{B.9}$$

with  $\mu$  the dynamic viscosity. Applying the boundary conditions  $u(r_0) = 0$  and  $\frac{\partial u}{\partial r}|_{r=0} = 0$  and zero slip at the tube surface, results in

$$u(r) = -\frac{1}{4\mu} \left( \frac{dp}{dx} \right) r_0^2 \left( 1 - \left( \frac{r}{r_0} \right)^2 \right) \tag{B.10}$$

with  $r_0$  [m] the radius of the duct.

Taking the mean velocity  $u_m = \frac{2}{r_0^2} \int_0^{r_0} u(r) r dr$  equation B.10 can be written as

$$u_m = -\frac{r_0^2}{8\mu} \frac{dp}{dx} \quad (\text{B.11})$$

The velocity profile will be:

$$\frac{u(r)}{u_m} = 2 \left( 1 - \left( \frac{r}{r_0} \right)^2 \right) \quad (\text{B.12})$$

In our hexagonal channel with aspect ratio 1/2 we assume this velocity profile.

The boundary thickness  $\delta$  [m] can be derived from the continuity, momentum equation and Blasius similarity solution and with  $u/u_\infty = 0.99$  it becomes

$$\delta = \frac{5.0}{\sqrt{u_\infty/\nu x}} = \frac{5x}{\sqrt{Re_x}} \quad (\text{B.13})$$

with  $x$  the distance from the leading edge in [m] and  $Re_x$  the local Reynolds number.

The hydraulic resistance of a channel is defined as the pressure drop over a channel with volume change  $\dot{V}$ :

$$R = \frac{p}{\dot{V}} \quad (\text{B.14})$$

with  $\dot{V}$  [ $m^3$ ] the volume change and  $p$  [Pa] the pressure drop. This can be used to apply a pressure drop over the differential pressure sensor using a restriction and a flow.

### B.1.2 Thermal

The first law of thermodynamics, which is a special form of the law of conservation of energy, for a control volume is:

$$\dot{E}_{in} + \dot{E}_g - \dot{E}_{out} = \frac{dE_{st}}{dt} \quad (\text{B.15})$$

with the rate of the thermal and mechanical energy enter and leave the control surface,  $\dot{E}_{in}$  and  $\dot{E}_{out}$ . The  $\dot{E}_g$  is the energy generation and  $\frac{dE_{st}}{dt}$  is the energy storage.

When no phase transition takes place and when the heat transfer only results in a change in the body temperature, the right-hand side of equation B.15 can be replaced by  $\rho c_p \frac{dT}{dt}$ , with  $c_p$  the specific heat at constant pressure in [ $J/(kgK)$ ] and  $\rho$  the density.

Equation B.16 is Fourier's law of heat conduction for a unidirectional substance:

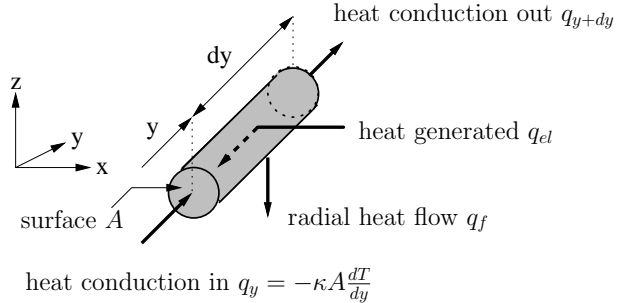


**Figure B.4:** Heat balance for control volume.

$$q_x'' = -\kappa \frac{dT}{dx} \quad (\text{B.16})$$

with  $q''$  [ $W/m^2$ ] the heat flux through a surface<sup>1</sup>,  $\kappa$  [ $W/(Km)$ ] the thermal conductivity.

Taking a Taylor series expansion and neglecting higher order terms result in:

$$q''_{x+dx} = q''_x + \frac{\partial q_x}{\partial x} dx \quad (B.17)$$

The net conduction heat flux into the control volume in the x-direction is

$$q''_x - q''_{x+dx} = \frac{\partial}{\partial x} \left( \kappa \frac{\partial T}{\partial x} \right) dx \quad (B.18)$$

For three dimensions and constant thermal conductivity and a generation term it becomes:

$$\nabla^2 T + \frac{\dot{q}}{\kappa} = \frac{1}{\alpha} \frac{\partial T}{\partial t} \quad (B.19)$$

with  $\alpha = \kappa/(\rho c)$  [ $m^2/s$ ] the diffusion coefficient and  $\dot{q}$  [ $W/m^3$ ] the power density.

The energy equation is defined as:

$$u \frac{\partial T}{\partial x} + v \frac{\partial T}{\partial y} = \alpha \frac{\partial^2 T}{\partial y^2} + \frac{\nu}{c_p} \left( \frac{\partial u}{\partial y} \right)^2 \quad (B.20)$$

Using  $T^* = \frac{T-T_s}{T_\infty-T_s}$  and the earlier mentioned parameters and the assumption of negligible viscous dissipation result in:

$$u^* \frac{\partial T^*}{\partial x^*} + v^* \frac{\partial T^*}{\partial y^*} = \frac{1}{Re_L Pr} \frac{\partial^2 T^*}{\partial y^{*2}} \quad (B.21)$$

with the Prandtl number

$$Pr = \frac{\nu}{\alpha} \quad (B.22)$$

For many gases the Prandtl number is around 0.7 at room temperature.

The thermal resistance  $R_{therm}$  [ $K/W$ ] in cartesian coordinates, with  $l$  [ $m$ ] the length and  $A$  [ $m^2$ ] the area, is defined as

$$\frac{\Delta T}{Q} = R_{therm} = \frac{l}{\kappa A} \quad (B.23)$$

The Nusselt number is equal to the dimensionless temperature gradient at the surface and provides a measure of the convection heat transfer occurring at the surface.

$$Nu = \frac{hL}{\kappa_f} = + \frac{\partial T^*}{\partial y^*} \Big|_{y^*=0} \quad (B.24)$$

with  $h$  the heat transfer coefficient. For a flat plate in laminar parallel flow from the similarity solution the local Nusselt number can be obtained:

$$Nu = \frac{h_x x}{\kappa} = 0.332 Re_x^{\frac{1}{2}} Pr^{\frac{1}{3}} \quad (B.25)$$

---

<sup>1</sup>the number of ' stands for the number of dimensions

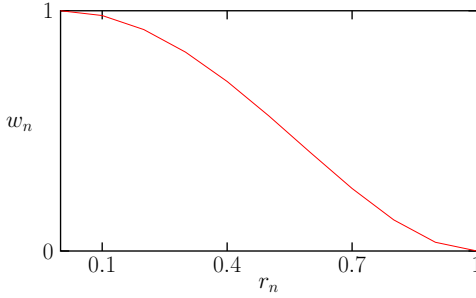


**Figure B.5:** Normalized deflection  $w_n$  versus the normalized position  $r_n$

with  $Pr \geq 0.6$ . The average Nusselt number is

$$\bar{Nu} = \frac{h_x x}{\kappa} = 0.664 Re_x^{\frac{1}{2}} Pr^{\frac{1}{3}} \quad (\text{B.26})$$

Taking the thermal conduction into account King's law can be recognized, which is defined as

$$T_s - T_{amb} = \frac{P_{gen}}{G_0 + K\sqrt{|v|}} \quad (\text{B.27})$$

with  $T - T_{amb}$  the temperature rise with respect to ambient temperature,  $P [W]$  the generated heat,  $v [m/s]$  the velocity,  $G [W/(Km)]$  the thermal conduction to the fluid and  $K$  a parameter depending on the fluid properties.

### B.1.3 Electrical

The electrical resistance  $R [\Omega]$  in cartesian coordinates is defined by Ohm's law

$$R = \frac{U}{I} = \rho \frac{l}{A} \quad (\text{B.28})$$

with  $\rho [\Omega m]$  the resistivity,  $U [V]$  the potential and  $I [A]$  the current,  $l [m]$  the length and  $A [m^2]$  the area.

The generation of heat (Joule heating)  $Q [W]$  is

$$Q = R_h I^2 \quad (\text{B.29})$$

with  $R_h [\Omega]$  the electrical resistance and  $I [A]$  the applied current.

The resistive structure on the membrane is used as heater and as sensor. The resistance is temperature dependent following

$$R = R_0 (1 + \alpha \Delta T) \quad (\text{B.30})$$

with  $\alpha [K^{-1}]$  the temperature coefficient of resistance and  $R_0$  the resistance at  $\Delta T = 0$

### B.1.4 Mechanical

For a circular membrane with radius  $R$  [m] the deflection  $w$  [m] and the boundary conditions  $w(r = R) = 0$  and  $(dw/dr)|_{r=0} = 0$  is given by [12]:

$$w(r) = \frac{3}{16} \frac{1 - \nu^2}{Eh^3} (R^2 - r^2)^2 \cdot \Delta p \tag{B.31}$$

with  $\nu$  the Poisson ratio,  $E$  [Pa] the Young's modulus,  $h$  [m] the thickness,  $\Delta p$  [Pa] the pressure drop and  $r$  [m] the radius from the center of the membrane.

## B.2 1D temperature distributions

In steady state ( $\frac{\partial T}{\partial t}$ ) general equation B.19 becomes

$$\nabla^2 T + \frac{\dot{q}}{\kappa} = 0 \tag{B.32}$$

This contains only the heat generation and the conduction through the beam to the support. Taking in account the heat transfer to the fluid a term,  $\dot{G}_f$  [W/(Km<sup>3</sup>)] the thermal conductance density to the fluid, has to be added:

$$\kappa \nabla^2 T - \dot{G}_f T + \dot{q} = 0 \tag{B.33}$$

For the one dimensional situation this is applied for a beam, in cartesian coordinates, and is applied for a circular membrane, in polar coordinates. The analytical solutions of the ordinary differential equations will be given in the next sections.

Introducing non linearities in the differential equation by making a coefficient depending on the dependent variable makes it hard to solve the differential equation. A numerical solution is obtained by using a lumped element model. A simple example is given to understand the principle, see figure B.6, The equation for each node is based on Kirchhoff currents law ( $\sum_1^n I_i = 0$ ).

$$(V_1 - V_3) G_1 + (V_1 - V_2) G = I_1 \tag{B.34}$$

$$(V_2 - V_1) G + (V_2 - V_3) G_2 = I_2 \tag{B.35}$$

$$(V_1 - V_3) G_1 + (V_2 - V_3) G_2 = I_1 + I_2 \tag{B.36}$$

Rewriting the equations into nodal admittance matrix form:

$$\begin{pmatrix} G + G_1 & -G & -G_1 \\ -G & G + G_2 & -G_2 \\ -G_1 & -G_2 & G_1 + G_2 \end{pmatrix} \begin{pmatrix} V_1 \\ V_2 \\ V_3 \end{pmatrix} = \begin{pmatrix} I_1 \\ I_2 \\ -I_1 - I_2 \end{pmatrix}$$

The reference node (3) is a linear combination of the others and can be used as a check or just leaved out. The summation of the elements along a row or column is zero [58]. The nodal admittance matrix is inverted using LU-factorization and is multiplied by the power to obtain the temperature distribution.

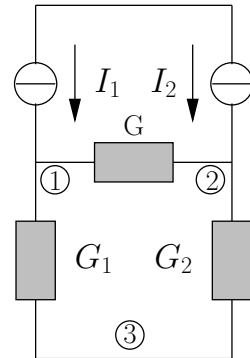


**Figure B.6:** Simple lumped element model

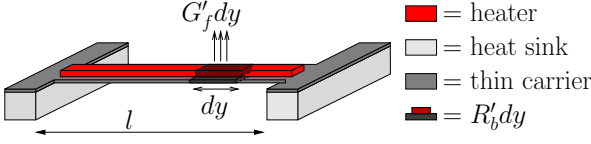


**Figure B.7:** Model of the beam with line conductance to the fluid  $G'_f$ , line resistance of the beam  $R'_b$  and beam length  $l$ .

## B.2.1 Cartesian coordinates

### analytical

For a homogeneously heated beam with only heat transfer through the beam in the  $y$ -direction equation B.33 becomes

$$A\kappa \frac{d^2 T}{dy^2} - G'_f T + q' = 0 \quad (\text{B.37})$$

with  $q'$  [ $W/m$ ] the line power and  $G'_f$  [ $W/(Km)$ ] the line conductance to the fluid.

A model is shown in figure B.7. Substituting the normalized position  $y_n = y/l$  and thermal line resistance  $R'_b = (A\kappa)^{-1}$  [ $K/(Wm)$ ] results in

$$\frac{1}{R'_b l^2} \frac{d^2 T}{dy_n^2} - G'_f T + q' = 0 \quad (\text{B.38})$$

The solution of equation B.38 is given by [1]

$$\Delta T(\mathbf{y}_n) = \frac{P'}{G'_f} \left( 1 - \frac{\cosh\left(y_n \cdot l \sqrt{R'_b G'_f}\right)}{\cosh\left(\frac{1}{2} l \sqrt{R'_b G'_f}\right)} \right) \quad (\text{B.39})$$

Figure B.8(a) shows a plot of the solution of equation B.38 for several values of the thermal line conductance to the fluid  $G'_f$ , ranging from 0 to 0.1 with fixed thermal line resistance of the beam  $R'_b$ . The shape of the temperature distribution changes when  $G'_f$  is varied by for example a pressure or a uniform flow.

Normalizing the temperature distribution of equation B.39 to the temperature rise at the center of the beam results in:

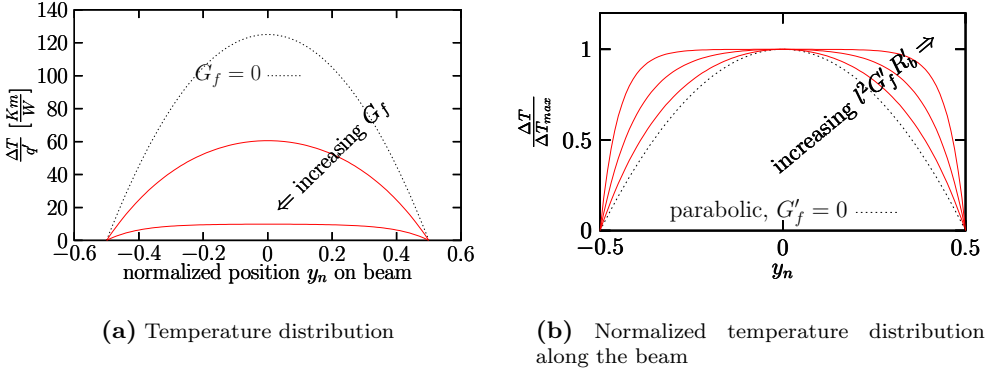
$$T_n(\mathbf{y}_n) = \frac{\Delta T(\mathbf{y}_n)}{\Delta T(0)} = \frac{\cosh\left(\frac{1}{2} l \sqrt{R'_b G'_f}\right) - \cosh\left(y_n \cdot l \sqrt{R'_b G'_f}\right)}{\cosh\left(\frac{1}{2} l \sqrt{R'_b G'_f}\right) - 1} \quad (\text{B.40})$$

Figure B.8(b) shows a plot of this normalized temperature distribution for several values of the term  $l \sqrt{R'_b G'_f}$  ranging from 0 to 20. The advantage of normalizing in this manner is the canceling out of the Temperature Coefficient of Resistance, which is otherwise needed to know the temperature.

### lumped element model

In the case  $G'_f$  is depending on the position a lumped element model is used. From the lumped element model of figure B.9 via Kirchhoff's current law the following matrix  $\mathbf{A}$  can be derived. The lumped element has  $n$  nodes and the  $n + 1$ st node is the





**Figure B.8:** The temperature distribution per unit power and the normalized temperature distribution versus the normalized position on the beam as function of the shape parameter  $R'_b G'_f l^2$ .

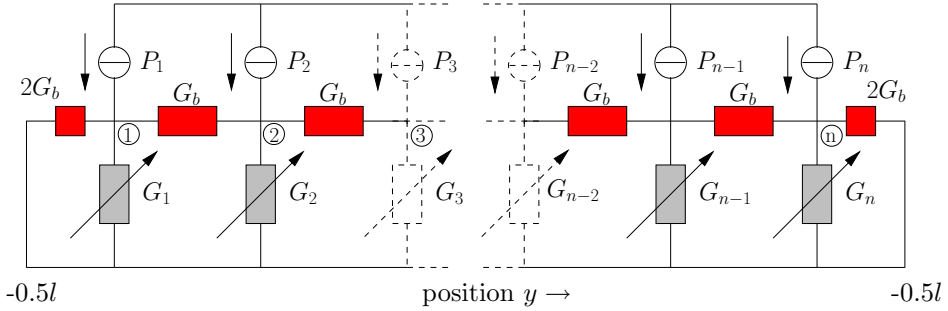


**Figure B.9:** Lumped thermal model of a beam with  $G_b$  [K/W] the thermal conductance of the beam,  $G_i$  [K/W] the flow-dependent thermal conductance to the fluid and  $P$  the power [W].

ground. The last is a superposition of the others, indicated by the filled block. This is only a check. The inverted matrix of  $\mathbf{A}$  multiplied by  $\mathbf{P}$  results in the temperature distribution:  $T = \mathbf{A}^{-1}\mathbf{P}$  with

$$\mathbf{A} = \begin{pmatrix} 3G_b + G_1 & -G_b & 0 & \dots & \dots & 0 & 0 & -2G_b - G_1 \\ -G_b & G_2 + 2G_b & -G_b & & & 0 & 0 & -G_2 \\ \vdots & & & \ddots & & & \vdots & \vdots \\ \vdots & & & & \ddots & & \vdots & \vdots \\ 0 & 0 & 0 & 0 & -G_b & G_{n-1} + 2G_b & -G_b & -G_{n-1} \\ 0 & 0 & 0 & 0 & 0 & -G_b & 3G_b + G_n & -G_n - 2G_b \\ -2G_b - G_1 & -G_2 & \dots & & -G_{n-1} & -2G_b - G_n & \star & \end{pmatrix}$$

$\star 2G_b + G_1 + G_2 + \dots + G_{n-1} + G_n + 2G_b$

and  $\mathbf{P} = [P_1 \ P_2 \ \dots \ P_{n+1} \ P_n \ -P]^t$  with  $P_i = P/n$

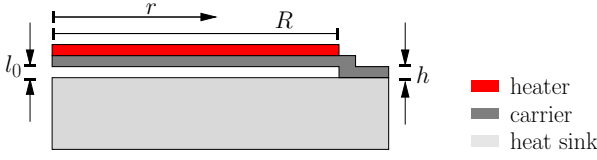


**Figure B.10:** Schematic drawing of bending membrane with gap distance  $l_0$  and thickness  $h$

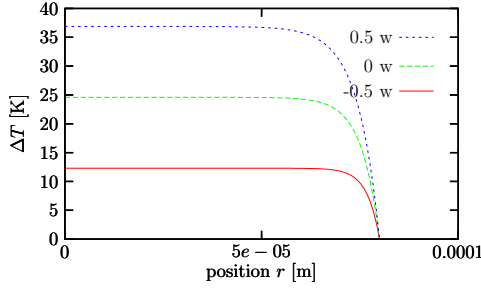


**Figure B.11:** Temperature distribution for several uniform  $G_f$

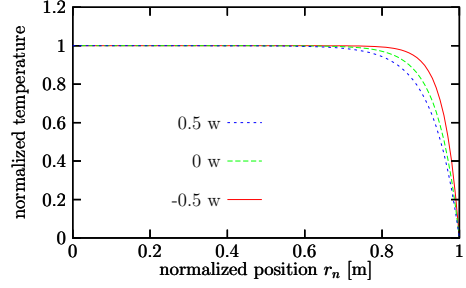


**Figure B.12:** Normalized temperature distribution for several uniform  $G_f'' R_b''$

## B.2.2 Polar coordinates

For polar coordinates equation B.33  $\nabla^2 T$  is written as

$$\nabla^2 T = \frac{1}{r} \frac{\partial}{\partial r} \left( r \frac{\partial T}{\partial r} \right) + \frac{1}{r^2} \frac{\partial^2 T}{\partial \theta^2} + \frac{\partial^2 T}{\partial z^2} \quad (\text{B.41})$$

Taking  $\frac{\partial T}{\partial \theta} = 0$  and  $\frac{\partial T}{\partial z} = 0$  it simplifies to

$$\frac{d^2 T}{dr^2} + \frac{1}{r} \frac{dT}{dr} \quad (\text{B.42})$$

### analytical

The differential equation becomes:

$$-h\kappa_s \left( \frac{d^2 T}{dr^2} + \frac{1}{r} \frac{dT}{dr} \right) + \frac{\kappa_f}{l} T = Q'' \quad (\text{B.43})$$

with  $\kappa_s$  and  $\kappa_f$  the thermal conductivity of the solid membrane and fluid, respectively, and  $Q''$  [ $W/m^2$ ] the applied heating power per area.

Using the boundary conditions  $T(R) = 0$  and  $\frac{T(0)}{dr} = 0$  and taking for the thermal square conductance  $G_f'' = \frac{\kappa_f}{l}$  [ $W/(Km^2)$ ] and the thermal square resistance of the membrane  $R_s'' = \frac{1}{\kappa_s h}$  [ $K/W$ ] the solution becomes:

$$T(r) = \frac{Q''}{G_f''} \left( 1 - \frac{\text{BesselJ}_0 \left( r \sqrt{-G_f'' R_s''} \right)}{\text{BesselJ}_0 \left( R \sqrt{-G_f'' R_s''} \right)} \right) \quad (\text{B.44})$$

This solution is plotted in figure B.11 as function of several homogeneous deflections of the membrane.

$$T_n(r) = \frac{\text{Bessel}J_0 \left( R\sqrt{-G_f''R_s''} \right) - \text{Bessel}J_0 \left( r\sqrt{-G_f''R_s''} \right)}{\text{Bessel}J_0 \left( R\sqrt{-G_f''R_s''} \right) - 1} \quad (\text{B.45})$$

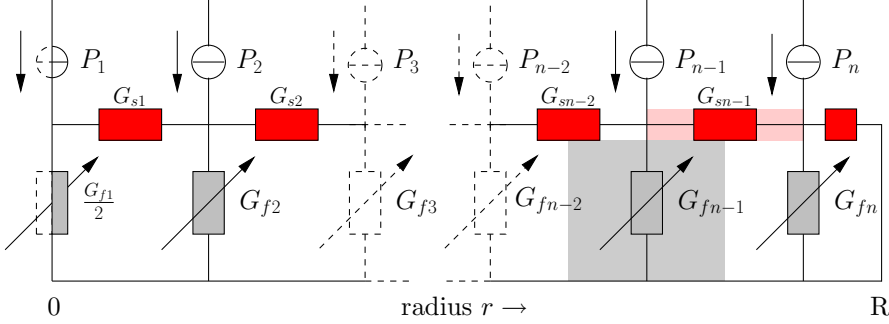


**Figure B.13:** Lumped element model used for calculating the temperature distribution of a deflected membrane.

### lumped element model

For the situation with (nonuniform) gap distance  $l = l_0 - w(r)$  the differential equation of equation B.43 is hard to solve. Therefore a lumped element model has been used, see figure B.13. For the thermal conductance of the beam a singularity exists for  $r = 0$ . A small value has been taken. The expressions for the lumped elements are:

$$G_{si} = \frac{2\pi h\kappa_s}{\ln\left(\frac{r_{i+1}}{r_i}\right)} \quad \text{for} \quad \frac{r_i}{R} = \left[ \frac{1}{2(n-1)+1} [2^{-9} \ 2 : 2 : 2(n-1)] \ 1 \right] \quad (\text{B.46})$$

$$G_{fi} = \frac{\kappa_f \pi (r_i^2 - r_{i-1}^2)}{l} \quad \text{for} \quad \frac{r_i}{R} = 0 : \frac{1}{2(n-1)+1} : \frac{2}{2(n-1)+1} : 1 \quad (\text{B.47})$$

$$Q_i = 2\pi (r_i^2 - r_{i-1}^2) Q'' \quad \text{for} \quad \frac{r_i}{R} = 0 : \frac{1}{2(n-1)+1} : \frac{2}{2(n-1)+1} : 1 \quad (\text{B.48})$$

## B.3 2D temperature distributions

The temperature distribution of an infinite long heater above a v-groove is modeled using a lumped element model. From the temperature distribution and the applied power the thermal conductance can be calculated.

In this model only the heat transfer in the direction perpendicular to the beam is considered: no heat transfer through the beam to its edges is assumed. The dark gray elements represent the thermal conductances in horizontal direction and the light gray elements represent the conductances in vertical direction. The sum of the ratios between the applied power  $P_i$  and the temperature difference  $T_j$  between the beam and the heat sink gives the value of the effective thermal conductance  $G_f'$ , with in the

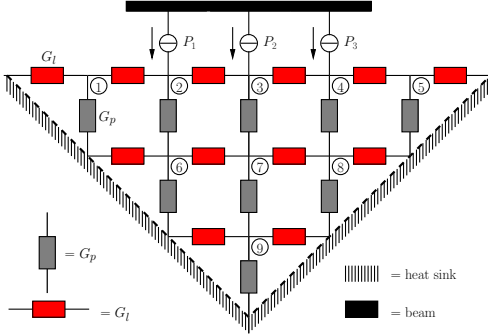


**Figure B.14:** Lumped element model with nine nodes drawn

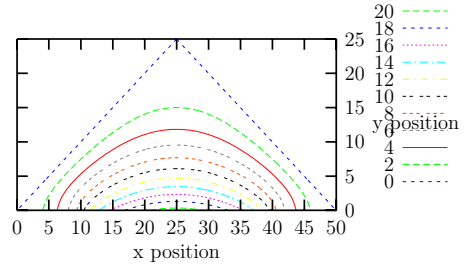


**Figure B.15:** Contour plot of the temperature in the v-groove

case of figure B.14  $i=1,2,3$  and  $j=2,3,4$ . In figure B.15 the temperature distribution in the gap is shown.

The nodal admittance matrix is:

$$\begin{pmatrix} 2G_l + G_p & -G_l & 0 & 0 & 0 & 0 & 0 & 0 & 0 & 0 \\ -G_l & 2G_l + G_p & -G_l & 0 & 0 & -G_p & 0 & 0 & 0 & 0 \\ 0 & -G_l & 2G_l + G_p & -G_l & 0 & 0 & -G_p & 0 & 0 & 0 \\ 0 & 0 & -G_l & 2G_l + G_p & -G_l & 0 & 0 & -G_p & 0 & 0 \\ 0 & 0 & 0 & -G_l & 2G_l + G_p & 0 & 0 & 0 & -G_p & 0 \\ 0 & -G_p & 0 & 0 & 0 & 2G_l + 2G_p & -G_l & 0 & 0 & 0 \\ 0 & 0 & -G_p & 0 & 0 & -G_l & 2G_l + 2G_p & -G_l & -G_p & -G_p \\ 0 & 0 & 0 & -G_p & 0 & 0 & -G_l & 2G_l + 2G_p & 0 & -G_p \\ 0 & 0 & 0 & 0 & -G_p & 0 & 0 & -G_l & 2G_l + 2G_p & 0 \\ 0 & 0 & 0 & 0 & 0 & 0 & -G_p & 0 & 0 & 2G_l + 2G_p \end{pmatrix}$$

with  $P_i$  power per source

$$\begin{pmatrix} 0 & P_1 & P_2 & P_3 & 0 & 0 & 0 & 0 & 0 & 0 \end{pmatrix}^{-1} \begin{matrix} G_l \text{ longitudinal thermal conductivity} \\ G_p \text{ perpendicular thermal conductivity} \end{matrix}$$

## B.4 Pirani sensor and thermal conductivity

To understand the relations between the macroscopic parameter thermal conductivity the "statistical mechanics" for a system in equilibrium will be used. It yields results of thermodynamics plus a large number of general relations for calculating the macroscopic parameters of the system from a knowledge of its microscopic constituents. It is based on the *microscopic*<sup>2</sup> properties of the particles in the system and on the laws of mechanics governing their behavior [57].

### B.4.1 Calculation of the thermal conductivity for a dilute gas

In the case of a dilute gas the thermal conductivity can be calculated from microscopic considerations. Suppose a volume with  $n$  molecules from which roughly one third have velocities along the  $z$  direction.  $\frac{1}{6}n$  molecules with internal energy  $\bar{\epsilon}(z-l)$  at position  $z-l$  move in the positive direction and  $\frac{1}{6}n(z+l)$  with  $\bar{\epsilon}(z+l)$  in the opposite direction. A collision happens after traveling over distance  $l$ , called the mean free path. The heat transferred in the  $z$ -direction  $Q_z$  is

<sup>2</sup> $\leq 1$  nm



**Figure B.16:** Heater and heat sink

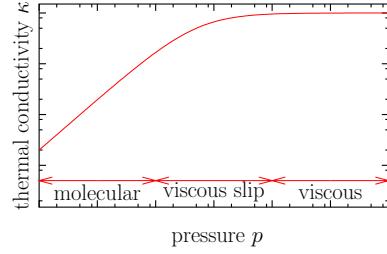


**Figure B.17:** Thermal conductivity as function of the pressure

$$\begin{aligned}
 Q_z &= \frac{1}{6} n \bar{v} [\bar{\epsilon}(z-l) - \bar{\epsilon}(z+l)] \stackrel{Taylor}{=} \frac{1}{6} n \bar{v} \left[ \bar{\epsilon}(z) - l \frac{\partial \bar{\epsilon}(z)}{\partial z} \right] - \left[ \bar{\epsilon}(z) + l \frac{\partial \bar{\epsilon}(z)}{\partial z} \right] \\
 &= \frac{1}{6} n \bar{v} \left( -2 \frac{\partial \bar{\epsilon}(z)}{\partial z} l \right) = \frac{1}{3} n \bar{v} l \frac{\partial \bar{\epsilon}(z)}{\partial T} \frac{\partial T}{\partial z}
 \end{aligned}
 \tag{B.49}$$

with  $c = \frac{\partial \bar{\epsilon}(z)}{\partial T}$  the pressure independent specific heat per molecule.

$$\kappa = \frac{1}{3} n \bar{v} c l
 \tag{B.50}$$

In order to derive the formula the following assumptions have been made: the free mean path is much larger than the diameter of the molecules to have only two-particle collisions and the number of molecules is sufficiently large enough to have molecules collide predominantly with other molecules rather than with the walls ( $l \ll L$ ). For vacuum  $n$  decreases to zero and so does the thermal conductivity.

The thermal conductivity as function of the pressure can be split up in three parts, see figure B.17. This can be characterized by the Knudsen number  $K_n$ , which is the quotient of the mean free path  $\lambda$  of a molecule and the characteristic length  $L$  of the geometry, see figure B.16:

- $3 < K_n$ : molecular region
- $0.01 < K_n < 3$ : viscous slip region
- $K_n < 0.01$ : viscous region

In the viscous region  $\kappa$  is pressure independent, because the number of particles in a volume,  $n$ , and the mean free path  $\lambda$  of the molecules are directly and inversely proportional to gas pressure. In the molecular region for the mean free path the characteristic length can be filled in, which shows that the thermal conductivity is proportional to the pressure.

The thermal conductivity can be expressed as [34]:

$$\kappa \approx \rho c_p \frac{1}{3} \bar{v} \lambda
 \tag{B.51}$$

with  $c_p$  the specific heat at constant pressure, the diffusion coefficient [57] and  $\bar{v}$  the mean molecular velocity.

The Pirani sensor makes use of the pressure dependency of the thermal conductivity.

# Appendix C

## Lock-in amplifier and $\omega - 3\omega$ -method

### C.1 Lock-in amplifier

To amplify small signals a lock in amplifier has been used. A lock in amplifier has compared to a DC amplifier a smaller offset and is compared to an AC amplifier less sensitive for harmonic influences from outside. In figure C.1 a schematic overview is given. The signal is first modulated, amplified, again modulated and the higher harmonics are filtered off. The digital LIA has also the possibility to measure higher order components, which can be used for the  $\omega - 3\omega$ -method.

### C.2 $\omega - 3\omega$ -method

The temperature of a harmonically heated wire can be measured by looking at the third harmonic component. For a resistor  $R_0$  [ $\Omega$ ] a current is applied of

$$I = \hat{I} \cos(\omega t) \tag{C.1}$$

with  $\hat{I}$  the amplitude of the current and  $\omega$  [ $rad/s$ ] the angular frequency. The power  $P$  [ $W$ ] dissipated in the resistor is

$$P = R_0 I^2 = R_0 (\hat{I} \cos(\omega t))^2 = R_0 \hat{I}^2 \left( \frac{1}{2} + \frac{1}{2} \cos(2\omega t) \right) \tag{C.2}$$

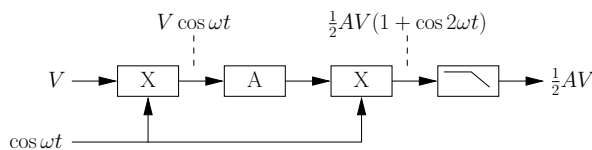


**Figure C.1:** Schematic overview of the lock-in amplifier

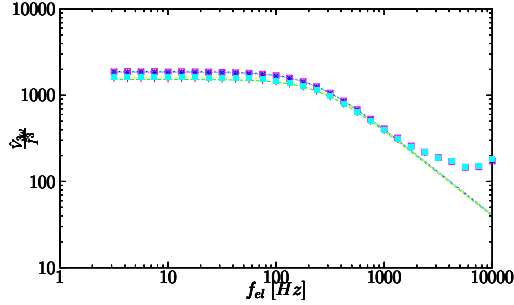


**Figure C.2:** The measured  $3\omega$  component over the current to the power three as function of the applied electrical frequency. For the five heater segments the data has been fitted to a first order model.

Assume that the temperature  $T$  of the resistor is proportional to the power with a phase lag  $\phi$ .

$$T = H(\omega) P \quad (\text{C.3})$$

with  $H(\omega)$  a function of  $\omega$ . The resistance change  $\Delta R$  changes via equation 2.1 also with  $2\omega t + \phi$ . The change in resistance becomes:

$$\Delta R = R_0 \alpha H(\omega) R_0 \hat{I}^2 \frac{1}{2} \cos(2\omega t + \phi) \quad (\text{C.4})$$

Assume that  $\Delta R \ll R_0$ . The resistance has to be multiplied by the current, resulting in the third  $\omega$  component using  $\cos(3a + a) + \cos(2a - a) = 2 \cos(2a) \cos(a)$ .

$$U_{3\omega} = \alpha H(\omega) R_0^2 \hat{I}^3 \frac{1}{4} \cos(3\omega t + \phi) \quad (\text{C.5})$$

The total voltage has the following form:

$$U \propto (\omega t, \omega t + \phi, 3\omega t + \phi) \quad (\text{C.6})$$

The first order component is a combination of two signals, the third order only from one. Normalizing it to the generating voltage  $\hat{V}_{gen} = R_0 \hat{I}$  gives

$$\frac{\hat{V}_{3\omega}}{\hat{V}_{gen}} = \frac{1}{4} \alpha H(\omega) R_0 \hat{I}^2 \quad (\text{C.7})$$

As an approximation for the transfer function  $H(\omega)$  a first order behavior has been taken, see figure C.2, for a measurement on a v-grooved pressure sensor with five segmented beams.

$$H(\omega) = \frac{R}{1 + j\omega RC} \quad (\text{C.8})$$

For the heat capacitance of the beam  $C = \rho cV$  [ $J/K$ ] has been taken, with  $\rho$  the density,  $c$  the specific heat and  $V$  the volume. Due to the heat sink near the heated beam the thermal resistance  $R$  from the beam to the heat sink via the fluid can be calculated using the method of images, see C.3.



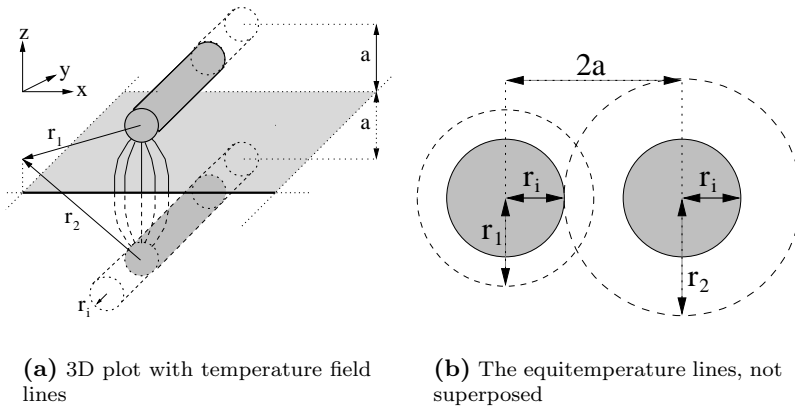


**Figure C.3:** Method of images for  $\infty$  line source and plane conductor

The temperature field up to the heat sink is given by:

$$T = \frac{q'}{2\pi\kappa} \left( \ln \frac{r_i}{r_1} - \ln \frac{r_i}{r_2} \right) = \frac{q'}{2\pi\kappa} \ln \frac{r_2}{r_1} \quad (\text{C.9})$$

in cartesian coordinates  $r_1 = \sqrt{(z-a)^2 + x^2}$  and  $r_2 = \sqrt{(z+a)^2 + x^2}$  and  $r_i$  the inner radius of the cylinders, which is eliminated. For obtaining equitemperature lines the quotient of  $r_1$  and  $r_2$  has to be taken constant. Filling these in results in an equation for a circle.

The thermal line conductance is defined as  $G' = \frac{dq'}{dT}$ . Using equation C.9 results in:

$$G' = \frac{2\pi\kappa}{\ln\left(\frac{r_2}{r_1}\right)} \quad (\text{C.10})$$

The distance between the real and image source is  $2a$ , see figure C.3 . For  $r_1$  can be taken the inner radius of the source  $r_1$  and for  $r_2$  has to be taken  $2a - r_1$ .

$$G' = \frac{2\pi\kappa}{\ln\left(\frac{2a-r_1}{r_1}\right)} \quad (\text{C.11})$$

If  $r_1 = a$  the resistance is of course zero. If  $r_1 \ll 2a$  then  $2a - r_1 \approx 2a$ : the formula is equal to the equation with a cylindrical boundary with inner radius  $r_1$  and outer radius  $2a$ .



# Summary

In this thesis the framework of thermal sensor-actuator structures is proposed for measuring the parameters pressure  $p$ , dynamic viscosity  $\mu$ , thermal conductivity  $\kappa$ , specific heat  $c$ , density  $\rho$  and fluid velocity  $v$ . All structures are based on simple resistive elements that can be used as actuator and sensor simultaneously.

Making use of a lot of simple structures has an added value: an array of resistors makes it possible to eliminate the Temperature Coefficient of Resistance of the metal by measuring the quotient of the temperature distribution of the array to the temperature at the center. The shape of the temperature distribution is determined by the heat transfer through the carrier to the support and the heat transfer to the fluid. Using the temperature distribution the loss of heat to the support can be taken into account, independent of the applied fluid, pressure or flow.

The design considerations for the structures are given and the measurement methods are discussed. Each structure has been optimized for a certain parameter by taking a specific geometry: a thin or a thick beam or a membrane, near or far away from a heat sink and with or without forced convection. The basic element is a heater along the center of the beam. The heater is divided into segments that are connected individually. Making use of four points measurements we are able to measure the temperature distribution. The shape of the temperature distribution depends on the heat transfer from the beam to the support and the heat transfer by conduction and forced convection from the beam to the fluid. Based on this principle a flow sensor, a v-grooved Pirani sensor and a bending membrane pressure sensor with thermal readout have been fabricated and characterized.

Two types of flow sensors with distributed temperature sensing are presented: a probe having a thin beam between the ends of two legs and several beams in a micromachined hexagonal channel. The cooling down of the probe by a uniform flow can be described by a one dimensional differential equation in cartesian coordinates. In the micromachined channel the parabolic flow profile will result in a dip in the temperature distribution at the center. A lumped element model has been used for calculating the temperature distribution. DC measurements are carried out for the gases nitrogen, carbon dioxide and helium on beams having 25 segments.

A thermal conductivity sensor consisting of a thin beam with distributed temperature sensing above a v-grooved heat sink has been discussed. For characteristic lengths smaller than the mean free path of the gas molecules the thermal conductivity depends on pressure, which makes it suitable as a pressure sensor. The heater has five segments. The model takes in account that the temperature has been averaged over a segment instead of being measured in a single point. For a characteristic length

of 20  $\mu\text{m}$  a transition pressure of about 20 mbar has been found. The possibility of taking the heat transfer to the support in account enlarges the measurement range.

A mechanical pressure sensor with thermal readout is shown. A differential pressure over a thin circular membrane results in a deflection. The membrane is placed 1  $\mu\text{m}$  above a heat sink. The heat transfer from the membrane to the heat sink depends on the deflection. Two types of sensors have been realized: one with a spiral heater and one with a meandering heater with distributed sensing. The transition pressures are around 0.2 bar. For the non-deflected membrane an analytical model can be derived, like done for the flow sensor with uniform flow profile except using cylindrical coordinates. For a deflected membrane a lumped element model has been used. A dip arises in the temperature distribution, like for the flow sensor with parabolic flow profile, when the membrane deflects towards the heat sink. The thermal conductivity of the fluid between the membrane and heat sink depends on the pressure, like for the v-grooved pressure sensor. A second sensor is needed to compensate for this and can also be used to measure the absolute pressure.

The designs of the TCR-sensor and kinematic viscosity sensors have been fabricated. The two versions of the TCR-sensor consist of a thick beam with distributed temperature sensing. One has a heater with five segments, the other only a heater at the center and several sensors at one side. From the known temperature distribution, given by the thermal properties of the beam, and the electrical resistance the TCR can be obtained.

# Samenvatting

In dit proefschrift is het raamwerk van temperatuurmeterverhitters voorgesteld voor het meten van de parameters druk  $p$ , dynamische viscositeit  $\mu$ , thermische geleidbaarheid  $\kappa$ , soortelijke warmte  $c$ , dichtheid  $\rho$  en de snelheid van het fluïdium. Alle structuren zijn gebaseerd op simpele resistieve elementen, welke tegelijkertijd als verhitter en als temperatuurmeter kunnen worden gebruikt.

Het gebruik maken van veel simpele structuren heeft een toegevoegde waarde: een rij weerstanden maakt het mogelijk de weerstandstemperatuurcoëfficiënt te elimineren door het quotiënt van de temperatuurverdeling van een rij weerstanden en de temperatuur in het centrum te meten. De vorm van de temperatuurverdeling wordt bepaald door het warmtetransport door de drager naar de ophanging en het warmtetransport naar het fluïdium. Gebruikmakend van de temperatuurverdeling kan het warmteverlies naar de ophanging worden meegenomen, onafhankelijk van het aangebrachte medium, druk of fluïdiumstroom.

De ontwerpoverwegingen van de structuren zijn gegeven en de meetmethodes zijn behandeld. Elk structuurtje is geoptimaliseerd voor een bepaalde parameter door een specifieke geometrie te nemen: een dunne of een dikke balk of membraan, dichtbij of veraf van een koude wand en met of zonder geforceerde convectie. Het basiselement is een longitudinaal geplaatste verhitter in het midden van de balk. De verhitter is verdeeld in verschillende segmenten, welke individueel zijn aangesloten. Gebruikmakend van een vierpuntsmeting zijn we in staat de temperatuurverdeling te meten. De vorm van de temperatuurverdeling hangt af van het warmtetransport door de balk naar de ophanging en het warmtetransport door geleiding en geforceerde convectie van de balk naar het fluïdium. Gebaseerd op dit principe zijn een fluïdiumstroommeter, een v-groeve Pirani drukmeter en een buigend-membraan drukmeter met thermische uitlezing gefabriceerd en gekarakteriseerd.

Twee typen fluïdiumstroommeters met gedistribueerde temperatuurmeters zijn gepresenteerd: een meetprobe met een dunne balk tussen de uiteinden van twee armen en een aantal balken in een microgefabriceerd hexagonaal kanaal. Het afkoelen van de meetprobe door een uniforme fluïdiumstroom kan worden beschreven met een eendimensionale differentiaalvergelijking in het carthesische coördinatenstelsel. In het microgefabriceerde kanaal zal het parabolische snelheidsprofiel resulteren in een dip in het centrum van de temperatuurverdeling. Een verdeeld model is gebruikt voor het berekenen van de temperatuurverdeling. Gelijkstroommetingen zijn uitgevoerd op balken met 25 segmenten voor de gasen stikstof, kooldioxide en helium.

Een thermische geleidbaarheidsmeter met een dunne balk met gedistribueerd meten boven een v-vormige koude wand is besproken. Voor karakteristieke afstanden kleiner

dan de vrije weglengte hangt de thermische geleidbaarheid af van de druk, hetgeen het geschikt maakt als drukmeter. De verhitter heeft vijf segmenten. In het model is meegenomen dat de temperatuur over een segment is gemiddeld in plaats van in een enkel punt. Voor een karakteristieke afstand van 20 micrometer is een transitiedruk van ongeveer 20 millibar gevonden. De mogelijkheid om het warmtetransport naar de ophanging mee te nemen, vergroot het bereik.

Een mechanische drukmeter met thermische uitlezing is getoond. Een verschil-druk over een dun cirkelvormig membraan resulteert in een deflectie. Het membraan is één micrometer boven de koude wand geplaatst. Het warmtetransport van het membraan naar de koude wand is afhankelijk van de deflectie. Twee versies van de meters zijn gerealiseerd: een met een spiraal en de ander met een meanderende verhitter met gedistribueerd meten. De transitiedrukken zijn ongeveer 0.2 bar. Voor een niet-buigend membraan kan een analytisch model worden afgeleid, zoals gedaan voor de fluïdiumstroommeter met uniform snelheidsprofiel, maar dan met cilindrische coördinaten. Voor een gebogen membraan is een verdeeld model gebruikt. Een dip verschijnt in de temperatuurverdeling, zoals bij de fluïdiumstroommeter met een parabolisch snelheidsprofiel, wanneer het membraan naar de koude wand buigt. De thermische geleidbaarheidsmeter voor het fluïdium tussen het membraan en de koude wand is drukafhankelijk, zoals voor de v-groef drukmeter. Een tweede drukmeter is nodig om hiervoor te compenseren en kan ook worden gebruikt om de absolute druk te bepalen.

De ontwerpen van de TCR-meter en de kinematische viscositeitsmeter zijn gefabriceerd. De twee versies van de TCR-meter bestaan uit een dikke balk met gedistribueerde temperatuurmeters. Een heeft een verhitter met vijf segmenten, de ander een verhitter in het centrum met een aantal temperatuurmeters aan één kant. Uit de bekende temperatuurverdeling, opgelegd door de thermische eigenschappen van de balk, en de elektrische weerstanden kan de TCR worden verkregen.

# Dankwoord

Het zal mensen niet zijn ontgaan dat als in een gesprek met mij een raakpunt is met fietsen het gesprek richting het voertuig of de beweging zelf zal worden gebogen. Het zal dan ook niet verbazingwekkend zijn dat dit terug komt in het dankwoord.

Het begon allemaal met een plasticen loopfiets. Allereerst wil ik mijn ouders en zus bedanken voor de geboden mogelijkheden, steun en de vele adviezen. Met name mijn moeder heeft veel voor mij gedaan en heb ik veel van geleerd; spijtig genoeg heeft ze de afronding van de promotie niet meer kunnen meemaken.

Met mijn eerste stalen fiets ging ik naar de lagere school, alwaar ik onder andere het plakken van binnenbanden leerde, waarvoor ik de juffen en meesters wil bedanken. In het bijzonder is in mijn gedachten gebleven de energierijke en motiverende meester Simon Laan: een voorbeeldig meester. Daarna moest ik op een stadsfiets naar het VWO. Na zes jaar training kon ik het niet meer met de fiets af en moest verhuizen naar Twente. De racefiets kwam bij mij in zwang, waarop ik nog steeds met Hugo en René vele kilometers in Twente berijd. Dat zouden meer mensen uit de groep moeten doen (Han?). Na zes jaar elektrotechniek te hebben gedaan, kwam bij mij de interesse voor een wat meer geëvolueerde fiets: de ligfiets, een toermodel, gevolgd door een snelle lage fiets.

Naast fysieke fietsen heb ik ook een ‘virtuele’ fiets bereden; diamantvormig frame met dubbele bovenbuis, merk micmec, type anarchistisch, bestaande uit: het stijve frame, opgebouwd uit de onderbuis (als enige trekbelast) Miko, die ondanks de geboden vrijheden de boel bij elkaar hield, de zitbuis Remco (zeer stabiel type), Theo (balhoofdbuis) had veel ideeën die wel eens moesten worden gedempd, Gijs (de bovenbuis) waar je je wel eens tegen kon stoten door zijn terechte kritische houding en Paul (onderste bovenbuis) onze projectleider en mijn tweede promotor. De technologen vormen de vorken: Remco (staande) met allerlei adviezen voor onder andere de meetapparatuur, Meint (liggende) en Erwin (voor) voor de procesttechnologie. Marieke en Judith, de handvatten van de groep, voor een comfortabel gesprek. Dick (het mannetje, dit is het buisje achter de bracketpot en tussen de liggende achtervorkpoten) voor extra stabiliteit, het regelen en bestellen van allerlei spulletjes. Henk voor het ter beschikking stellen van een aantal meetapparaten. Willem, het stuur voor mij in de Linux wereld. Hans-Elias, het zadel, waarop hij mij na een dipje weer heeft geholpen. Petranella voor de motivatie bij het trainen als ik weer eens teveel aan het communiceren was. Henri voor het klappen over het terrein België als ik weer eens goesting had (Awel, verstade da nie?). Edwin over de gesprekken over voeding (in de mensa). De onderdelen Phillip, Regina, Joost, Kees, Yuri, Hien, Toon, Saravanan, Edin, Fran, Roald, Jeroen, Marko, Niels, Martijn, Stefan, Deladi, Florian, Theo, Henk

en de studenten Dick, Michele, Wilco en Marcel maken het plaatje compleet.

Het onderhoud aan het rijwiel is vrij vlot verricht door de mensen van de clean room, zoals Gerard, Johnny, Peter en Huib. Erg gemakkelijk.

Bij het draaien en frezen van speciale onderdelen hielp Mario van de FTD je altijd op weg. Bedankt!

De open bron gemeenschap voor het maken van al die handige programmaatjes, zoals Slackware linux, pdfL<sup>A</sup>T<sub>E</sub>X met bijbehorende pakketten (TexPower, a0poster, thumbpdf, pdfpages, ...), Xfig, gnuplot, The Gimp, the lexical database Wordnet (“thanks – an acknowledgment of appreciation”), etcetera.

Van de meer dan 1000 onderdelen zal ik ongetwijfeld essentiële onderdelen zijn vergeten te benoemen...





